Electron Transfer Involving the Phylloquinone (A_1) Cofactor of Photosystem I

Examined with Time Resolved Absorbance and
Electron Paramagnetic Resonance Spectroscopy

Samuel Mula Jr., Bachelor of Science in Chemistry

Chemistry

Submitted in partial fulfillment
of the requirements for the degree of

Doctor of Philosophy

Faculty of, Mathematics and Science, Brock University
St. Catharines, Ontario

Quote

“Wisdom is not a product of schooling, but of the lifetime attempt to acquire it”

Albert Einstein

Dedication

This thesis is dedicated to my mother,

Sandra L. Prischak,

without whom none of this would be possible.

Abstract:

The dependence of the electron transfer (ET) rate on the Photosystem I (PSI) cofactor phylloquinone (A_1) is studied by time-resolved absorbance and electron paramagnetic resonance (EPR) spectroscopy. Two active branches (A and B) of electron transfer converge to the F_X cofactor from the A_{1A} and A_{1B} quinone.

The work described in Chapter 5 investigates the single hydrogen bond from the amino acid residue PsaA-L722 backbone nitrogen to A_{1A} for its effect on the electron transfer rate to F_X. Room temperature transient EPR measurements show an increase in the rate for the A_{1A}^- to F_X for the PsaA-L722T mutant and an increased hyperfine coupling to the 2-methyl group of A_{1A} when compared to wild type. The Arrhenius plot of the A_{1A}^- to F_X ET in the PsaA-L722T mutant suggests that the increased rate is probably the result of a slight change in the electronic coupling between A_{1A}^- and F_X. The reasons for the non-Arrhenius behavior are discussed.

The work discussed in Chapter 6 investigates the directionality of ET at low temperature by blocking ET to the iron-sulfur clusters F_X, F_A and F_B in the *menB* deletion mutant strain of *Synechocyctis* sp. PCC 6803, which is unable to synthesize phylloquinone, by incorporating the high midpoint potential (49 mV vs SHE) 2,3-dichloro-1,4-naphthoquinone (Cl_2NQ) into the A_{1A} and A_{1B} binding sites. Various EPR spectroscopic techniques were implemented to differentiate between the spectral features created from A and B- branch electron transfer. The implications of this result for the directionality of electron transfer in PS I are discussed.

The work discussed in Chapter 7 was done to study the dependence of the heterogeneous ET at low temperature on A_1 midpoint potential. The menB PSI mutant contains plastiquinone-9 in the A_1 binding site. The solution midpoint potential of the quinone measures 100 mV more positive then wild-type phylloquinone. The irreversible ET to the terminal acceptors F_A and F_B at low temperature is not controlled by the forward step from A_1 to F_X as expected due to the thermodynamic differences of the A_1 cofactor in the two active branches A and B. Alternatives for the ET heterogeneity are discussed.

Acknowledgements

First and foremost, I would like to express my gratitude to Dr. Art van der Est for the opportunity to work in his lab for the past five years. His patience, insight, knowledge and guidance have been indispensable. His mentorship has brought to light some of the greatest mysteries of the physical world for which I would have never seen and I am forever in his debt.

Secondly, I would like to thank my committee members, Dr. Stuart Rothstein, Dr. Travis Dudding and Dr. Doug Bruce for their guidance during my PhD projects.

In addition, I would like to thank Dr. Prashanth Poddutoori, the members of the Doug Bruce Lab and the members of the John Golbeck lab for their collaborative efforts and critical instruction.

Lastly, I would like to thank my family and friends for enduring the journey with me and giving me words of encouragement to persevere and successfully complete what I never thought would be possible.

Table of Contents

List of Figures

List of Tables

Abbreviations List

Abbreviation	Description
O_2	Oxygen
H_2O	Water
CO_2	Carbon Dioxide
P	Phosphate
ETC	Electron Transport Chain
LHI	Light Harvesting Complex I
LHII	Light Harvesting Complex II
ET	Electron Transfer
PSI	Photosystem I
PSII	Photosystem II
ADP	Adenosine diphosphate
ATP	Adenosine triphosphate
Cyt-b_6f	Cytochrome b_6f
$NADP^+$	Nicotinamide adenine dinucleotide phosphate
NADPH	Nicotinamide adenine dinucleotide hydrogen phosphate
PC	Plastocyanin
Chl-*a*	Chlorophyll-*a*
PQ	Plastoquinone
PQH_2	Plastoquinol
Fd	Ferrodoxin
FNR	Nicotinamide Diphosphate Reductase
ATP-Synthase	Adenosine Triphosphate Synthase
ET	Electron Transfer
A-branch	PsaA subunit association
B-branch	PsaB subunit association
A_{-1A}	A-branch Chlorophyll-*a* PSI ET cofactor
A_{-1B}	B-branch Chlorophyll-*a* PSI ET cofactor
A_{0A}	A-branch Chlorophyll-*a* PSI ET cofactor
A_{0B}	B-branch Chlorophyll-*a* PSI ET cofactor
A_1	Phylloquinone PSI ET cofactor
A_{1A}	A-branch Phylloquinone PSI ET cofactor
A_{1B}	B-branch Phylloquinone PSI ET cofactor
F_X	[4Fe4S] Cluster PSI ET cofactor
F_A	[4Fe4S] Cluster PSI ET cofactor
F_B	[4Fe4S] Cluster PSI ET cofactor
P_{700}	Photosystem I Energy Trap
P_{680}	Photosystem II Energy Trap
DA	Donor/Acceptor pair
Tyr,Y	Tyrosine
Leu, L	Leucine
Trp, W	Tryptophan
Ser, S	Serine

Phe, F	Phenylalanine
Thr,T	Threonine
WT	wild-type
ENDOR	electron nuclear double resonance spectroscopy
EPR	electron paramagnetic resonance spectroscopy
TREPR	transient EPR spectroscopy
CW EPR	continuous wave EPR spectroscopy

Chapter 1 Literature Review

1.1 Introduction

Photosynthesis is the metabolic process by which plants and other organisms convert solar energy into energetically dense molecular bonds. A large portion ($3x10^{21}$ J) of the earth's sparse annual electromagnetic flux ($3x10^{24}$ J) is converted by this process. [1] Although photosynthesis has been known since the early 1700's and been studied since the 1880's, [2] some aspects of the process are still not well understood.

What studies have been able to determine over the decades is that the storage of solar energy is a complicated orchestration of biophysics and bioenergetics. The energy conversion occurs by light induced electron transfer which effectively transfers the photon energy into electric potential energy. The conversion happens within several complex proteins which interact through a series of cofactors and small molecules that make up what is known as the electron transport chain (ETC).

The light induced electron transfer reactions are known to take place in the two large photoactive proteins of the ETC, Photosystem I (PSI) and Photosystem II (PSII). In both of these proteins, light excitation, charge separation and sequential electron transfer occur, but the details of the processes and their role in the ETC differ. [1, 3-5] In this work we examine the biophysics and bioenergetics of sequential electron transfer within PSI, focusing on the thermodynamic aspects that govern the forward and reverse electron transfer steps through the two Phylloquinone (A_1) cofactors. Currently, the literature indicates the thermodynamic properties of A_1 are key factors in governing the equilibrium of the electron transfer reactions within the PSI reaction center. This thesis

continues that work by investigating the A_1 properties with recently developed methods. These methods have made it possible to exchange the A_1 cofactor with other quinones and, in addition, its interaction within the protein can be altered by genetic mutations. PSI research of the light-induced electron transfer reactions within the protein provide a knowledge base of design principles for creating synthetic analogs, which mimic the light gathering and rapid stabilization of the charge separated state. The rate between sequential ET cofactors is governed by not only thermodynamics (i.e Gibbs free energy) but also quantum mechanics (i.e. electronic couplings) which are important factors when considering synthetic alternatives. The A_1 electron transfer cofactor could prove useful for these synthetic analogs but its properties and role in PSI ET must first be fully understood. The capability of quinone exchange and genetic mutation techniques allow for the investigation of both thermodynamic and quantum mechanical properties of A_1.

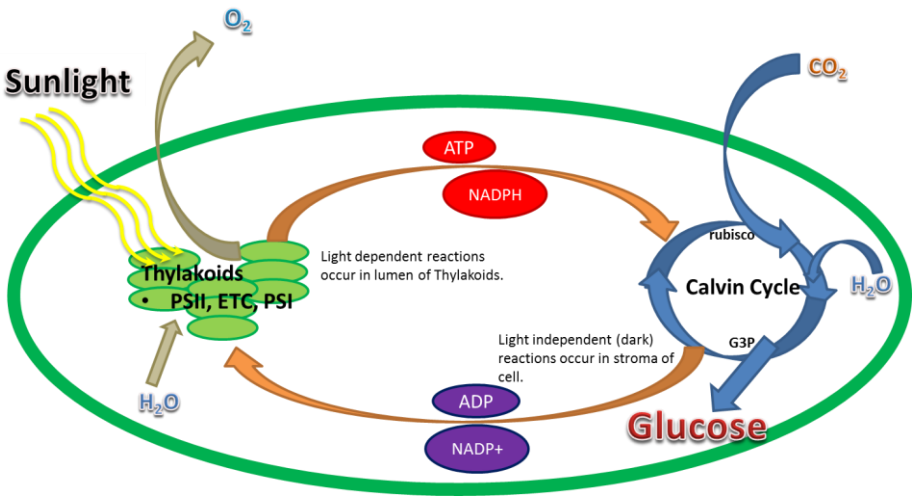

Figure 1-1: Cellular cartoon of the photosynthetic process. The image shows the major starting materials and end products of the light and dark reactions of photosynthesis.

1.2 Photosynthesis

1.2.1 Early understanding and general chemistry.

Early understanding of photosynthesis came about in the 17th century with the work of Jan van Helmont who coined the term "gas" and is responsible for pioneering "pneumatic chemistry" [6] and its role in plant metabolism, and of Joseph Priestley's observations of the direct consumption and evolution of gas from plants. [7] The overall reaction of oxygenic photosynthesis for the conversion of water and CO_2 into carbohydrate [CH_2O] and oxygen is:

$$CO_2 + H_2O + 478\ \text{kJ} \rightarrow [CH_2O] + O_2 \qquad (1.1)$$

The 478 kJ of energy must be supplied per mole of reactant. In terms of light harvesting, if the stoichiometry were 1:1 (i.e. if each photon absorbed led to the reduction of one molecule of CO_2), the photons would have to be of high energy in the UV region at a wavelength of approximately 250 nm. [1] Instead, the process is divided into multiple steps with two different photosystems working in series to allow multiple lower energy photons in the visible region to be used. The storage of the photon energy is done through single electron chemistry by means of protein catalysis. As can be seen in Figure 1-1, there are light and dark reactions of photosynthesis, both of which carry out the catalytic reactions but are carried out in separate areas of the cell. The chemical reaction for the light driven process of oxygenic photosynthesis is:

$$2\ H_2O + 4\ NADP^+ + 8\ \text{photons} \rightarrow 4\ NADPH + O_2 \qquad (1.2)$$

The equation is balanced according to the production of one molecule of O_2 which requires eight sequential photons of light for the extraction of eight electrons. [8] The eight electrons removed from the water molecules, in addition to four available protons, are then used to reduce the electron carrier $NADP^+$ to NADPH to complete the redox reaction. The reaction (1.2) is carried out in the thylakoid membranes. The two regions of space on either side of the thylakoid membrane are defined as the lumen and stroma or interior and exterior respectively. The oxidation of water takes place on the lumenal side and the reduction of NADP+ occurs on the stromal side while the lipid bilayers serves as scaffold for the ETC components (Figure 1-2) which are embedded in the membrane. The reduction of CO_2 (1.1) to carbohydrate is not a part of the light reactions, but instead it takes place in the stroma of the thylakoid membrane during the dark reactions and is shown below:

$$3\,CO_2 + 9\,ATP + 6\,NADPH + 6\,H^+ \rightarrow C_3H_6O_3\text{-}Pi + 9\,ADP + 8\,Pi + 6\,NADP^+ + 3\,H_2O \quad (1.3)$$

The completion of photosynthesis ends with the synthesis of carbohydrates during the Calvin Cycle. (Figure 1-1) The fixation of carbon dioxide by the enzyme rubisco begins a series of reductive reactions at the end of which CO_2 is converted into a simple sugar. The reducing species ATP and NADPH are generated from the light reactions and following the oxidation to ADP and NADP+ during the dark reactions of the Calvin cycle, they are returned. The organism uses the sugars as energy reserves for other metabolic processes during cellular respiration. The proteins that constitute the ETC carry out the redox coupled reactions in series where absorption of light begins the reaction sequence.

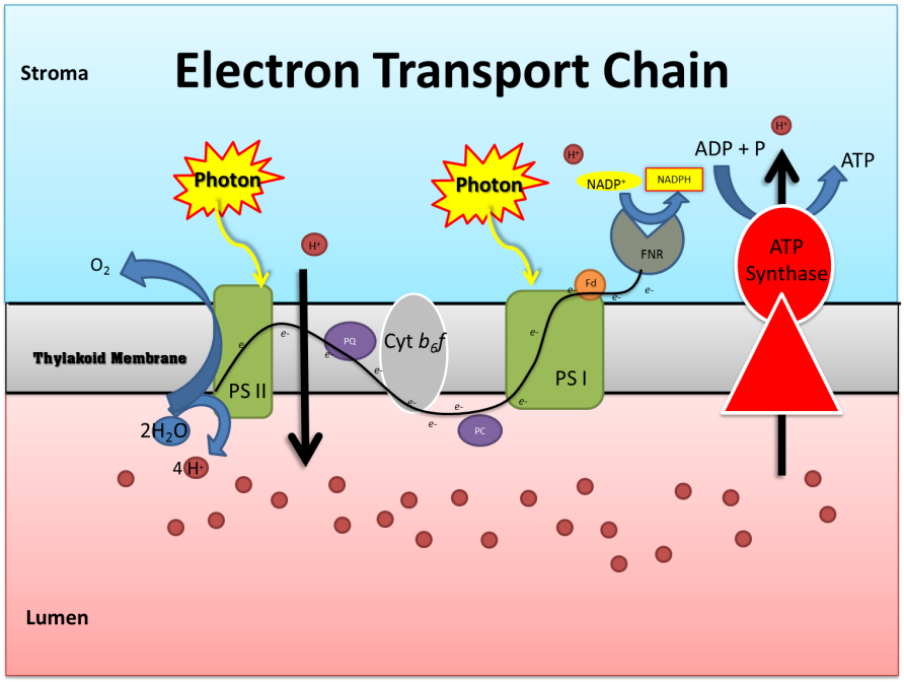

Figure 1-2: Cartoon depicting the proteins of the Electron Transport Chain (ETC) for the light driven reactions of oxygenic photosynthesis. Photosystem II (PSII), Photosystem I (PSI), Plastoquinone (PQ), Cytochrome *b*$_6$*f* (Cyt *b*$_6$*f*), Plastocyanin (PC), Ferredoxin Reductase (Fd), Nictoamide Diphosphate Reductase (FNR), Adenosine diphosphate (ADP), Adenosine triphosphate (ATP), Adenosine triphosphate Synthase (ATP Synthase) are shown.

1.2.2 Electron Transport Chain Components

The components of the ETC that perform the overall light reaction in oxygenic photosynthesis are four protein complexes Photosystem I (PSI) and II (PSII), cytochrome *b*$_6$*f* (Cyt *b*$_6$*f*) and ATP-synthase are incorporated into the thylakoid membrane. [1, 3, 5, 8] The photoactive proteins, PSI and PSII, contain ~100 and ~35 chlorophyll-*a* (Chl-*a*) molecules, respectively. In addition, other light active proteins involved in light harvesting (e.g. phycobilliosomes and the Light Harvesting Complex I and II (LHCI & LHCII)) which vary from species to species are also usually present. [9, 10]

The process of photosynthesis is initiated with the absorption of a photon by one of the Chl-*a* molecules (or light harvesting cofactors) to form the excited state, Chl-*a**. The exiton, Chl-*a**, migrates through the antenna to the specialized Chl-*a* energy traps

P_{700} and P_{680} of the respective photosystems, PSI or PSII, from which initial charge separation and sequential electron transfer occurs via a chain of cofactors within the proteins. A more thorough review of the PSI and PSII light harvesting and excitation energy transfer can be found in [11]. PSII serves as a light driven water:plastoquinone oxidoreductase that oxidizes water and delivers electrons to its terminal acceptor plastoquinone (PQ) to form plastoquinol (PQH_2). The intermediate Cyt b_6f is a heme based protein that continues the ETC from PSII to PSI by oxidizing PQH_2 and reducing plastocyanin (PC). PSI serves as a plastocyanin:ferredoxin oxidoreductase that oxidizes PC and reduces ferredoxin (Fd). The NADP reductase (FNR) protein accepts reductive equivalents from Fd and converts NADP+ to NADPH. During this process an electrochemical gradient of protons is built up as a result of water oxidation and protons being shuttled from the stroma to the lumen by the PQ/PQH_2 couple. This gradient is utilized by the ATP Synthase protein for the conversion of ADP to ATP. These are the reactions that comprise the light driven oxidative photosynthesis process.

1.2.3 Redox Scale of ETC components

The scheme in Figure 1-3 depicts the redox potentials of the ETC components and is often referred to as the photosynthetic Z-scheme. [12] The scheme shows that the energy gap between the water oxidation couple (+1.3eV) and NADP+ reduction couple (-0.34 eV) is accessible by a visible region photon (680 nm = 1.8 eV). However, much of the potential energy is lost during the electron transfer from P_{680} to PQ and thus two photons are needed. Hence, the reaction is divided across two proteins (PSI and PSII), which can be physically separated from one another and which operate in two different regions of the redox scale. The reduction side of the scale is covered by PSI.

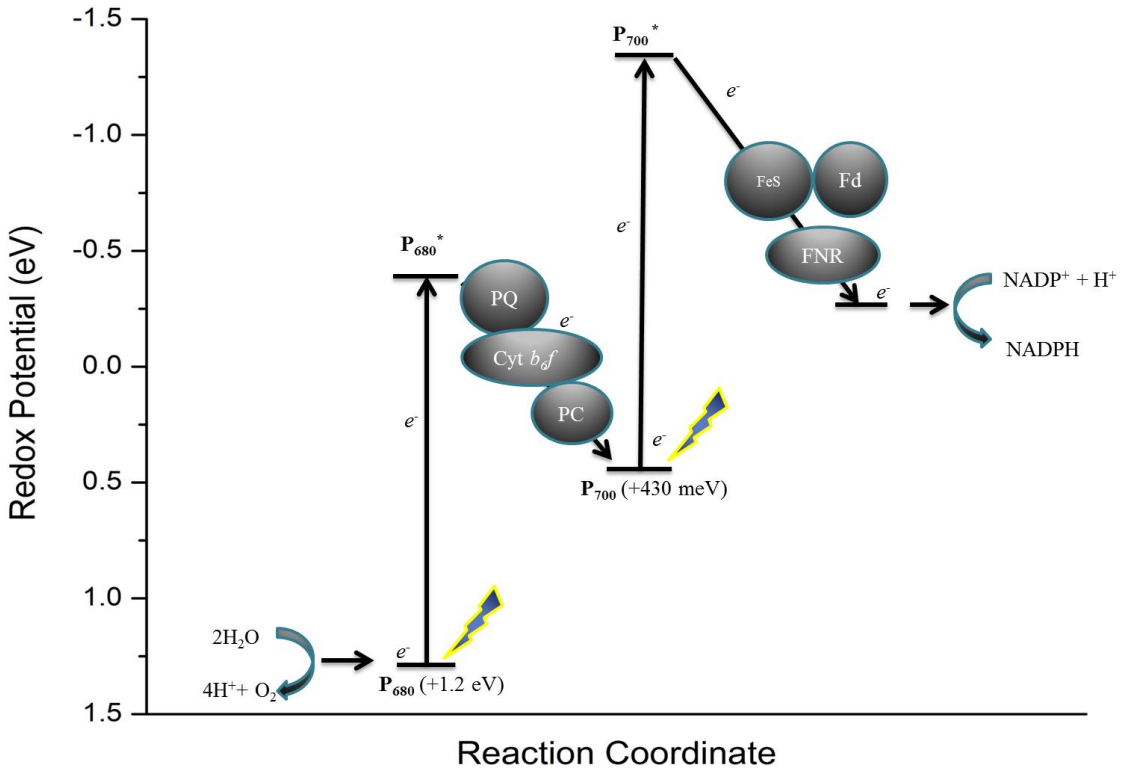

Figure 1-3 The electron redox potentials for oxygenic photosynthesis Z-Scheme including reaction centers P_{700} and P_{680} of Photosystem I and II, respectively. The intermediate electron carriers plastoquonone (PQ), cytochrome *b*$_6$*f* (Cyt *b*$_6$*f*), plastocyanin (PC), iron sulfur cluster (FeS), ferredoxin (Fd) and NADP reductase (FNR) are also included.

1.3 Photosystem I (PSI): The Plastocyanin:Ferredoxin Oxidoreductase

The PSI trimer complex is a very large protein and has a mass of ~1000 kDa. Incredibly, the X-ray crystal structure of PSI from the cyanobacterium *Thermosynnechococcus elongatus* [13] has been determined to a resolution of 2.5 Å. The structure, which was 15 years in the making, shows that each monomer contains twelve protein subunits, (PsaA-PsaF, PsaI-PsaM and PsaX). Beginning at the periphery of each monomer, there are 90 to 100 Chl-*a* and 20 beta-carotene pigment molecules coordinated

by subunits PsaI-M and PsaX. The three subunits, PsaA, PsaB and PsaC coordinate the charge separation cofactors of the reaction center and are responsible for transferring electrons from the lumenal to the stromal side of the thylakoid membrane. Subunits PsaD, PsaE and PsaF [14] help to keep the PsaC subunit bound to the stromal surface of the complex. Oriented from lumen to stroma the cofactors of electron transfer are a special Chl-*a*/Chl-*a'* dimer, called P_{700}, four Chl-*a* molecules or A_{-1A}, A_{-1B}, A_{0A}, and A_{0B}, two phylloquinone molecules, A_{1A} and A_{1B} and three 4Fe-4S clusters; F_A, F_B and F_X. Subscripts A and B describe which branch the cofactors belong to and are derived from the subunits, PsaA and PsaB, which provides the majority of the cofactor ligands in a given branch. The exceptions are the cofactors F_A and F_B which are ligated exclusively by the PsaC subunit and are not part of the A- or B-branch. Both PsaA and PsaB subunits ligate the F_X cofactor. The two branches of ET cofactors have pseudo C_2 symmetry and diverge at the P_{700} chlorophyll dimer and converge at the iron-sulfur acceptor F_X (Figure 1-4). [1, 4, 15]. The PsaA and PsaB subunits share a high degree of sequence homology but do display differences. [13] The use of these two branches has been studied but the factors governing their relative use are not well understood. [16-19]

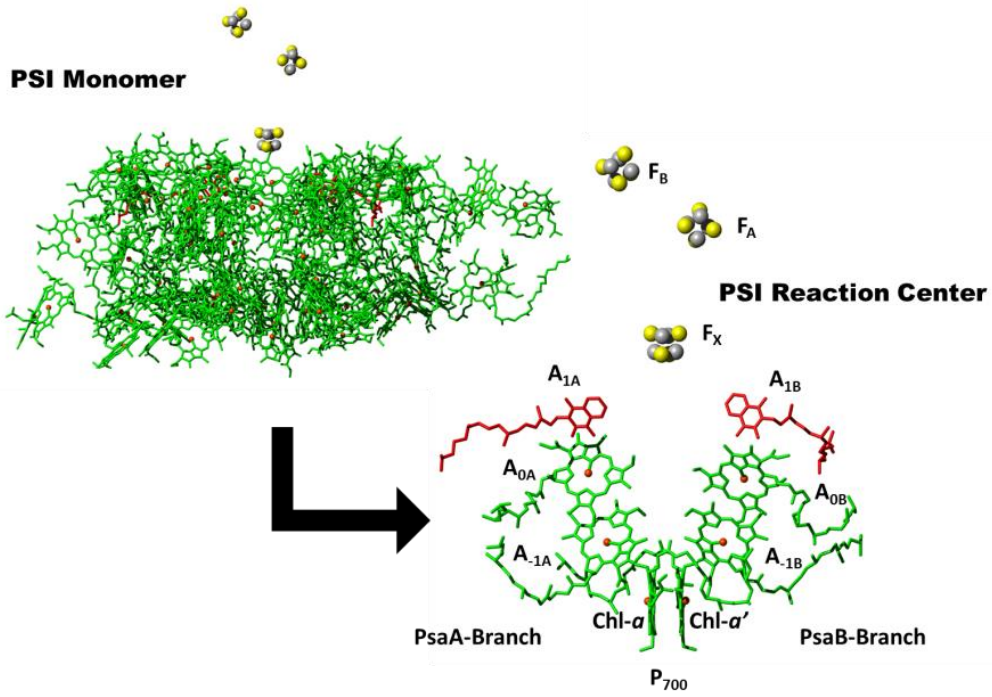

Figure 1-4: (left) Photosystem I (PSI) monomer of the light gathering antenna Chl-*a* molecules with initial charge separation and sequential electron transfer cofactors. (right) PSI Reaction Center cofactors consisting of P_{700} (Chl-*a*/Chl-*a'*) dimer, four Chl-*a* molecules (A_{-1A}, A_{-1B}, A_{0A}, A_{0B}), two naphthoquinone molecules (A_{1A}, A_{1B}) and three [4Fe4S] clusters (F_X, F_A, F_B).

1.4 PSI: Light induced energy and electron transfer

1.4.1 Description of initial charge separation and charge separated states

To achieve efficient ET, the protein serves as scaffolding for holding the cofactors in a fixed orientation relative to one another. In addition, the protein scaffolding also controls the electronic properties of the cofactors. In this sense, the energetics are finely tuned in order to perform efficient light gathering and charge separation by rapidly transferring an electron along a chain of acceptors and thus, creating distance between the oxidized donor and the reduced acceptor.

The first step in this process is the absorption of a photon in the antenna chlorophyll-*a* pigments (Figure 1-4) and the transfer of the Chl-a^* exiton to a photochemical trap by Förster Resonance Energy Transfer (FRET). [20] The photochemical trap is the energy stabilization that occurs when the D^+A^- state is formed from the precursor Chl-a^* exiton. The overall rate of this process is the sum of the trapping rate, which is the rate of electron transfer from D^*A to D^+A^-, and the transfer to trap rate, which is defined as the inverse of the time it takes for the Chl-a^* exiton to reach the photochemical trap.

The location of the initial charge separation is difficult to ascertain because of the spectral overlap of the Chl-a^* exiton and the Chl-a^- radical species and entangled rates associated with the overall rate of the process. The narrow spectral range over which the fast kinetics are examined is between 690 and 730 nm. The blue side of the spectral range is characteristic of the Chl-a^* exiton while red side indicates the species P_{700}^+. Knowing the site of initial charge separation is important because it helps to understand the mechanism by which the precursor D^*A effects later ET directionality. The ET steps following the initial charge separation have been well established and are bidirectional, meaning that both branches actively carry out ET but how initial charge separation effects this bi-directionality is not well understood. PSI is the only known reaction center to carry out bi-directional transfer. The potential sites by which the initial charge separation can proceed are seen in Figure 1-5.

Early work to determine the initial charge separation event involved point mutations of amino acid residues surrounding the P_{700} dimer. The results showed no effect on the relative use of the PsaA and PsaB branches. [21] Continued work

Holtzwarth et. al. [16] was done using mutants PsaA-Y696F and PsaB-Y676F of the green algae *Chlamydomonas reinhardtii*. The tyrosine residues PsaA-Y696 and PsaB-Y676 hydrogen bond to the A_0 chlorophyll of the respective branch and changing these tyrosines to phenylalanine removes the hydrogen bond and influences the redox potential of the A_0^- anion. Ultrafast spectroscopic measurements of the mutants suggest that the initial charge separation occurs between $A_{-1A}^+A_{0A}^-$ or $A_{-1B}^+A_{0B}^-$ (Figure 1-5 **c** and **d**). The decay of absorbance difference spectral features in the 690-730 nm range where species involving the D*A to D^+A^- charge separation step are known to occur slowed from a lifetime of 8-9 ps in WT to a lifetime of ~20 ps in the tyrosine mutants. This event is quickly followed by the oxidation of the dimer P_{700}–P_{700}^+ and the re-reduction of cofactor A_{-1}^+–A_{-1}. This study shows bi-directionality is therefore dictated by the charge separation event and can be seen immediately in the spectral differences. This work also gives direct evidence why the initial mutations surrounding P_{700} would have no effect on branch directionality. Interestingly, the mutation PsaA-Y696F showed a decrease in the yield of A-branch transfer and an increase in the yield of B-branch ET. [17] The A_0^- thermodynamic properties appeared to be controlled by the protein and barriers to forming its reduced state seem to affect the generation of the initial charge separated state in the branch carrying the mutation.

The charge separation mechanism suggested by Holzwarth et. al. is countered by the work done Shuvalov et. al. [22], whom used the cyanbacterium *Synechocystis* sp. PCC 6803 to show initial charge separation occurs from $P_{700}^*A_{-1}$ (Figure 1-5 **a** and **b**) with a lifetime of (< 100 fs) to the charge separated state $P_{700}^+A_0^-$. A kinetic fitting model of unidirectional ET was used to disentangle the time constants from the absorbance

difference spectra over the 690 to 730 nm range. However, this model fails to incorporate the bi-directionality of ET or how the initial charge separation event determines A- B-branch use. The ultimate electron donor is P_{700} irrespective of the two mechanisms.

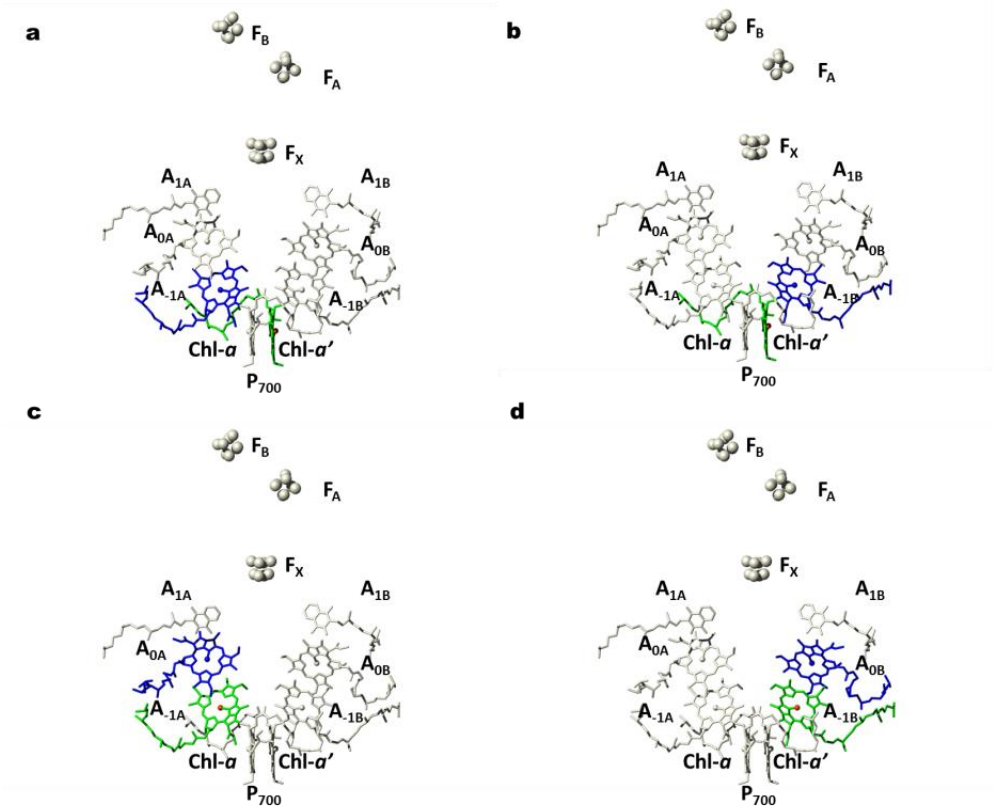

Figure 1-5: PSI reaction center cofactors with proposed sites of initial charge separation in which the photo chemical traps are colored in green (donor) and blue (acceptor). The photochemical traps are defined as, (a) $P_{700}^{+}A_{-1A}^{-}$, (b) $P_{700}^{+}A_{-1B}^{-}$, (c) $A_{-1A}^{+}A_{0A}^{-}$, (d) $A_{-1B}^{+}A_{0B}^{-}$. The PSI reaction center renderings were created from the PDB file 1JB0.

According to electron nuclear double resonance (ENDOR) experiments, the spin density of the unpaired electron on P_{700}^{+} is delocalized asymmetrically over the Chl-*a*/Chl-*a'* dimer (Figure 1-4) in an 80:20 ratio in favor of the Chl-*a*' bound to PsaB. [21, 23] It is well established by optical transient absorption measurements that the appearance of A_1^{-} occurs within ~30 ps. [24-30] The arrival of the electron on the A_1 cofactor begins the convergence of the two branches to the iron sulfur cluster F_X, however the quinones A_{1A}

and A_{1B} have different rates of ET to F_X. The thermodynamic and quantum mechanical properties of the quinone that govern this difference are the main focus of this thesis.

1.5 Electron Transfer Involving the Phylloquinone Cofactor

1.5.1 Room temperature behavior for A_1^- to F_X electron transfer step.

The absorbance change and magnetic resonance signals associated with $P_{700}^+A_1^-$ to $P_{700}^+F_X^-$ ET step in PSI can be seen at room temperature and show a biphasic decay signal with lifetimes of ~200 and 20 ns. About 15 years ago it was first suggested that this behavior might be due to bi-directional electron transfer. [18, 31, 32] Prior to the X-ray structure determination, it was thought that the faster of the two phases might be an artifact of sample preparation, because it was not observed in PSI preparations from cyanobacteria that were isolated with mild detergents but was present in spinach samples prepared with strong detergents. [32] However, a species of *Chlorella* was examined by a new optical technique that had the ability to resolve 5 ns signals for whole cell samples and both lifetimes were observed in the decay of spectral signatures associated with re-oxidation of A_1^-. [33] In later work, it was shown that removal of subunits PsaE and F in combination with harsh detergents leads to a changes in the relative amplitude of the two phases. [34, 35]

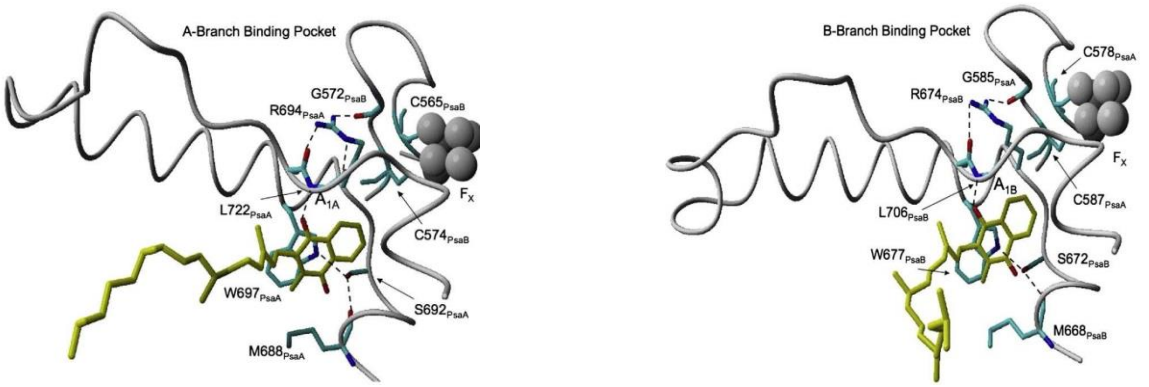

Figure 1-6: View of the A_1 binding site showing the PsaA-W697 (left) and PsaB-W677 (right) π stacking. (Taken from [15]) The phylloquinone cofactor is presented in yellow with its carbonyl oxygen in red. Hydrogen bonding is indicated by the dotted line.

More rigorous understanding of the origin of the two kinetic components for A_1^- oxidation required a genetic approach. Therefore, point mutations to the protein surrounding the quinone binding site were done. According to the 2.5Å crystal structure, the side chains of the tryptophan amino acid residues at positions PsaA-W697 and PsaB-W677 are close enough to the respective phylloquinone cofactors to π stack with the quinone ring (Figure 1-6). [18] Each of the two tryptophan residues was selectively mutated to a phenylalanine to alter the π-stacking in one of the two branches. As a result of these mutations, two things became apparent. First, using pump probe optical absorbance spectroscopy the two lifetimes, 200 and 20 ns, could be associated with a particular branch of electron transfer for the A_1^- to F_X ET step. The oxidation of A_{1A}^- occurs with a lifetime of 200 ns and A_{1B}^- oxidation occurs with a lifetime of 20 ns. Second, the mutations altered the π stacking causing an increase in lifetime from 200 ns to 490 ns for the PsaA-W697F mutant and an increase of the 20 ns phase to 73 ns for PsaB-W677F. Disruption of the π-stacking drives the redox potential of the A_1 cofactor more positive and therefore stabilizes the A_1^- radical anion. These increases in the ET

rates associated with the A_1^- re-oxidation are in agreement with the quantum chemical calculations that predicted an influence of -150 mV from the tryptophan residue on the reduction midpoint potential of A_1. It was now seemingly possible to alter the redox potential of the quinone through point mutations. [18]

1.5.2 The temperature dependence of the A_1^- to F_X ET rate.

Cyanobacterial PSI from *S. elongatus* was used to examine the temperature dependence of the forward electron transfer rates between cofactors A_1^- to F_X (see ref. [36]) using high concentrations of (~40%) glycerol to maintain a glass and avoid light scattering by the sample which can interfere with sensitivity of transient absorption measurements. At room temperature, the decay of the 385 nm semi-quinone signal was simulated with a bi-exponential decay curve with lifetimes of 200 ns and 20 ns. When the temperature is lowered, the 200 ns slow phase lifetime becomes much longer (28 µs at 165 K), but the 20 ns lifetime shows no change. The 20 ns fast phase can only be observed to a temperature of ~180 K at which point no measurable absorbance change can be fit with a 20 ns lifetime. [36] In addition, the 820 nm absorbance change was examined for back reaction and re-reduction of P_{700}^+ to P_{700} to identify if the electron was recombining from the A_1^- cofactor. Below ~165 K the lifetime associated with the A_1^- 385 nm absorbance change for the slow phase was identical to that found for the reduction of P_{700}^+ to P_{700} at the 826 nm absorbance change. The fast phase is only seen in the decay at 385 nm. [36] From these data it can be concluded that the rate of ET from A_{1A}^- to F_X is temperature dependent while the A_{1B}^- to F_X is temperature independent.

1.5.3 Transient EPR of electron transfer in PSI from room (298K) to cryogenic (80K) temperatures

In addition to optical absorbance decay kinetics, time resolved electron paramagnetic resonance spectroscopy (TREPR) provides a unique look into PSI ET. Chapter 3 will cover the theoretical background pertaining to EPR and the origin of spectral features in EPR. The PSI ET generates two detectable strongly correlated electron spins and this correlation persists for several microseconds. During this time, the electron spin eigenstates are populated in a non-equilibrium distribution. This distribution is referred to as spin polarization and results in strong absorptive (A) and emissive (E) signals in the EPR spectrum. Room temperature TREPR measurements of PSI showing the ET between A_1^- and F_X can be seen in Figure 1-7.

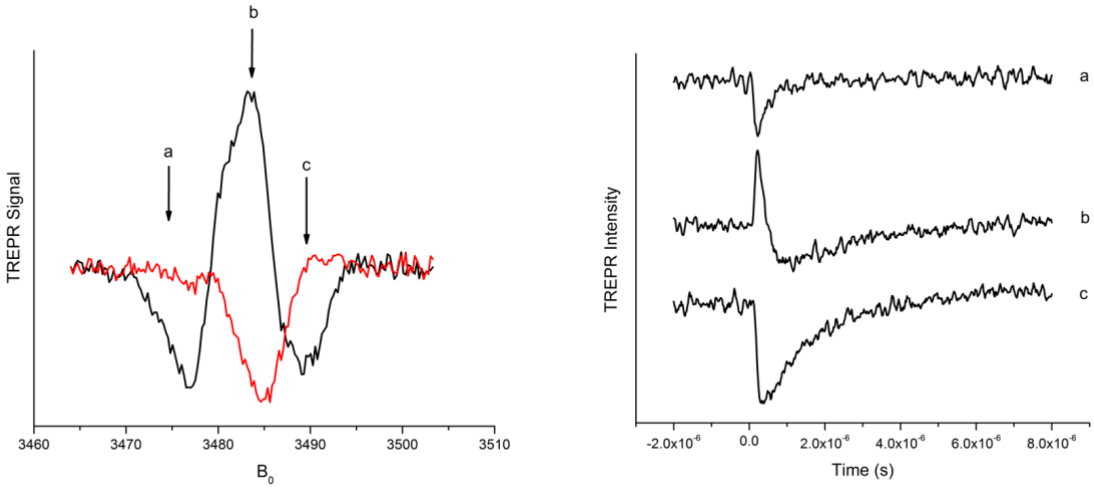

Figure 1-7: (left) Room temperature transient EPR (TREPR) spectra of the spin polarized radical pair $P_{700}^+A_1^-$ (black) at early time after the laser flash to net emission of $P_{700}^+F_X^-$ (red) for wild type cyanobacterium *Synechocystis* sp. PCC 6803. The black spectrum is a spin polarized pattern of emission/absorption/emission moving into the net emission of the red spectrum. (right) The individual transients at field positions indicated a, b and c on the radical pair spectra(left). The signal intensity changes with the ET of A_1^- to F_X and can be fit with a multi-exponential decay curve with an amplitude and rate.

The early spectrum has an E/A/E spin polarization pattern from the radical pair $P_{700}^{+}A_1^{-}$. This spin polarization evolves into the primarily emissive spectrum due to ET and the formation of $P_{700}^{+}F_X^{-}$ with a lifetime of ~200 ns at room temperature. The response time for the EPR spectrometer is 100 ns because of resonator bandwidth and lifetime broadening limitations. Thus, the PsaB-branch radical pair, $P_{700}^{+}A_{1B}^{-}$, cannot be detected directly by EPR spectroscopy since its lifetime is ~20 ns. However, its amplitude can be inferred from the amplitude of $P_{700}^{+}F_X^{-}$ net emission (Figure 1-7 red spectrum) present at early time (Figure 1-7**:** black spectrum). When such experiments are conducted at temperatures below ~180K, the lifetime of the spin polarization pattern of the radical pair $P_{700}^{+}A_1^{-}$ (Figure 1-8) becomes very long (>10 μs) and the emissive signal from $P_{700}^{+}F_X^{-}$ is no longer observed. Comparison with optical data and the microwave power dependence of the signal lifetime shows that the decay of the spin polarization is due to spin relaxation.

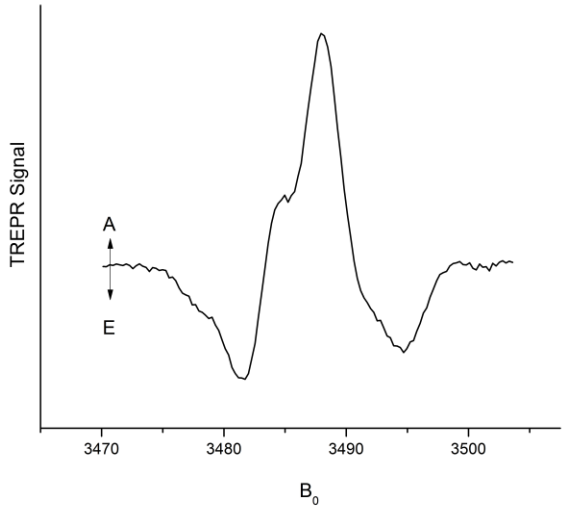

Figure 1-8: Low temperature (80K) transient EPR spectrum of the spin polarized radical pair $P_{700}^{+}A_1^{-}$ from wild type cyanobacterium *Synechocystis* sp. PCC 6803.

The low temperature TREPR spectrum of the spin polarized radical pair $P_{700}^{+}A_1^{-}$ is similar to that of the room temperature spectrum but it has significantly better signal to noise. Interestingly, the low temperature TREPR spectrum of the radical pair $P_{700}^{+}A_1^{-}$ arises only from reversible PsaA-branch ET and there is no contribution from PsaB-Branch ET. This assignment to the A-branch radical pair was made by analyzing the same mutants PsaA-W673F and PsaB-W677F of the cyanobacterium *Synechococcus elongatus* PCC 7942 that were used to demonstrate the bi-directionality of ET in PSI at room temperature. The low temperature TREPR spectrum of $P_{700}^{+}A_1^{-}$ in the PsaA-W697F was different than that of the wild-type, while the spectrum from the PSI of the PsaB-W677F mutant looked identical to that of corresponding wild-type samples. [37] Based on this study it was concluded, the radical pair observed in TREPR experiments at low temperature is almost exclusively as a result of reversible PsaA-branch ET.

1.5.4 Light induced irreversible electron transfer signals detected by CW EPR at low temperature.

In addition to reversible electron transfer between P_{700} and A_{1A}, illumination of frozen PSI samples also results in irreversible transfer of electrons from P_{700} to the terminal iron sulfur clusters F_A and F_B (Figure 1-4). [38, 39] The irreversible ET leads to accumulation of the charge-separated state $P_{700}^{+}[F_A/F_B]^{-}$. The continuous wave (CW) EPR spectrum of this state can be measured at helium cryogenic temperatures (15 K). At higher temperatures the extremely fast spin relaxation of iron (Fe) causes broadening of the spectrum and the signal is not detectable.

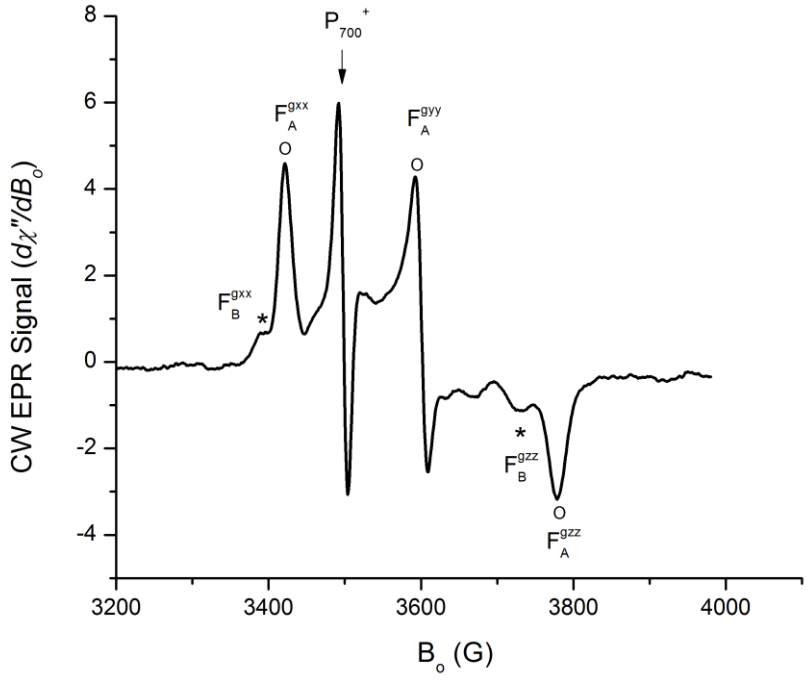

Figure 1-9: X-Band CW EPR spectrum of the light accumulated $(F_A/F_B)^-$ in wild-type *Synechocystis* sp. PCC 6803 at 15 K witnessed by field modulation and lock in detection. The g-tensor for F_A^- (O) and the gxx & gzz of F_B^-(*), as well as the P_{700}^+ g-factor are labeled accordingly.

The light induced X-band CW EPR spectrum of wild type PSI at 15 K can be seen in Figure 1-9. The sample was frozen in the dark with excess sacrificial reductant to ensure P_{700}^+ has been reduced to P_{700} and then illuminated. The spectrum is the combination of multiple static species including P_{700}^+ (3480 Gauss) and F_A^- (O) and F_B^- (*). Several features are observed for the F_A^- and F_B^- signals, because the spectrum is the sum over the random distribution of reaction centers and of orientations present in the sample. The overlapping F_A^- and F_B^- spectra arise from a combination of $P_{700}^+F_A^-$ and $P_{700}^+F_B^-$ which is often written as $P_{700}^+[F_A/F_B]^-$ because both species occur. At higher temperatures (~18 K) more $P_{700}^+F_B^-$ is present while at lower temperatures (~15K) $P_{700}^+F_A^-$ becomes more prevalent. This spectrum (Figure 1-9) is an irreversible signal

$P_{700}^{+}[F_A/F_B]^{-}$ which can remain for days after illuminating the sample. Interestingly, the reversible light-induced TREPR signal of $P_{700}^{+}A_1^{-}$ can also be observed in samples where stable $P_{700}^{+}[F_A/F_B]^{-}$ is present. Indeed the TREPR signals due to reversible ET between P_{700} and A_1 can be observed even after long periods of illumination, i.e. laser flashes at 10 Hz for many hours with little or no decrease in intensity. Together the CW and TREPR data show that there are at least two fractions in the PSI sample which display reversible and irreversible charge separation. At present it is not known why there are several fractions, but because of the thermodynamic differences of the A_{1A} and A_{1B} cofactors, it has been postulated that they may play a role in determining whether reversible and irreversible ET occurs at low temperature.

Clearly, many properties of the ET in PSI, such as the temperature dependence of the rate of ET transfer involving the quinone cofactor, the activity of the two kinetic phases at room temperature compared to the low temperature and the determining step of reversible and irreversible ET from the terminal acceptors F_A and F_B, are not well understood. Thus, further exploration into the dependence of ET behavior on A_1 is needed. This thesis contains an introduction literature review, three chapters of theoretical descriptions and three chapters of research projects.

The published work discussed in Chapter 5 investigates the role of the single hydrogen bond to the A_1 cofactor. By substituting a Thr for the Leu at position 722 of the PsaA subunit, an additional hydrogen bond to A_1 was introduced. The influences of this hydrogen bond are discussed in terms of experimental data and theoretical calculations. The work was able to show the feasibility of the additional H-bond to the A_1 through molecular dynamics and quantum mechanics simulations of the protein. The theoretical

work was able to accurately model the A_1 binding site and gave electron spin density distributions that agreed well with experimental magnetic resonance measurements. The influence of the additional H-bond on ET rates showed an accelerated rate for the PsaA-L722T when compared to wild type for the A_1^- to F_X. The temperature dependence was measured for the A_1^- to F_X ET rate of the PsaA-L722T and showed non-Arrhenius behavior. Possible explanations for the non-Arrhenius behavior are discussed, including the coupling of the rate of ET to the vibrational motion of the protein.

The published work discussed in Chapter 6 involves the quinone exchange of plastoquinone in the *menB* variant for a very high midpoint potential quinone (2,3-dichloro-1,4-naphthoquinone), which affectively blocks ET beyond the A_1 cofactor. This allows the temperature dependence of the branch activity to be studied without added complication of stable charge separation to the iron-sulfur clusters. Characterization of these samples was carried out using various magnetic resonance (CW EPR, TREPR and Pulsed EPR) and transient optical absorbance spectroscopy techniques. The work confirms the incorporation of 2,3-dichloro-1,4-naphthoquinone and shows the ET becomes strongly biased to PsaA-branch at low temperature.

The unpublished work in Chapter 7 addresses the role of the quinone acceptors in the two fractions of PSI complexes showing reversible and irreversible ET at low temperature. The CW EPR spectra of the accumulated P_{700}^+ and $[F_A/F_B]^-$ signals induced by single laser flash turnovers are discussed for the PSI reaction centers from the *menB* variant and wild-type strains of the cyanobacterium *Synechocystis* sp. PCC 6803. The PSI complexes from these two strains have plastoquinone-9 and Phylloquinone, respectively, bound to the A_1 site. The difference in solution midpoint potentials for the two quinones

is ~100 mV. This midpoint potential difference is explored for its possible influence on the two fractions. The data suggest the reversible and irreversible ET past the A_1 cofactor does not have an effect on the amount of ET that leads to trapping. Instead, the rate limiting step is one in which both menB and wild-type share. This leads to the postulate that a distribution of ET rates between the three [4Fe4S] clusters F_X, F_A and F_B are responsible for the different fractions.

1.6 References:

1. Golbeck, J.H., *Structure and Function of Photosystem I.* Annu Rev Plant Phys and Plant Mol Bio, 1992. **43**(1): p. 293-324.
2. Clements, H.F., *Mannose and the First Sugar of Photosynthesis.* Plant Phys, 1932. **7**(3): p. 547-50.
3. Chitnis, P.R., *PHOTOSYSTEM I: Function and Physiology.* Annu Rev Plant Phys & Plant Mol Bio, 2001. **52**(1): p. 593.
4. Melkozernov, A. and R. Blankenship, *Structural and functional organization of the peripheral light-harvesting system in Photosystem I.* Photosynth Res, 2005. **85**(1): p. 33-50.
5. Nelson, N. and C.F. Yocum, *Structure and Function of Photosystems I and II.* Annu Rev Pla Bio, 2006. **57**(1): p. 521-565.
6. Eric, H.J., *Makers of Chemistry*2007: Read Books.
7. Priestley, J., *Experiments and Observations on Different Kinds of Air*1774-86: Cambridge University Press.
8. Sadava, D.E. and H.C. Heller, *Life: The Science of Biology*2008: W. H. Freeman.
9. Subramanyam, R., C. Jolley, D.C. Brune, P. Fromme, and A.N. Webber, *Characterization of a novel photosystem I-LHCI supercomplex isolated from Chlamydomonas reinhardtii under anaerobic (State II) conditions.* FEBS Lett., 2006. **580**(1): p. 233-238.
10. Wang, Q., *Three Step Dissociation and Covalent Stabilization of Phycobilisome*, in *Photosynthesis Research for Food, Fuel and the Future*2013, Springer Berlin Heidelberg. p. 156-166.
11. Wydrzynski, T.J. and K. Satoh, *Photosystem II: The Light-Driven Water:Plastoquinone Oxidoreductase*2005: Springer.
12. Hill, R. and F. Bendall, *Function of the 2 Cytochrome Components in Chloroplasts - Working Hyothesis.* Nature, 1960. **186**(4719): p. 136-137.
13. Jordan, P., P. Fromme, H.T. Witt, O. Klukas, W. Saenger, and N. Kraub, *Three-dimensional structure of cyanobacterial photosystem I at 2.5 A resolution.* Nature, 2001. **411**(6840): p. 909-917.

14. Kruip, J., P.R. Chitnis, B. Lagoutte, M. Rögner, and E.J. Boekema, *Structural Organization of the Major Subunits in Cyanobacterial Photosystem 1: LOCALIZATION OF SUBUNITS PsaC, -D, -E, -F, AND -J.* J Bio Chem, 1997. **272**(27): p. 17061-17069.
15. Srinivasan, N. and J.H. Golbeck, *Protein–cofactor interactions in bioenergetic complexes: The role of the A_{1A} and A_{1B} phylloquinones in Photosystem I.* BBA-Bio, 2009. **1787**(9): p. 1057-1088.
16. Muller, M.G., C. Slavov, R. Luthra, K.E. Redding, and A.R. Holzwarth, *Independent initiation of primary electron transfer in the two branches of the photosystem I reaction center.* Proc. Natl. Acad. Sci. U. S. A., 2010. **107**(9): p. 4123-4128.
17. Li, Y., A. van der Est, M.G. Lucas, V.M. Ramesh, F. Gu, A. Petrenko, S. Lin, A.N. Webber, F. Rappaport, and K. Redding, *Directing electron transfer within Photosystem I by breaking H-bonds in the cofactor branches.* Proc. Natl. Acad. Sci. U. S. A., 2006. **103**(7): p. 2144-2149.
18. Guergova-Kuras, M., B. Boudreaux, A. Joliot, P. Joliot, and K. Redding, *Evidence for two active branches for electron transfer in photosystem I.* P Nat Ac Sci, 2001. **98**(8): p. 4437-4442.
19. Santabarbara, S., A. Jasaitis, M. Byrdin, F.F. Gu, F. Rappaport, and K. Redding, *Additive Effect of Mutations Affecting the Rate of Phylloquinone Reoxidation and Directionality of Electron Transfer within Photosystem I.* Photochem and Photobio, 2008. **84**(6): p. 1381-1387.
20. Sinanoğlu, O., *Modern Quantum Chemistry: Istanbul Lectures*1965: Academic P.
21. Webber, A.N. and W. Lubitz, *P700: the primary electron donor of photosystem I.* BBA-Bio, 2001. **1507**(1–3): p. 61-79.
22. Shelaev, I.V., F.E. Gostev, M.D. Mamedov, O.M. Sarkisov, V.A. Nadtochenko, V.A. Shuvalov, and A.Y. Semenov, *Femtosecond primary charge separation in Synechocystis sp PCC 6803 photosystem I.* Biochim. Biophys. Acta-Bioenerg., 2010. **1797**(8): p. 1410-1420.
23. Käss, H., P. Fromme, H.T. Witt, and W. Lubitz, *Orientation and Electronic Structure of the Primary Donor Radical Cation in Photosystem I: A Single Crystals EPR and ENDOR Study.* J Phy Chem B, 2001. **105**(6): p. 1225-1239.
24. Blankenship, R.E., G. Hastings, F.A.M. Kleinherenbrink, S. Lin, and T.J. McHugh, *Observation of the reduction and reoxidation of the primary electron acceptor in photosystem I.* Biochem, 1994. **33**(11): p. 3193+.
25. Hastings, G., F.A.M. Kleinherenbrink, S. Lin, and R.E. Blankenship, *Time-Resolved Fluorescence and Absorption Spectroscopy of Photosystem I.* Biochem, 1994. **33**(11): p. 3185-3192.
26. Hecks, B., K. Wulf, J. Breton, W. Leibl, and H.W. Trissl, *Primary Charge Separation in Photosystem I: A Two-Step Electrogenic Charge*

Separation Connected with $P_{700}^{+}A_0^{-}$ and $P_{700}^{+}A_1^{-}$ Formation. Biochem, 1994. **33**(29): p. 8619-8624.

27. Brettel, K. and M. H. Vos, *Spectroscopic resolution of the picosecond reduction kinetics of the secondary electron acceptor A_1 in Photosystem I.* FEBS Lett., 1999. **447**(2–3): p. 315-317.
28. Mi, D., S. Lin, and R.E. Blankenship, *Picosecond Transient Absorption Spectroscopy in the Blue Spectral Region of Photosystem I†.* Biochem, 1999. **38**(46): p. 15231-15237.
29. Savikhin, S., W. Xu, P.R. Chitnis, and W.S. Struve, *Ultrafast primary processes in PS I from Synechocystis so. PCC 6803: Roles of P_{700} and A_0.* Biophys J, 2000. **79**(3): p. 1573-1586.
30. Savikhin, S., W. Xu, P. Martinsson, P.R. Chitnis, and W.S. Struve, *Kinetics of Charge Separation and $A_0^{-} \rightarrow A_1$ Electron Transfer in Photosystem I Reaction Centers†.* Biochem, 2001. **40**(31): p. 9282-9290.
31. Brettel, K., *Electron transfer from A_1^{-} to an iron-sulfur center with $t_{1/2}$ = 200 ns at room temperature in Photosystem I Characterization by flash absorption spectroscopy.* FEBS Lett., 1988. **239**(1): p. 93-98.
32. Setif, P. and K. Brettel, *Forward electron transfer from phylloquinone A_1 to iron-sulfur centers in spinach photosystem I.* Biochem, 1993. **32**(31): p. 7846-7854.
33. Bautista, J.A., F. Rappaport, M. Guergova-Kuras, R.O. Cohen, J.H. Golbeck, J.Y. Wang, D. Béal, and B.A. Diner, *Biochemical and Biophysical Characterization of Photosystem I from Phytoene Desaturase and ζ-Carotene Desaturase Deletion Mutants of Synechocystis Sp. PCC 6803: EVIDENCE FOR PsaA- AND PsaB-SIDE ELECTRON TRANSPORT IN CYANOBACTERIA.* J Bio Chem, 2005. **280**(20): p. 20030-20041.
34. Agalarov, R., M. Byrdin, F. Rappaport, G.Z. Shen, D.A. Bryant, A. van der Est, and J.H. Golbeck, *Removal of the PsaF Polypeptide Biases Electron Transfer in Favor of the PsaB Branch of Cofactors in Triton X-100 Photosystem I Complexes from Synechococcus sp PCC 7002.* Photochem and Photobio, 2008. **84**(6): p. 1371-1380.
35. van der Est, A., A.I. Valieva, Y.E. Kandrashkin, G.Z. Shen, D.A. Bryant, and J.H. Golbeck, *Removal of PsaF alters forward electron transfer in photosystem I: Evidence for fast reoxidation of Q(K)-A in subunit deletion mutants of Synechococcus sp PCC 7002.* Biochem, 2004. **43**(5): p. 1264-1275.
36. Schlodder, E., K. Falkenberg, M. Gergeleit, and K. Brettel, *Temperature Dependence of Forward and Reverse Electron Transfer from A_1^{-}, the Reduced Secondary Electron Acceptor in Photosystem I†.* Biochem, 1998. **37**(26): p. 9466-9476.
37. Boudreaux, B., F. MacMillan, C. Teutloff, R. Agalarov, F. Gu, S. Grimaldi, R. Bittl, K. Brettel, and K. Redding, *Mutations in Both Sides of the Photosystem I Reaction Center Identify the Phylloquinone*

Observed by Electron Paramagnetic Resonance Spectroscopy. J Bio Chem, 2001. **276**(40): p. 37299-37306.

38. Brettel, K., I. Sieckmann, P. Fromme, A. van der Est, and D. Stehlik, *Low-temperature EPR on single crystals of photosystem I: study of the iron-sulfur center F_A*. BBA-Bio, 1992. **1098**(2): p. 266-270.
39. Teutloff, C., W. Hofbauer, S.G. Zech, M. Stein, R. Bittl, and W. Lubitz, *High-frequency EPR studies on cofactor radicals in photosystem I*. Appl. Magn. Reson., 2001. **21**(3-4): p. 363-379.

Chapter 2 Examining Electron Transfer by the Rate of the Reaction

2.1 Arrhenius Behavior of Chemical Reactions

The PSI ET cofactors are coordinated by a large matrix of amino-acids. It is not well understood how the protein-cofactor interactions govern the rate of the $P_{700}^{+}A_1^{-}$ to $P_{700}^{+}F_X^{-}$ step. (Figure 2-1)

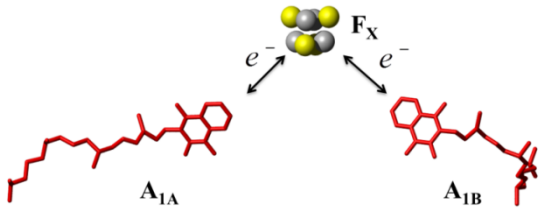

Figure 2-1: The PSI $P_{700}^{+}A_1^{-}$ to $P_{700}^{+}F_X^{-}$ ET step. The quinone cofactors A_{1A} and A_{1B} of the PsaA and PsaB-branch, respectively, are shown along with the [4Fe4S] cluster cofactor F_X. Figure generated from the PDB file 1JB0.

To examine this interaction it is necessary to know the relationship of the energetics and the ET rate. For a chemical reaction this relationship is well known. [1] A chemical reaction can be written as an activated process described by the Arrhenius equation (2.1) that relates the forward rate, k_f, to a surmountable barrier called the activation energy, ΔG^*. [1]

$$k_f = Ae^{-\Delta G^*/k_b T} \tag{2.1}$$

$$\log(k_f) = -\frac{\Delta G^*}{k_b}\frac{1}{T} + \log(A) \tag{2.2}$$

where k_b is the Boltzmann constant and T is temperature in Kelvin. The activation energy, ΔG^*, is a constant barrier and when sufficient thermal energy ($k_b T$) is available the reaction proceeds, as seen in Figure 2-2 (left). The probability of a molecule reacting is governed by the Boltzmann distribution which describes the population of molecules with a given energy at a given temperature. [2] The rate increases to a maximum when the thermal energy $k_b T$ is much greater than the ΔG^*.

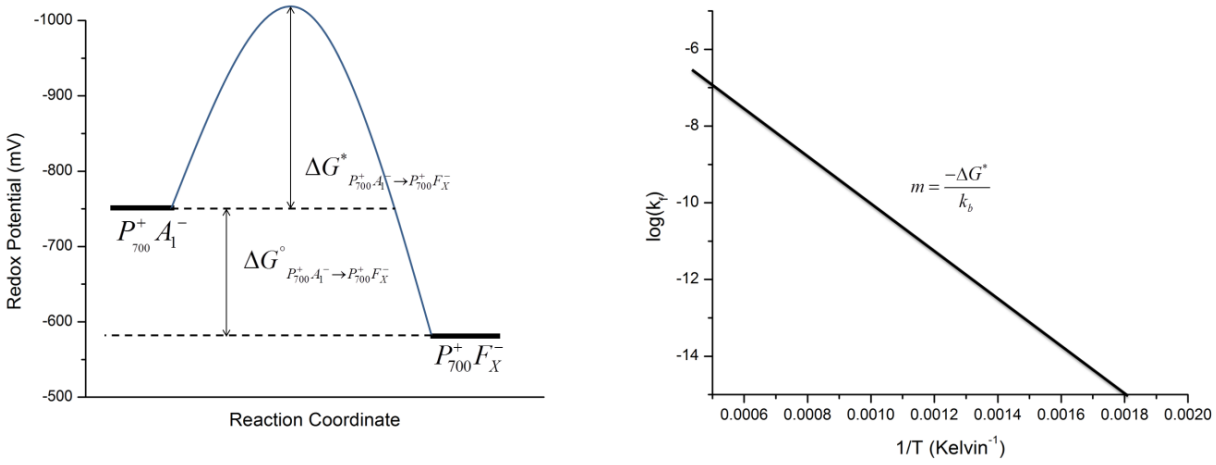

Figure 2-2: (left) A classical representation of a chemical reaction going from the donor state, $P^+_{700}A^-_1$, to the acceptor state, $P^+_{700}F^-_X$, with an activation energy, ΔG^*, and Gibbs free energy, ΔG°. (right) The Arrhenius plot which shows the linear relationship between $\log(k_f)$ and $\frac{1}{T}$ with a slope $\frac{\Delta G^*}{k_b}$.

The pre-exponential term A is defined as the inherent rate of the reaction when $\Delta G^* = 0$. This can easily be seen in the linear dependence of equation (2.2) in Figure 2-2 (right). The slope of the line is $-\frac{\Delta G^*}{k_b}$ and $\log(A)$ is the y-intercept. These parameters which dictate Arrhenius behavior are the basis for Marcus Theory of ET.

2.2 Marcus Theory of Electron Transfer Reactions

2.2.1 Electron Tunneling in Biological Systems

Electron transfer reactions through protein are different than the gas and liquid state reactions studied by Arrhenius. The protein medium made up of amino acids which form continuous scaffolding. The protein medium is often described by a dielectric constant because of its uniform electronic properties and in addition has small nuclear frequency bandwidth. [3] The cofactors which perform the electron transfer reactions are placed at distances relative to one another for efficient transferring of the electron within this protein medium. The electron can be transported over large distances (> 20 Å) and the rate can increase 10^{12} fold by increasing the number of cofactors and decreasing the distance between them. However, in some cases the distance between the cofactors is further than the van der Waals radius of the cofactor, which is approximately 4 Å for most biologic molecules. In a classical picture, the electron is localized at the potential energy surface at the cofactor boundary. In the open space beyond the cofactors' van der Waal radius, the potential energy is not sufficient to support the high energy electron and so electron transfer between cofactors would not occur. However, in a quantum mechanical picture, the electron can still be transferred by electron tunneling. The electron tunneling was first described in biological systems by Devault et al [4] where the

ET reaction could still occur at cryogenic temperatures where available k_bT was insufficient. Rudolph A. Marcus developed a theory (Marcus Theory [5, 6]) based on the chemical reaction rate description of Arrhenius and the assumption that electron transfer occurs by tunneling. An ET rate described by equation (2.3) involves two parameters which are simplified to the electronic coupling V^2 and the Franck-Condon factor, FC. In comparison to the Arrhenius equation, the electronic coupling will describe the inherent maximum rate of the reaction and the FC factor describes the thermal dependence.

$$k_{\mathrm{ET}} = \frac{4\pi^2}{h} V^2 \,\mathrm{FC} \tag{2.3}$$

2.2.2 The Classical Marcus Equation

The classical Marcus equation (2.4) describes a rate dependence on the electronic coupling between donor and acceptor and a temperature dependent energetic barrier. The electronic coupling of an electronic transition within a molecule from one orbital to another is dependent on the spatial distribution of the electron and an energy requirement. The spatial component of initial and final state wave-functions of the electron describes the overlap between them and is described by the electronic coupling term, V^2, and the coefficient $\frac{4\pi^2}{h}$ seen in equation (2.4).

$$k_{\mathrm{ET}} = \frac{4\pi^2}{h} V^2 \,\mathrm{FC} \tag{2.4}$$

where,

$$V^2 = \left\langle \Psi^{initial}_{(\mathrm{x,y,z})el} \mid \Psi^{final}_{(x,y,z)el} \right\rangle^2 \tag{2.5}$$

$$FC = \frac{1}{\sqrt{4\pi\lambda k_b T}} \exp^{-(\Delta G^*/k_b T)} \tag{2.6}$$

and

$$\Delta G^* = \frac{(\lambda + \Delta G^o)^2}{4\lambda} \tag{2.7}$$

The rate dependence on available energy, which is necessary to promote the electron to another orbital, is contained within the FC factor, because the nuclei do not move during the electron transfer. Thermal fluctuations will manifest into nuclear vibrational motion and in turn changes in the electron's degrees of freedom. A classical harmonic oscillator (CHO) is used to map the energetic surface described by these motions (Figure 2-3 left) and the crossing point of the initial and final state CHO will represent the position of the nuclei at which no energy is required to transfer the electron.

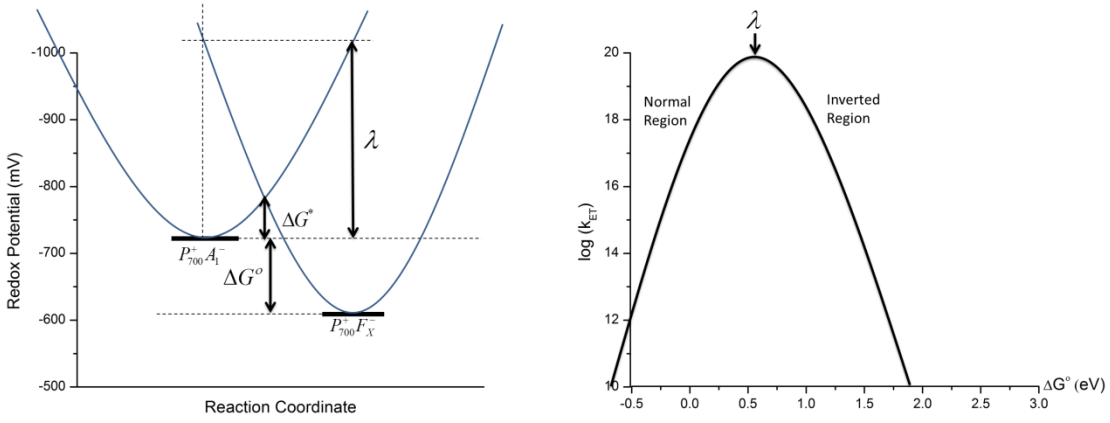

Figure 2-3: (left) Classical Marcus Theory description of exergonic ET for a donor state, A_1^- , to acceptor state, F_X , with reorganization energy, λ , the activation energy, ΔG^* , and Gibbs free energy, ΔG^o. (right) The log(k_{ET}) plotted versus the Gibbs free energy ΔG^o according to Marcus Theory for a general reaction forms the inverted parabola. The maximum rate occurs at λ. The

values of ΔG^o smaller than λ describe the "normal region" while values of ΔG^o larger than λ describe the inverted region to the right.

2.2.2.1 The Driving Force, ΔG^o

The activation energy, ΔG^*, is in part dictated by the driving force Gibbs free energy, ΔG^o. The ΔG^o is put in terms of the difference in reduction midpoint potential of the donor-acceptor states because the ET reaction involves the transfer of an electron. The ET reaction is comprised of the reduction and oxidation of two species. These half-reactions are described in equation (2.8).

$$\begin{aligned} E^{reduction} &= F_X + e^- \rightarrow F_X^- \\ E^{oxidation} &= A_1^- \rightarrow A_1 + e^- \end{aligned} \tag{2.8}$$

The difference in half-reaction midpoint potentials, ΔE, relates to the driving force by the following equation:

$$\Delta G^o = nF\Delta E_{(E^{oxidation} - E^{reduction})} \tag{2.9}$$

where n is the number of moles of electrons transferred and F is the Faraday constant with a value of $9.64853399(24)\times 10^4 C/mol$ [7]. The driving force is increased by having a more electron poor acceptor relative to the donor.

2.2.2.2 The Reorganization Energy, λ

The activation energy, ΔG^*, is also described by the reorganization energy, λ, which can be seen in Figure 2-3 (left). If we consider the donor state $P_{700}{}^+A_1{}^-$ converting to the acceptor state $P_{700}{}^+F_X{}^-$, the vibrational motion of the nuclei of the donor state must adjust to form the potential energy surface of the acceptor state. The change in potential

energy that occurs when the reaction coordinate is changed from the value at the minimum of the donor state potential to the minimum of the acceptor state potential is the reorganization energy. The reorganization energy for protein medium lies in the range of 0.7 to 1.0 V.

2.2.2.3 The ET rate dependence on the Frank-Condon factor.

The dependence of the logarithm of the ET rate, k_{ET}, on ΔG^o is a parabola. (Figure 2-3 right) The "normal region" of the parabola is for those values of $-\Delta G^o$ less than λ . In this region the rate increases as the magnitude of ΔG^o increases, whereas $-\Delta G^o$ values larger than λ form the "inverted region" in which the rate decreases as the magnitude of ΔG^o increases. The maximum ET rate is reached at the value of $-\Delta G^o = \lambda$ for the reaction. In this thesis the energetics of the $P_{700}{}^{+}A_1{}^{-}$ to $P_{700}{}^{+}F_X{}^{-}$ step was studied by changing the reduction midpoint potential of the cofactor A_1 in two ways. In Chapter 5, point mutations of the amino acid residue PsaA-L722 are discussed. In Chapter 6, the exchange of the native phylloquinone with a foreign naphthoquinones is discussed.

2.2.2.4 The ET rate dependence on Electron Tunneling

The addendum to classical Marcus theory is a quantum mechanical treatment which does not change the structure of the classical Marcus equation. In equation (2.4) the vibrational motion is described classically. In a quantum mechanical treatment the vibrational energy of the nuclei is quantized and the vibrational wave-function extends beyond the boundaries of the molecular potential energy surface (Figure 2-4). In classical Marcus theory the rate will eventually become zero for a reaction when the temperature

goes to zero. However, according to quantum mechanics the minimum vibrational energy is that of the lowest vibrational state (the zero-point energy). [8]

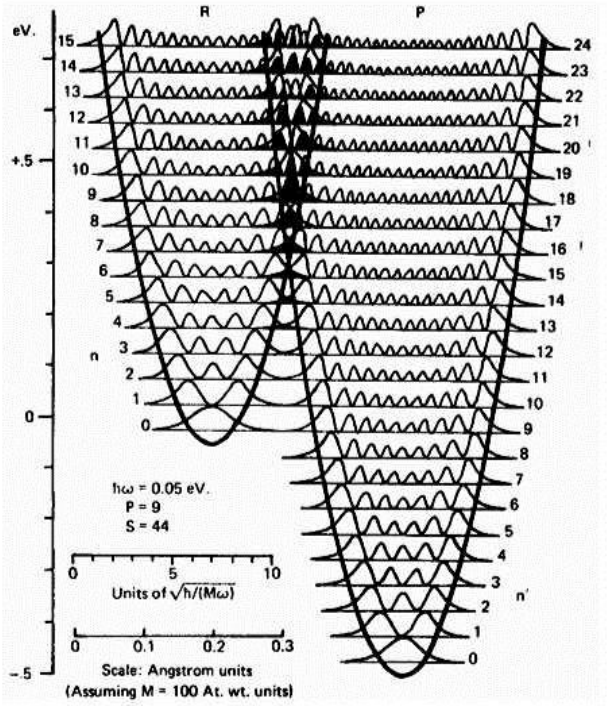

Figure 2-4: The quantum mechanical description of the vibrational overlap between reactant and product. The figure was taken from "Marcus Theory for Electron Transfer a short introduction" by Minoia Andrea.

2.2.3 The Hopfield Equation

Modifications to classical Marcus theory were made to include the high frequency vibrational modes of the protein that the ET rate can couple to. In the adiabatic case described by Hopfield et. al. the rate was shown to include thermal dependence of the electron tunneling. Lower energy vibrational states are not expected to influence the rate because they correspond to slow motions and the ET reaction occurs before the nuclei have gone through one period of oscillation. The Hopfield equation describes the rate dependence coupled to a single vibrational mode $\hbar\omega$ and is shown below.

$$k_{ET} \propto \frac{1}{\sqrt{2\pi\lambda\hbar\omega \; coth(\hbar\omega / 2k_bT)}} \exp\left\{-\frac{(\Delta G^0 + \lambda)^2}{2\lambda\omega \; coth(\hbar\omega / 2k_bT)}\right\} \qquad (2.10)$$

The Hopfield equation shows that when k_bT is small compared to $\hbar\omega$ the *coth* terms approach a value of 1 and the rate becomes independent of temperature. At high temperature $coth(\hbar\omega / 2k_bT) \approx 2k_bT / \hbar\omega$ and equation (2.10) becomes equivalent to the classical Marcus equation (2.4). The Hopfield equation is employed to explain the non-Arrhenius behavior of the rate for the $P_{700}{}^{+}A_1{}^{-}$ to $P_{700}{}^{+}F_X{}^{-}$ step in several PSI samples which include wild type and the samples with point mutations to PsaA-L722 of the A_1 cofactor-protein coordination site, which is discussed in more detail in Chapter 5.

2.2.4 The Moser-Dutton Ruler

The dependence of the ET rate on the factors in the Marcus Equation was investigated extensively with various ET protein samples. [5, 6, 9-12] The factors that were deemed important are the driving force, the distance between cofactors and the reorganization energy, because when combined they can sufficiently define the reaction directionality. [10] The empirical formalism derived by Moser and Dutton et.al. [10] can be seen below:

$$\log k_{ET}^{exer} = 15 - 0.6(R - 3.6) - 3.1\frac{(\Delta G^o + \lambda)^2}{\lambda} \qquad (2.11)$$

The leading value 15 is associated with the maximum rate. As an estimate for the rate, the frequency of visible light, which is roughly the rate of an intermolecular ET reaction, can be taken. Those wavelengths of the blue region that drive photosystems have a frequency of 10^{15} s^{-1}.

The electronic coupling term was examined for those reactions where $-\Delta G^{o} = \lambda$ and at low temperature in order to study the rate dependence without thermal dependencies from the FC factor. The value 0.6 is the maximum value associated with the β [10] term which describes the distance dependence for the propagation of the electronic wave-function through protein medium. In a vacuum this β term is zero. The radius, R, is the distance between the donor-acceptor cofactors and 3.6 is an average of the van der Waals radius for cofactor molecules.

2.3 Current energetics for the $P_{700}^{+}A_1^{-}$ to $P_{700}^{+}F_X^{-}$ step.

Quinones are commonly used in physiological environments as electron carriers because of their ability to stabilize charge. However, in PSI, the two quinones act as highly reducing intermediates in the electron transfer pathway. The reduction midpoint potential of phylloquinone in aprotic solvents such as dimethyl formamide (DMF) is measured to be -400 mV against the standard hydrogen electrode (SHE). In contrast, the redox potentials of phylloquinone in the A_{1A} and A_{1B} binding sites of PSI are currently estimated to be -671 mV and -844 mV [13] (Figure 2-5), respectively. Moreover, the presence of a single hydrogen bond between the A_1 cofactor and the respective adjacent protein backbone [14, 15] is estimated to shift the potential 83mV and 190mV more positive than it would otherwise be. The use of a molecular "electron sink" in the ET pathway and the large change in redox potential caused by the protein environment has raised some interesting and currently unanswered questions as to why the quinone was retained as PSI evolved and how the influence of a protein framework governs ET.

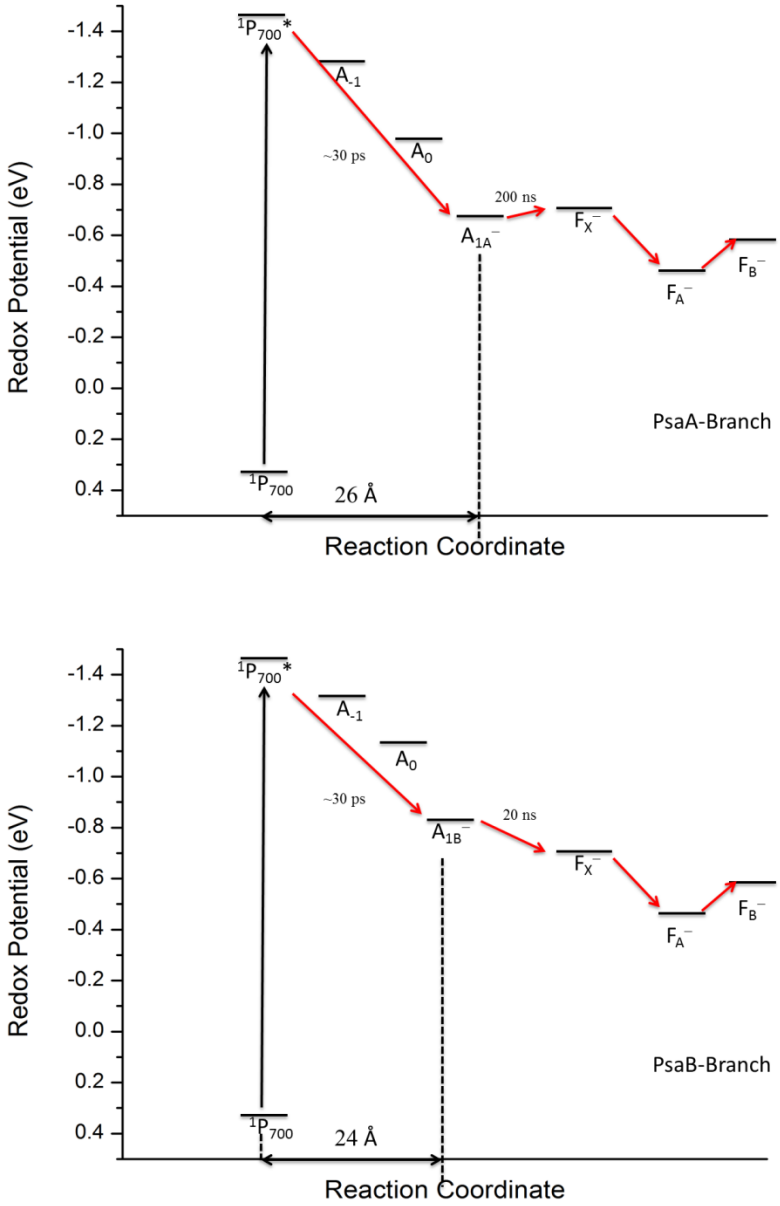

Figure 2-5: Room temperature electron transfer pathways within the PSI reaction center with known lifetimes of the A_1^- to F_X ET rate for the (top) PsaA-Branch and the (bottom) PsaB-Branch for *Synechocystis* sp. PCC 6803. Distances between the P_{700}^+ and A_1^- radicals for PsaA and PsaB are 26 and 24 Å, respectively.

The lifetime of the charge separated state, $P_{700}^+A_1^-$, is longer than the initial states by 3 to 4 order of magnitude with lifetimes of 20-200 ns (Figure 2-5). The difference in the

$P_{700}^{+}A_{1A}^{-}$ and $P_{700}^{+}A_{1B}^{-}$ ET rates suggests differences in the barriers and/or electronic couplings that govern the individual ET reaction rates. Changes to the factors governing the $P_{700}^{+}A_{1}^{-}$ to $P_{700}^{+}F_{X}^{-}$ ET rate k_{ET} were induced in two ways for this thesis. First, in Chapter 5, the protein-cofactor interaction is changed by point mutation to the PsaA-L722 residue. Then in Chapter 6, the Gibbs free energy of the A_{1}^{-} to F_{X}^{-} step was changed by introducing a foreign quinone with a different reduction midpoint potential into the A_1 binding sites. To study the effect of these changes two methods are employed. The transient absorbance and electron paramagnetic resonance spectroscopic techniques are described for clarity of the following chapters.

2.4 Transient Optical Absorbance Spectroscopy Technique

Transient optical techniques are used to observe the time dependence of absorption changes. (Figure 2-6) After an actinic flash of a laser, radical ions are produced during PSI electron transfer. The absorbance profiles of a cofactor and its radical ion form are different. Once a population of radical ion species is generated its presence can be probed with a secondary laser source. This transient secondary signal is then digitized for exponential decay curve fitting.

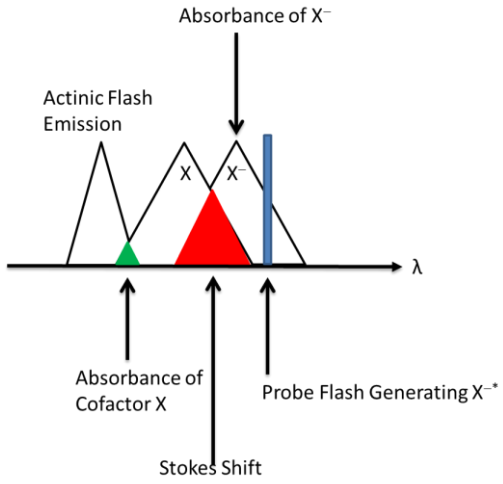

Figure 2-6: Cartoon depicting the transient optical techniques of pumping a species with actinic flash and probing the excited species through stimulated emission for decay kinetic fitting as a function of wavelength and varying the timing for the pump probe sequence.

2.5 Transient Electron Paramagnetic Resonance Spectroscopy Technique

Unfortunately, the spectral overlap of the absorbance changes associated with energy and electron transfer in PSI make it difficult to assign all the rates to particular reactions. PSI ET is an ideal candidate for transient electron paramagnetic resonance spectroscopy (TREPR) to complement the transient optical technique. Not only does TREPR follow provide time resolved signals, but can also provide structural information about the ET species from which the spectrum arises as seen in Chapter 1. A more complete description of EPR signals is described in the following chapter.

2.6 References

1. Chang, R., *General Chemistry*1986: Random House.
2. Engel, T. and P. Reid, *Thermodynamics, Statistical Thermodynamics, and Kinetics*2013: Pearson.
3. Est, J.G.A., *The Biophysics of Photosynthesis*: Springer New York, New York, NY.
4. Chance, B., D. Devault, W.W. Hildreth, W.W. Parson, and Nishimur.M, *Early Chemical Events in Photosynthesis - Kinetics of Oxidation of Cytochromes of Types C or F in Cells Chloroplasts and Chromatophores*. Brookhaven Sym Biol, 1966(19): p. 115-&.

5. Marcus, R.A., *Analytical Mechanics of Chemical Reactions. IV. Classical Mechanics of Reactions in Two Dimensions.* J Chem Phys, 1968. **49**(6): p. 2617-2631.
6. Marcus, R.A. and N. Sutin, *Electron Transfers in Chemistry and Biology.* BBA, 1985. **811**(3): p. 265-322.
7. Griffiths, D.J., *Introduction to Electrodynamics*1999: Prentice Hall.
8. Griffiths, D.J., *Introduction to quantum mechanics*. 2nd ed2005, Upper Saddle River, NJ: Pearson Prentice Hall. ix, 468 p.
9. Hopfield, J.J., *Electron-Transfer Between Biological Molecules by Thermally Activated Tunneling.* Proc. Natl. Acad. Sci. U. S. A., 1974. **71**(9): p. 3640-3644.
10. Moser, C.C., J.M. Keske, K. Warncke, R.S. Farid, and P.L. Dutton, *Nature of Biological Electron Transfer.* Nature, 1992. **355**(6363): p. 796-802.
11. Santabarbara, S., P. Heathcote, and M.C.W. Evans, *Modelling of the electron transfer reactions in Photosystem I by electron tunnelling theory: The phylloquinones bound to the PsaA and the PsaB reaction centre subunits of PS I are almost isoenergetic to the iron–sulfur cluster F_X.* BBA-Bio, 2005. **1708**(3): p. 283-310.
12. Weber, S., T. Biskup, A. Okafuji, A.R. Marino, T. Berthold, G. Link, K. Hitomi, E.D. Getzoff, E. Schleicher, and J.R. Norris, *Origin of Light-Induced Spin-Correlated Radical Pairs in Cryptochrome†.* J Phy Chem B, 2010. **114**(45): p. 14745-14754.
13. Ptushenko, V.V., D.A. Cherepanov, L.I. Krishtalik, and A.Y. Semenov, *Semi-continuum electrostatic calculations of redox potentials in photosystem I.* Photosynth Res, 2008. **97**(1): p. 55-74.
14. Jordan, P., P. Fromme, H.T. Witt, O. Klukas, W. Saenger, and N. Kraub, *Three-dimensional structure of cyanobacterial photosystem I at 2.5 A resolution.* Nature, 2001. **411**(6840): p. 909-917.
15. Ben-Shem, A., F. Frolow, and N. Nelson, *Crystal structure of plant photosystem I.* Nature, 2003. **426**(6967): p. 630-635.

Chapter 3 Electron Paramagnetic Resonance (EPR)

Following photo-excitation of PSI antenna Chl-*a* molecules, the radicals generated by charge separation and ET can be studied by electron paramagnetic resonance (EPR) spectroscopy. During an EPR experiment, a sample containing paramagnetic species (i.e. free radicals, biradicals, transition metals ions) is placed in the presence of a strong static magnetic field, $\mathbf{B_o}$. The unpaired electrons interact with the strong field according to the orientation of their magnetic dipole moment or spin state which is proportional to the spin angular momentum [1, 2] of the electron. The spin of a free electron, $S = \frac{1}{2}$, can align with the field $\uparrow(\alpha)$ or against $\downarrow(\beta)$ as demonstrated by the Stern-Gerlach experiment [3] giving rise to $2S+1$ spin states. While in the presence of the $\mathbf{B_o}$ field, a second applied magnetic field, $\mathbf{B}_1$, of the microwave drives the electron to transition from one spin state to another. The transition between the electron spin states leads to an absorption or emission of the microwave. Hollow tubes called waveguides contain and channel the microwaves to convey the spin transition signals from the sample to the detector. A resonator cavity at the terminus of the waveguide establishes a standing wave which amplifies the transition signals. When the electron absorbs the microwave during spin transitions, the standing wave is changed. The changes are compared against an in-phase reference microwave. These microwave signals are converted into electrical signals by a diode detector before a computer receives the electrical signals and converts them into digital values that can be plotted against the magnetic field to give a spectrum. [4]

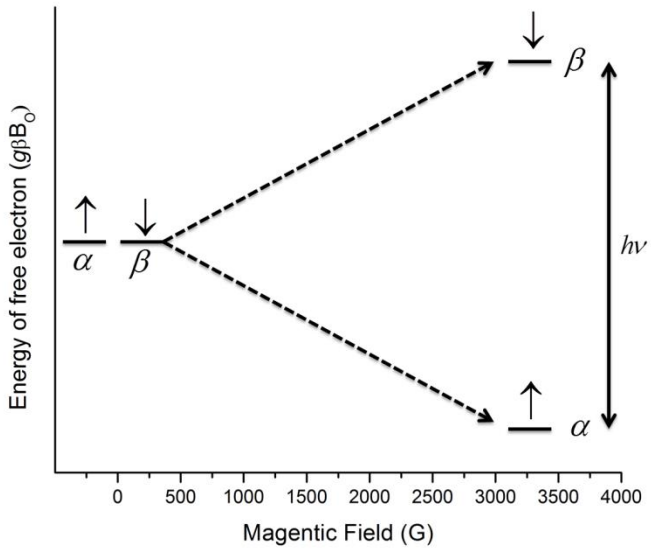

Figure 3-1: A plot of the free electron transition energy as a function of the applied magnetic field, $\mathbf{B_o}$, for the spin up (α) to spin down (β) state.

In an EPR experiment the microwave frequency is kept constant and the magnetic field, $\mathbf{B_o}$, is varied. The energy separation, $\Delta E_{\alpha/\beta}$, of the spin states increases with increasing magnetic field. When the energy separation is equal to the energy of the microwave photons the transition occurs as shown in Figure 3-1. Neighboring nuclei to which the electron is coupled and $\mathbf{B_o}$ will influence the transition. The spin state of an electron is an entirely quantum mechanical property and has no classical description. However, spin angular momentum is to a good approximation directly proportional to the magnetic dipole moment, $\boldsymbol{\mu}_e$, which is created by the spinning electron rotating in an electromagnetic field and is equated in the following way. [5]

$$\boldsymbol{\mu}_e = \mathbf{g}_e \beta_e \mathbf{S} \tag{3.1}$$

where $\mathbf{g}_e$ is the proportionality constant called the g-factor of an electron and

$\beta_e = \frac{e\hbar}{2m_e} = \left(9.27400968(20) \times 10^{-24} \frac{\text{J}}{\text{Tesla}} \right)$ is the Bohr Magneton of the free electron. The difference in energy between the two states is quantifiable by equation (3.2) and is visually described by Figure 3-1.

$$\Delta E = h\nu = \mathbf{g}_e \beta_e \mathbf{B_o} \tag{3.2}$$

The quantification of the spin states are described by the spin Hamiltonian.

3.1 The Radical Pair Spin Hamiltonian.

The radical pair generated during PSI ET consists of two weakly coupled electron spins (a and b) separated at a distance, $\mathbf{r}$. They share a strong correlation because they originate from the same primary donor singlet state. [6] The formation of the radical pair $P_{700}^{+}A_1^{-}$ occurs within 30 ps, which is too fast for any differences between the electron's precession frequencies to have occurred within the radical pair or the precursors. [7] Therefore, the radical pair $P_{700}^{+}A_1^{-}$ is said to be a pure singlet state of a and b. To determine the energy of the radical pair spin eigenstates and understand the spectral lines for the $P_{700}^{+}A_1^{-}$ radical pair, a Hamiltonian which operates on the electron spin wave-function must be created. The spin Hamiltonian for a radical pair is written as

$$\hat{H}_{\text{RP}} = \hat{H}_{\text{Za}} + \hat{H}_{\text{Zb}} + \hat{H}_{\text{Dip}} + \hat{H}_{\text{EX}} + \hat{H}_{\text{HFC}} \tag{3.3}$$

where $\hat{H}_{Za(b)}$ describe the Zeeman energy of electron spins interacting with the applied magnetic field, $\hat{H}_{\mathrm{Dip}}$ is the through space magnetic dipole interaction between the two electrons, $\hat{H}_{\mathrm{EX}}$ is the spin-spin exchange interaction between the two electrons and $\hat{H}_{\mathrm{HFC}}$ is the hyper-fine coupling interaction of the unpaired spin with nearby nuclear spins. [7-11]

$$\begin{aligned}
\hat{H}_{\mathrm{Za}} &= \mathbf{g}_{eff}^{a}\,\beta\,\mathbf{B}_{\mathrm{o}}\,\hat{\mathbf{S}}^{a} \\
\hat{H}_{\mathrm{Zb}} &= \mathbf{g}_{eff}^{b}\,\beta\,\mathbf{B}_{\mathrm{o}}\,\hat{\mathbf{S}}^{b} \\
\hat{H}_{\mathrm{HFC}} &= \mathbf{S}\cdot\mathbf{A}\cdot\mathbf{I} \\
\hat{H}_{\mathrm{EX}} &= J(\frac{1}{2}+2\hat{\mathbf{S}}\cdot\hat{\mathbf{S}}) \\
\hat{H}_{\mathrm{Dip}} &= \hat{\mathbf{S}}\cdot\mathbf{D}\cdot\hat{\mathbf{S}}
\end{aligned} \tag{3.4}$$

To describe the EPR spectrum of the photo-induced radical pairs, the energies and eigenfunctions of Hamiltonians shown in (3.4) must be obtained. There are two possible choices for the spin basis functions which are the product of the two spin states α and β or the singlet-triplet basis. The initial state of our radical pair is a singlet and so the singlet-triplet basis will be used. The four singlet-triplet basis-functions can be seen below in equation (3.5).

$$\begin{aligned}
|S\rangle &= \frac{1}{\sqrt{2}}(|\alpha\beta\rangle - |\beta\alpha\rangle) \\
|T_{+}\rangle &= |\alpha\alpha\rangle \\
|T_{o}\rangle &= \frac{1}{\sqrt{2}}(|\alpha\beta\rangle + |\beta\alpha\rangle) \\
|T_{-}\rangle &= |\beta\beta\rangle
\end{aligned} \tag{3.5}$$

where $|S\rangle$ is the singlet and $|T_+\rangle, |T_o\rangle, |T_-\rangle$ are the triplet spin state basis-functions. [5, 12]

3.2 The Zeeman Interaction

The Zeeman interaction is defined as the interaction between the external field, $\mathbf{B_o}$, and the unpaired electron. The radical pair is made up of two spins separated by ~25 Å. [5, 12] At this distance, the coupling between the spins is weak. It is convenient for the Hamiltonian to be in terms of individual spins and are distinguished by the superscripts, a and b. The Zeeman interaction Hamiltonian is:

$$\hat{H}_Z = \underbrace{\mathbf{g}_{eff}^{a} \beta \mathbf{B}_o}_{\omega^a} \hat{\mathbf{S}}_Z^a + \omega^b \hat{\mathbf{S}}_Z^b \tag{3.6}$$

where $\mathbf{g}_{eff}$ is the orientation dependent proportionality constant of the electron in the field $\mathbf{B_o}$ which also accounts for changes of the spin's angular momentum created by coupling to the orbital angular momentum of the electron. [4, 6, 7]

$$\begin{aligned} \mathbf{g}_{eff} &= \sin^2\theta\cos^2\phi g_{xx} + \sin^2\theta\sin^2\phi g_{yy} + \cos^2\theta g_{zz} \\ &+2\sin^2\theta\cos\phi\sin\phi g_{xy} + 2\sin\theta\cos\theta\cos\phi g_{xz} + 2\sin\theta\cos\theta\sin\phi g_{yz} \end{aligned} \tag{3.7}$$

The angles θ and ϕ are the polar and azimuthal angles, respectively, of the $\mathbf{B_o}$ oriented in the frame of the principle axes of, $\mathbf{g}$. The terms $g_{xx}, g_{yy}, g_{zz}, etc$ refer to the terms of the second rank $\mathbf{g}$-tensor[2]. The Zeeman Hamiltonian operates on the spin basis functions in the following way.

$$\hat{H}_{\mathrm{Z}}\left|T_{+}\right\rangle = \hat{H}\left|\alpha\alpha\right\rangle = \frac{1}{2}(\omega^{a}+\omega^{b})\left|T_{+}\right\rangle \tag{3.8}$$

$$\begin{aligned}\hat{H}_{\mathrm{Z}}\left|T_{o}\right\rangle &= \hat{H}\frac{1}{\sqrt{2}}(\left|\alpha\beta\right\rangle+\left|\beta\alpha\right\rangle)\\ &= \frac{1}{\sqrt{2}}[(\frac{1}{2}\omega^{a}-\frac{1}{2}\omega^{b})\left|\alpha\beta\right\rangle+(-\frac{1}{2}\omega^{a}+\frac{1}{2}\omega^{b})\left|\beta\alpha\right\rangle]\\ &= \frac{1}{2}(\omega^{a}-\omega^{b})\left|S\right\rangle\end{aligned} \tag{3.9}$$

$$\hat{H}_{\mathrm{Z}}\left|S\right\rangle = \hat{H}\frac{1}{\sqrt{2}}(\left|\alpha\beta\right\rangle-\left|\beta\alpha\right\rangle) = \frac{1}{2}(\omega^{a}-\omega^{b})\left|T_{o}\right\rangle \tag{3.10}$$

$$\hat{H}_{\mathrm{Z}}\left|T_{-}\right\rangle = \hat{H}\left|\beta\beta\right\rangle = -\frac{1}{2}(\omega^{a}+\omega^{b})\left|T_{-}\right\rangle \tag{3.11}$$

The Zeeman interaction can be collectively described by a matrix for the four spin basis-functions as seen in (3.12). [4, 6, 7]

$$\hat{H}_{\mathrm{Z}} = \begin{array}{c} \\ \langle T_{+}| \\ \langle S| \\ \langle T_{o}| \\ \langle T_{-}| \end{array} \begin{array}{c} \begin{array}{cccc} \left|T_{+}\right\rangle & \left|S\right\rangle & \left|T_{o}\right\rangle & \left|T_{-}\right\rangle \end{array} \\ \begin{pmatrix} \frac{1}{2}(\omega^{a}+\omega^{b}) & 0 & 0 & 0 \\ 0 & 0 & \frac{1}{2}(\omega^{a}-\omega^{b}) & 0 \\ 0 & \frac{1}{2}(\omega^{a}-\omega^{b}) & 0 & 0 \\ 0 & 0 & 0 & -\frac{1}{2}(\omega^{a}+\omega^{b}) \end{pmatrix} \end{array} \tag{3.12}$$

3.3 The Hyperfine Coupling Interaction

The hyperfine coupling arises from the interaction between the unpaired electron and neighboring magnetic nuclei. The Hamiltonian, $\hat{H}_{\mathrm{HFC}}$, is written as:

$$\hat{H}_{\mathrm{HFC}} = \hat{\mathbf{S}}\cdot\mathbf{A}\cdot\hat{\mathbf{I}} \tag{3.13}$$

The terms $\hat{\mathbf{S}}$ and $\hat{\mathbf{I}}$ are the spin and nuclear vector operators, respectively, and $\mathbf{A}$ is the hyperfine coupling matrix. We assume high field approximation which reduces the $\hat{H}_{\mathrm{HFC}}$ to:

$$\begin{aligned}\hat{H}_{\mathrm{HFC}} &= \sum_i \hat{S} A^i I^i \\ &= \sum_i a^i_{eff} \hat{S}_z \hat{I}^i_z\end{aligned} \tag{3.14}$$

where

$$\mathbf{a}^i_{eff} = a_{aa}\cos^2\theta_{za} + a_{bb}\cos^2\theta_{zb} + a_{cc}\cos^2\theta_{zc} \tag{3.15}$$

and the off-diagonal terms of the hyperfine matrix are neglected when z is the field direction and a, b and c refer to the principal axes of $\mathbf{A}$. [4, 6, 7] The hyperfine coupling interaction divides the spin system up into subensembles according to different orientations of the nuclear spins. In each subensemble the hyperfine term shifts the resonance field of the electron spins as seen in Figure 3-2.

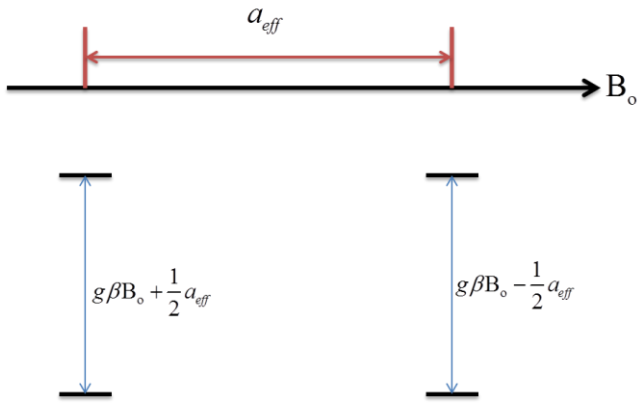

Figure 3-2: Symmetric splitting of a spin transition caused by the hyperfine interaction. The spectrum of an electron gets split into two spectral lines when an effective hyperfine coupling a_{eff} occurs to a single nucleus with nuclear spin $I = \frac{1}{2}$.

For a radical pair, the matrix form of the hyperfine coupling Hamiltonian for a given subensemble of the nuclear spin can then be written as:

$$\hat{H}_{\mathrm{HFC}} = \begin{array}{c} \\ \langle T_+| \\ \langle S| \\ \langle T_o| \\ \langle T_-| \end{array} \begin{array}{c} \begin{array}{cccc} |T_+\rangle & |S\rangle & |T_o\rangle & |T_-\rangle \end{array} \\ \begin{pmatrix} \frac{1}{2}(\mathbf{a}_{eff}^a + \mathbf{a}_{eff}^b) & 0 & 0 & 0 \\ 0 & 0 & \frac{1}{2}(\mathbf{a}_{eff}^a - \mathbf{a}_{eff}^b) & 0 \\ 0 & \frac{1}{2}(\mathbf{a}_{eff}^a - \mathbf{a}_{eff}^b) & 0 & 0 \\ 0 & 0 & 0 & -\frac{1}{2}(\mathbf{a}_{eff}^a + \mathbf{a}_{eff}^b) \end{pmatrix} \end{array} \quad (3.16)$$

where the terms $\mathbf{a}_{eff}^a$ and $\mathbf{a}_{eff}^b$ are the hyperfine coupling for electrons a and b . [4, 6, 7]

3.4 The Exchange Interaction

The exchange interaction arises from the electrostatic interaction of the two spins a and b . The Hamiltonian for the exchange interaction is:

$$\hat{H}_{\mathrm{EX}} = -J(\frac{1}{2} + 2\hat{\mathbf{S}}^a \cdot \hat{\mathbf{S}}^b) \quad (3.17)$$

where J is the exchange integral and $\hat{\mathbf{S}}^a$ and $\hat{\mathbf{S}}^b$ are the spin vector operators for the electrons a and b . The dot product of the spin operators equates to:

$$\hat{\mathbf{S}}^a \cdot \hat{\mathbf{S}}^b = \mathbf{S}_x^a \cdot \mathbf{S}_x^b + \mathbf{S}_y^a \cdot \mathbf{S}_y^b + \mathbf{S}_z^a \cdot \mathbf{S}_z^b \quad (3.18)$$

where

$$\begin{aligned}\mathbf{S}_x^a &= \frac{1}{2}(S_+^a + S_-^a)\cdot S_y^a = \frac{1}{2i}(S_+^a - S_-^a)\\ \mathbf{S}_x^b &= \frac{1}{2}(S_+^b + S_-^b)\cdot S_y^b = \frac{1}{2i}(S_+^b - S_-^b)\end{aligned} \tag{3.19}$$

Therefore

$$\hat{\mathbf{S}}^a \cdot \hat{\mathbf{S}}^b = \frac{1}{2}(S_+^a S_-^b + S_-^a S_+^b) + S_z^a S_z^b \tag{3.20}$$

The exchange interaction Hamiltonian operates on the spin basis-function $|T_o\rangle$ in the following way. [4, 6, 7]

$$\begin{aligned}\hat{H}_{\mathrm{EX}}|T_o\rangle &= \hat{H}_{\mathrm{EX}}\frac{1}{\sqrt{2}}(|\alpha\beta\rangle + |\beta\alpha\rangle)\\ &= -\frac{J}{2}(\frac{1}{\sqrt{2}}(|\alpha\beta\rangle + |\beta\alpha\rangle)) - 2JS_z^aS_z^b(\frac{1}{\sqrt{2}}(|\alpha\beta\rangle + |\beta\alpha\rangle))\\ &\quad - J(S_+^aS_-^b + S_-^aS_+^b)\frac{1}{\sqrt{2}}(|\alpha\beta\rangle + |\beta\alpha\rangle)\\ &= 0 - J(S_+^aS_-^b + S_-^aS_+^b)\frac{1}{\sqrt{2}}(|\alpha\beta\rangle + |\beta\alpha\rangle)\\ &= -\frac{J}{\sqrt{2}}[\underbrace{S_+^aS_-^b|\alpha\beta\rangle}_{0} + \underbrace{S_+^aS_-^b|\beta\alpha\rangle}_{|\alpha\beta\rangle} + \underbrace{S_-^aS_+^b|\alpha\beta\rangle}_{|\beta\alpha\rangle} + \underbrace{S_-^aS_+^b|\beta\alpha\rangle}_{0}\\ &= -\frac{J}{\sqrt{2}}(|\alpha\beta\rangle + |\beta\alpha\rangle)\\ &= -J|T_o\rangle\end{aligned} \tag{3.21}$$

Similarly

$$\begin{aligned}\hat{H}_{\mathrm{EX}}|T_+\rangle &= -J|T_+\rangle\\ \hat{H}_{\mathrm{EX}}|T_-\rangle &= -J|T_-\rangle\\ \hat{H}_{\mathrm{EX}}|S\rangle &= J|S\rangle\end{aligned} \tag{3.22}$$

The $\hat{H}_{\mathrm{EX}}$ in matrix form is:

$$\hat{H}_{\mathrm{EX}} = \begin{array}{c} \\ \langle T_+| \\ \langle S| \\ \langle T_o| \\ \langle T_-| \end{array} \begin{array}{c} \begin{array}{cccc} |T_+\rangle & |S\rangle & |T_o\rangle & |T_-\rangle \end{array} \\ \begin{pmatrix} -J & 0 & 0 & 0 \\ 0 & J & 0 & 0 \\ 0 & 0 & -J & 0 \\ 0 & 0 & 0 & -J \end{pmatrix} \end{array} \tag{3.23}$$

3.5 The Dipole-Dipole Interaction

The electron possesses spin angular momentum which generates a magnetic dipole. The dipolar coupling Hamiltonian is given by:

$$\begin{aligned} \hat{H}_{\mathrm{Dip}} &= \hat{\mathbf{S}} \cdot \mathbf{D} \cdot \hat{\mathbf{S}} \\ &= \sum_{ij} \hat{S}_i \cdot \hat{S}_j \cdot D_{ij} \end{aligned} \tag{3.24}$$

Where $\hat{\mathbf{S}}$ is the spin vector operator for the total spin and i, j refer to X, Y and Z directions in the laboratory frame. [4, 6, 7] The Hamiltonian matrix for the dipolar coupling interaction is given by:

$$\hat{H}_{\mathrm{Dip}} = \begin{array}{c} \\ \langle T_+| \\ \langle S| \\ \langle T_o| \\ \langle T_-| \end{array} \begin{array}{c} \begin{array}{cccc} |T_+\rangle & |S\rangle & |T_o\rangle & |T_-\rangle \end{array} \\ \begin{pmatrix} \frac{1}{2}D_{zz} & 0 & \sqrt{2}(D_{xz} - iD_{yz}) & \frac{1}{2}(D_{xx} - D_{yy}) - iD_{xy} \\ 0 & 0 & 0 & 0 \\ \sqrt{2}(D_{xz} + D_{yz}) & 0 & -D_{zz} & -\frac{1}{\sqrt{2}}(D_{xz} - iD_{yz}) \\ \frac{1}{2}(D_{xx} - D_{yy}) + iD_{xy} & 0 & -\frac{1}{\sqrt{2}}(\mathrm{D}_{xz} + iD_{yz}) & \frac{1}{2}D_{zz} \end{pmatrix} \end{array} \tag{3.25}$$

The sum of the spin Hamiltonians are given in the $\hat{H}_{Total}$ matrix (3.26). To get the energies and eigenvalues of our radical pair spin states the matrix must be diagonalized. [2] This can be done numerically but it is more instructive to make approximations so that the diagonalization can be done analytically.

$$\hat{H}_{Total} = \begin{array}{c} \\ \langle T_+| \\ \langle S| \\ \langle T_o| \\ \langle T_-| \end{array} \begin{array}{c} \begin{array}{cccc} |T_+\rangle & |S\rangle & |T\rangle_o & |T_-\rangle \end{array} \\ \begin{pmatrix} \bar{\omega}_o + \bar{\mathbf{a}}_{eff} + \frac{1}{2}D_{zz} - J & 0 & \sqrt{2}(D_{xz} - iD_{yz}) & \frac{1}{2}(D_{xx} - D_{yy}) - iD_{xy} \\ 0 & J & \Delta\omega + \Delta\mathbf{a}_{eff} & 0 \\ \sqrt{2}(D_{xz} + iD_{yz}) & \Delta\omega + \Delta\mathbf{a}_{eff} & -D_{zz} - J & -\frac{1}{\sqrt{2}}(D_{xz} - iD_{yz}) \\ \frac{1}{2}(D_{xx} - D_{yy}) + i\,\mathrm{D}_{\mathrm{xy}} & 0 & -\frac{1}{\sqrt{2}}(D_{xz} + iD_{yz}) & -\bar{\omega}_o + \bar{\mathbf{a}}_{eff} + \frac{1}{2}D_{zz} - J \end{pmatrix} \end{array} \quad (3.26)$$

where $\bar{\omega}_o = \frac{1}{2}\left(\omega^a + \omega^b\right)$, $\Delta\omega = \frac{1}{2}(\omega^a - \omega^b)$, $\bar{\mathbf{a}}_{eff} = \frac{1}{2}(\mathbf{a}^a_{eff} + \mathbf{a}^b_{eff})$ and $\Delta a_{eff} = \frac{1}{2}(\mathbf{a}^a_{eff} - \mathbf{a}^b_{eff})$. At high field the total Hamiltonian reduces to (3.27). Any pair of diagonal elements in the matrix are mixed by the terms of the connecting off-diagonal elements. When in the presence of the high field the tensors of the individual interactions become aligned along the principal axis or z direction and the x and y containing terms do not affectively mix. At X-band microwave frequency $\omega_o \approx 9-10$ GHz and the difference of the electron precession frequencies for organic radicals is ≈ 30 MHz. The exchange integral J will be dependent on the overlap of the electronic wavefunctions of the radical pair. As a result the following matrix is constructed. [4, 11]

$$\hat{H}_{Total} = \begin{array}{c} \\ \langle T_+| \\ \langle S| \\ \langle T_o| \\ \\ \langle T_-| \end{array} \begin{array}{c} \begin{array}{cccc} |T_+\rangle & |S\rangle & |T\rangle_o & |T_-\rangle \end{array} \\ \begin{pmatrix} \bar{\omega}_o + \bar{\mathbf{a}}_{eff} + \frac{1}{2}D_{zz} - J & 0 & 0 & 0 \\ 0 & J & \Delta\omega + \Delta\mathbf{a}_{eff} & 0 \\ 0 & \Delta\omega + \Delta\mathbf{a}_{eff} & -D_{zz} - J & 0 \\ 0 & 0 & 0 & -\bar{\omega}_o + \bar{\mathbf{a}}_{eff} + \frac{1}{2}D_{zz} - J \end{pmatrix} \end{array} \tag{3.27}$$

The reduced $\hat{H}_{Total}$ matrix is diagonalized to give the four eigenstates:

$$E_1 = \bar{\omega}_o + \bar{\mathbf{a}}_{eff} - J + \frac{1}{2}D_{zz} \tag{3.28}$$

$$E_2 = -\frac{1}{2}D_{zz} + K \tag{3.29}$$

$$E_3 = -\frac{1}{2}D_{zz} - K \tag{3.30}$$

$$E_4 = -\bar{\omega}_o + \bar{\mathbf{a}}_{eff} - J + \frac{1}{2}D_{zz} \tag{3.31}$$

where

$$K = (J + \frac{1}{2}D_{zz})^2 + (\Delta\omega + \Delta\mathbf{a}_{eff})^2 \tag{3.32}$$

and the radical pair spin eigenfunctions are

$$\Psi_1 = |T_+\rangle \tag{3.33}$$

$$\Psi_2 = \cos\theta|S\rangle + \sin\theta|T_o\rangle \tag{3.34}$$

$$\Psi_3 = -\sin\theta|S\rangle + \cos\theta|T_o\rangle \tag{3.35}$$

$$\Psi_4 = |T_-\rangle \tag{3.36}$$

As an aside,

$$\begin{aligned} \sin 2\theta &= (\Delta\omega + \Delta\mathbf{a}_{eff}) / K \\ \cos 2\theta &= (J + \frac{1}{2} D_{zz}) / K \end{aligned} \tag{3.37}$$

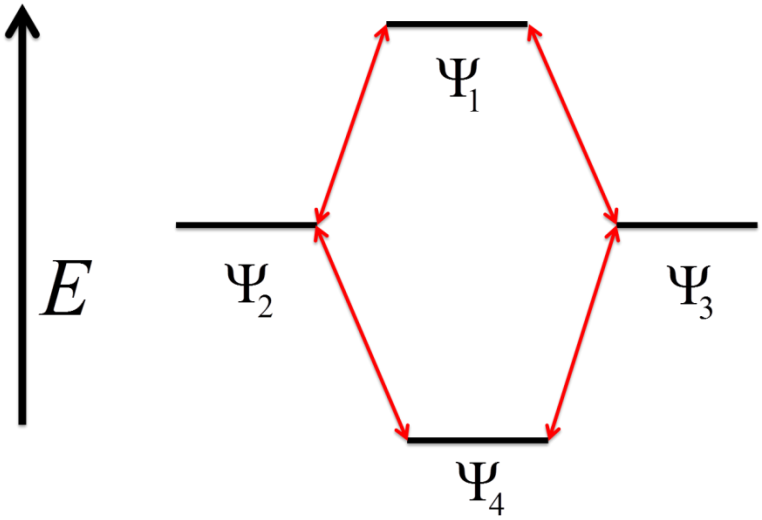

Figure 3-3: The radical pair eigenstates for the spin eigenfunctions of (3.33)-(3.36) are plotted on an energetic scale with allowed transitions labeled in red.

The transition energies associated with the spin allowed transitions are:

$$E_{12} = \bar{\omega}_o + \bar{\mathbf{a}}_{eff} - J + D_{zz} - K \tag{3.38}$$

$$E_{13} = \bar{\omega}_o + \bar{\mathbf{a}}_{eff} - J + D_{zz} + K \tag{3.39}$$

$$E_{24} = \bar{\omega}_o + \bar{\mathbf{a}}_{eff} + J - D_{zz} + K \tag{3.40}$$

$$E_{34} = \bar{\omega}_o + \bar{\mathbf{a}}_{eff} + J - D_{zz} - K \tag{3.41}$$

The spectrum of the radical pair will have four lines whose intensity is related to the probability of the transition. [4, 11] There are two applied magnetic fields in an EPR experiment. The large static field $\mathbf{B_o}$ and the applied field $\mathbf{B_1}$. The $\mathbf{B_1}$ field is applied

along the x-direction perpendicular to the static $\mathbf{B_o}$ field. The affective spin vector operator S_X is written as:

$$\mathbf{S}_X = (S_+ + iS_-) \tag{3.42}$$

Therefore for a given transition from an initial state, i , to a final state, f , the probability becomes:

$$P_{if} = \left|\left\langle \Psi_f \left| S_+ + iS_- \right| \Psi_i \right\rangle\right|^2 \tag{3.43}$$

For the $|S\rangle$ and $|T_o\rangle$ states being operated on by the creation and annihilation spin operators S_+ and S_- result in:

$$\begin{aligned} S_+|S\rangle &= 0 \\ S_-|S\rangle &= 0 \\ S_+|T_o\rangle &= \sqrt{1(1+1)-0(0+1)}\,|T_+\rangle = \sqrt{2}\,|T_+\rangle \\ S_-|T_o\rangle &= \sqrt{1(1+1)-0(0+1)}\,|T_-\rangle = \sqrt{2}\,|T_-\rangle \end{aligned} \tag{3.44}$$

So the probability of the Ψ_2 to Ψ_1 transition is given by:

$$\begin{aligned} P_{12} &= \left|\left\langle \Psi_1 \left| S_+ + iS_- \right| \Psi_2 \right\rangle\right|^2 \\ &= \left|\left\langle \Psi_1 \right| (S_+ + iS_-)(\cos\theta|S\rangle + \sin\theta|T_o\rangle) \left| \Psi_2 \right\rangle\right|^2 \\ &= \left|\left\langle T_+ | T_+ \right\rangle \sqrt{2}\sin\theta\right|^2 + \left|\left\langle T_+ | T_- \right\rangle i\sqrt{2}\sin\theta\right|^2 \\ &= 2\sin^2\theta \end{aligned} \tag{3.45}$$

Similarly,

$$\begin{aligned} P_{24} &= 2\sin^2\theta \\ P_{13} &= 2\cos^2\theta \\ P_{34} &= 2\cos^2\theta \end{aligned} \tag{3.46}$$

For the weakly coupled spins $(\Delta\omega + \Delta\mathbf{a}_{eff}) \gg (J + \frac{1}{2}D_{zz})$ and therefore the maximum mixing occurs for the Ψ_2 and Ψ_4 eigenstates. The stick spectrum of the allowed transitions can be seen in Figure 3-4. Initially, the Ψ_2 and Ψ_4 eigenstates are populated according to the $|S\rangle$ character of the radical pair. When the radical pair has more of the $|T_o\rangle$ character the transitions of Figure 3-3 occur. Thus, the populations of Ψ_2 and Ψ_4 unequal and are proportional to $\cos^2\theta$ and $\sin^2\theta$ respectively which is from the square of the singlet character of the eigenfunction. The intensity of the transitions is proportional to the product of the probability of the transition and the population differences of the eigenstates as seen by equation (3.47) and (3.48). [4, 11]

$$\begin{aligned} P_{21} &\propto \sin^2\theta \qquad \Delta n_{21} \propto \cos^2\theta \\ P_{31} &\propto \cos^2\theta \qquad \Delta n_{31} \propto \sin^2\theta \\ P_{24} &\propto \sin^2\theta \qquad \Delta n_{24} \propto \cos^2\theta \\ P_{34} &\propto \cos^2\theta \qquad \Delta n_{34} \propto \sin^2\theta \end{aligned} \tag{3.47}$$

$$I_{ij} \propto P_{ij}\Delta n_{ij} = \cos^2\theta\sin^2\theta \tag{3.48}$$

This results in a spectrum of four equal intensity lines with two emissive and two absorptive lines (Figure 3-4). The g-factors of the a and b radicals will be separated according to their difference in precession frequencies. The effect of the dipolar coupling and exchange interaction lead to the distribution of the electron transitions from α to β

and β to α. When the line-broadening and the sum over all orientations are taken into account the radical spectrum will look much different than the stick spectrum.

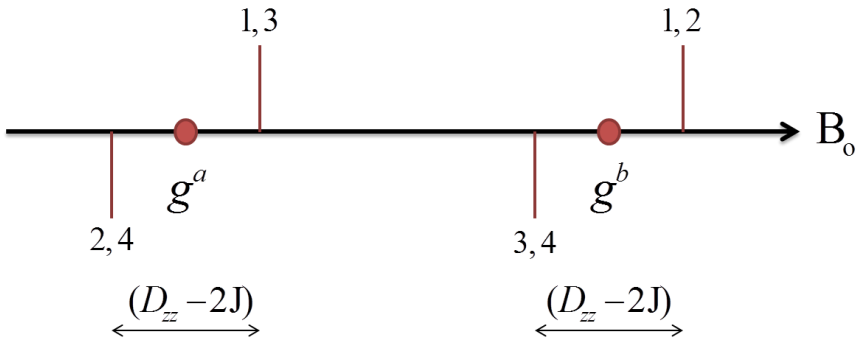

Figure 3-4: The stick spectrum of a weakly coupled radical pair of spins a and b.

The actual radical pair spectrum of the $P_{700}^{+}A_1^{-}$ for *Synechocystis* sp. PCC 6803 can be seen in Figure 3-5.

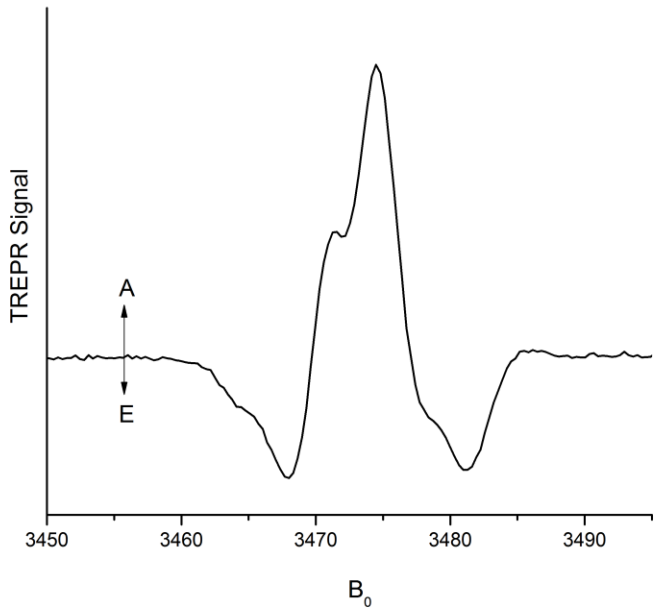

Figure 3-5: The X-Band TREPR spectrum of the radical pair $P_{700}^{+}A_1^{-}$ of *Synechocystis* sp. PCC 6803.

The sequential electron transfer of $P_{700}^{+}A_1^{-}$ to $P_{700}^{+}F_X^{-}$ is seen in the transient EPR spectrum. While the lifetimes of the precursors to the radical $P_{700}^{+}A_1^{-}$ are not sufficiently long enough to influence the polarization characteristics of the spectrum, the sequential transfer to $P_{700}^{+}F_X^{-}$ does. The population of the eigenstates and intensities of the transitions will therefore be an effect of the lifetime of the $P_{700}^{+}A_1^{-}$ radical pair. The result is a net polarization of the P_{700}^{+} radical which appears as a purely emissive signal at late time. The contributions of the F_X^{-} are not seen due to the fast spin relaxation of the Fe within the [4Fe4S] cluster. Thus, the spectrum of the sequential radical pair $P_{700}^{+}F_X^{-}$ is a net emmisive signal and can be seen in Figure 3-6 (red line).

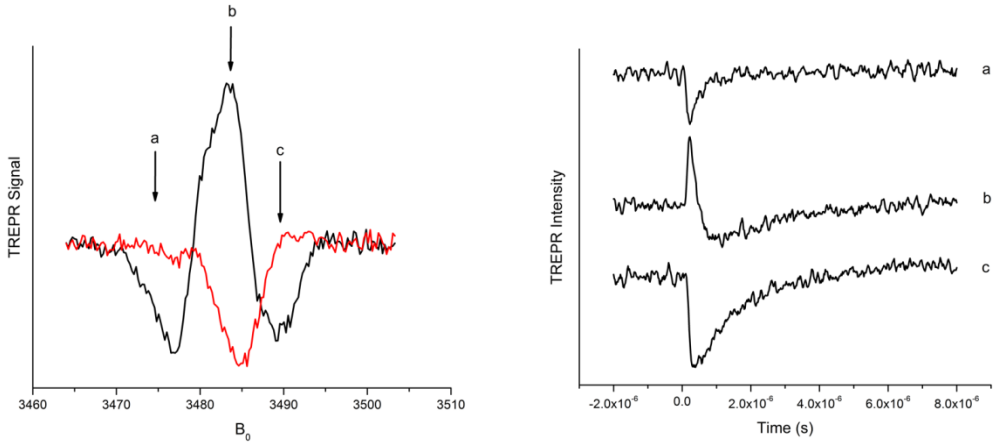

Figure 3-6: (left) Room temperature transient EPR (TREPR) spectra of the spin polarized radical pair $P_{700}^{+}A_1^{-}$ (black) at early time after the laser flash to net emission of $P_{700}^{+}F_X^{-}$ (red) for wild type cyanobacterium *Synechocystis* sp. PCC 6803. The black spectrum is a spin polarized pattern of emission/absorption/emission moving into the net emission of the red spectrum. (right) The individual transients at field positions indicated a, b and c on the radical pair spectra(left). The signal intensity changes with the ET of A_1^{-} to F_X and can be fit with a multi-exponential decay curve with an amplitude and rate.

3.6 EPR Detection Methods

3.6.1 Field Modulated Lock-in Detection

Static radicals are detected by a method called Field Modulated Lock-in Detection. The EPR experiment is carried out as mentioned above. A secondary smaller oscillating magnetic field is applied to the sample. Its purpose is to modulate the sample signal to a frequency that can be locked in. The signal reaching the detector contains fast noise that can be filtered because it contains a wide spectrum of frequencies whereas the signal oscillates with the field modulation frequency which is commonly set to 100 kHz. The response time of the lock-in detection is about 5-10 times the inverse of the modulation frequency. Thus, the response time with a modulation frequency of 100 kHz is 50-100 us. For static signals, this is not an issue, but our PSI electron transfer contains lifetimes that significantly shorter than this and therefore a different technique called direct detection is used for time resolved EPR experiments. [4]

3.6.2 Direct Detection

The direct detection method does not use a secondary oscillating magnetic field. Instead, the signal from the resonator is connected directly to an oscilloscope. The microwave bridge needs a modified preamplifier to eliminate any high frequency filtering that might limit signal getting to the detector. What is lost in signal to noise is made up for in sensitivity. The signals generated in PSI electron transfer are massive and dwarf much of the high frequency noise. Signals in the range of 100ns to a few milliseconds can now be detected. [4]

3.7 References

1. Griffiths, D.J., *Introduction to Electrodynamics*1999: Prentice Hall.
2. Griffiths, D.J., *Introduction to quantum mechanics*. 2nd ed2005, Upper Saddle River, NJ: Pearson Prentice Hall. ix, 468 p.
3. Gerlach, W. and O. Stern, *The experimental evidence of direction quantistion in the magnetic field.* Z Phys, 1922. **9**: p. 349-352.
4. van der Est, A., *Transient EPR: using spin polarization in sequential radical pairs to study electron transfer in photosynthesis.* Photosynth Res, 2009. **102**(2-3): p. 335-347.
5. Zech, S.G., W. Lubitz, and R. Bittl, *Pulsed EPR experiments on radical pairs in photosynthesis: Comparison of the donor-acceptor distances in photosystem I and bacterial reaction centers.* Ber Bunsen Phys Chem, 1996. **100**(12): p. 2041-2044.
6. Kandrashkin, Y.E., W. Vollmann, D. Stehlik, K. Salikhov, and A. Van der Est, *The magnetic field dependence of the electron spin polarization in consecutive spin correlated radical pairs in type I photosynthetic reaction centres.* Mol Phys, 2002. **100**(9): p. 1431-1443.
7. Kandrashkin, Y.E., K.M. Salikhov, A. van der Est, and D. Stehlik, *Electron spin polarization in consecutive spin-correlated radical pairs: Application to short-lived and long-lived precursors in type 1 photosynthetic reaction centres.* Appl. Magn. Reson., 1998. **15**(3-4): p. 417-447.
8. Buckley, C.D., D.A. Hunter, P.J. Hore, and K.A. McLauchlan, *Electron Spin Resonance of Spin-Correlated Radical Pairs.* Chem. Phys. Lett., 1987. **135**(3): p. 307-312.
9. Atherton, N.M., *Bruker Lecture - the Nuclear Zeeman Interaction in Electron Resonance.* Chem Soc Rev, 1993. **22**(5): p. 293-298.
10. Atherton, N.M. and A.G. Davies, *Special Issue on Electron-Paramagnetic-Resonance Spectroscopy.* Chem Soc Rev, 1993. **22**(5): p. U293-U293.
11. Kandrashkin, Y.E. and A. van der Est, *Time-resolved EPR spectroscopy of photosynthetic reaction centers: From theory to experiment.* Appl. Magn. Reson., 2007. **31**(1-2): p. 105-122.
12. Bittl, R. and S.G. Zech, *Pulsed EPR Study of Spin-Coupled Radical Pairs in Photosynthetic Reaction Centers: Measurement of the Distance Between and in Photosystem I and between and in Bacterial Reaction Centers.* J Phy Chem B, 1997. **101**(8): p. 1429-1436.

Chapter 4 Methods for introducing foreign quinones into PSI

4.1 Isolation and purification of PSI

Spectroscopic studies and chemical manipulation of PS I require that the protein be isolated. The details of the procedures used to grow the cyanobacterium *Synechocystis* sp. PCC 6803 and isolate PS I including media and buffer recipes are given in Appendix I. The organisms are grown photoautotrophically by providing light, CO_2 and supportive media to carryout photosynthesis. In the case of the *menB* variant, antibiotics were used to insure survivability of the mutant and avoid nutrient competition by contamination. The removal of PSI containing thylakoids from the cyanobacteria is done by shearing forces of a French press. The isolated thylakoids are solubilized and separated by a detergent rich size exclusion sucrose density gradient to separate PSI from other proteins contained in the thylakoids.

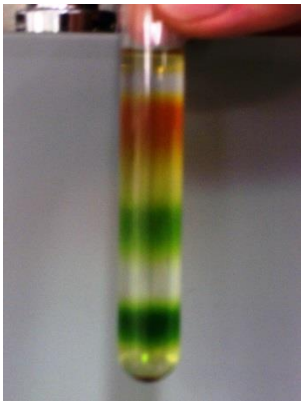

Figure 4-1: Initial sucrose gradient of solubilized thylakoid membranes separated by size with the carotenoid band (top), PSII, PSI monomer and free chlorophyll (middle) and PSI trimer band (bottom).

A second gradient was done to pellet PSI trimers. The purity of the PSI increased and it allowed a simple collection of a condensed pellet. The pellet was re-suspending in appropriate buffer and then frozen until needed for incubation with 100 fold excess of foreign quinone. The incubation reaction was done with thawed PSI trimers on ice with desired naphthoquinone. The reaction was washed to remove quinone unbound and reconcentrated to 10 uM PSI concentration. The concentration of PSI was monitored with peak height of the Chl-*a* UV-Vis absorbance signal at 667 nm.

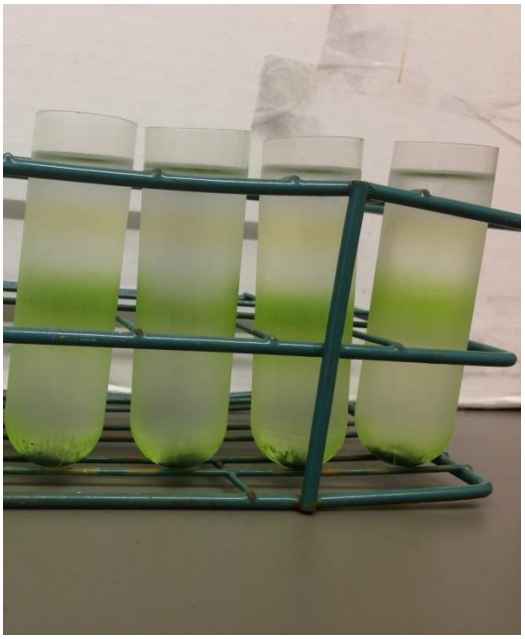

Figure 4-2: Second sucrose gradient containing no detergent. PSI trimer complexes are pelleted during the 16 hour spin at 28,000 rpm. Faint carotenoid and (PSII, PSI monomer and free chlorophyll) bands can also be seen.

4.2 Solvent Extraction of PSI Quinones

Early quinone exchange studies of PSI involved extraction of the native quinone followed by incorporation of foreign quinones. [1-3] The quinone is bound by a single hydrogen bond to the protein backbone and this binding can be disrupted and the quinone extracted with organic solvents. [1] One extraction technique developed by Biggins et.al.

[2] involves treating freeze dried PSI particles with dry hexane containing a trace of methanol. Itoh and co-workers were also able to achieve quinone extraction using di-ethylether [3]. The extraction can be monitored by TREPR to ensure the solvents are not damaging the ability of the PSI complex to carry out natural ET. If the extraction procedure removes the quinone but does not interfere with the initial charge separation, the triplet state of P_{700} is formed due to recombination of $P_{700}^{+}A_0^{-}$. This triplet state has a characteristic spin polarization pattern that can be easily recognized (Figure 4-3). The spectrum shown in Figure 4-3 is from a PSI sample isolated from *Chlamydomonas reinhartii* in which partial loss of Phylloquinone has occurred. The broad features of the spectrum are due to $^{3}P_{700}$ and the narrow peaks at the centre arise from PSI complexes that still contain phylloquione. The arrows indicate the characteristic polarization pattern A/E that is only seen when the triplet is formed by charge recombination of a radical pair precursor.

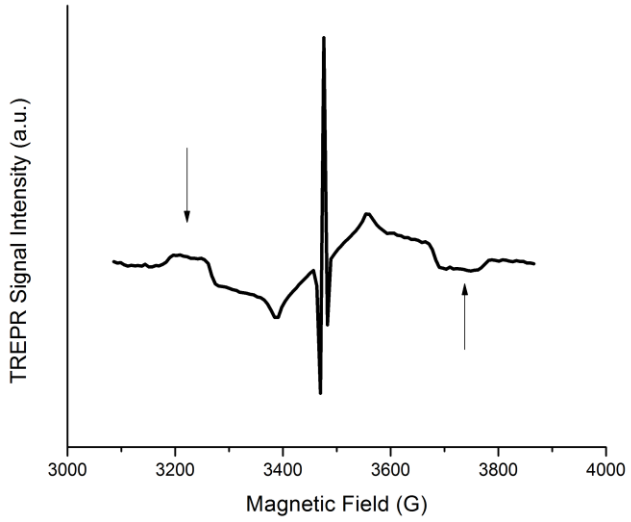

Figure 4-3: X-Band transient EPR of triplet spin polarization from radical pair recombination to the $^3P_{700}$ state in the algae *Chlamydomonas reinhartii*. Arrows indicate the characteristic A/E polarization pattern of this recombination mechanism.

Reincorporation of quinones can be achieved by re-suspension of the extracted PSI particles and incubation with an excess of quinone, which allows diffusion into the open binding site. This method is successful but also extracts many of the carotenoid and antenna chlorophyll-*a* cofactors and it undoubtedly leads to some denaturation of the protein. Genetic mutations provide an alternative to harsh solvents.

4.3 *menB* mutant

As part of a study of the biosynthetic pathway for Phylloquinone, several genes corresponding to enzymes suspected to be involved in the pathway were targeted for interruption in the cyanbacterium *Synechocystis* sp. PCC 6803. One of the genes targeted was *menB*, which codes for the 1,4-dihydroxy-2-naphthoate synthase enzyme needed for proper construction of phylloquinone. The interruption of *menB* gene expression was done by insertion of an antibiotic resistance gene sequence into the *menB* gene sequence by homologous recombination. In the resulting mutant strain of the bacterium, the synthesis of phylloquinone is no longer carried out and the authors expected that the A_1 binding site would go unfilled. However, the benzoquinone, plastoquinone-9 (Figure 4-4), which is present in the thylakoid membrane, is able to bind loosely into the A_1 binding site. [4] This quinone is synthesized in the organism readily for the ETC. This substitution ensures that ET through PSI is maintained and thus the viability of the organism, but the strain must be grown under low light conditions. [4]

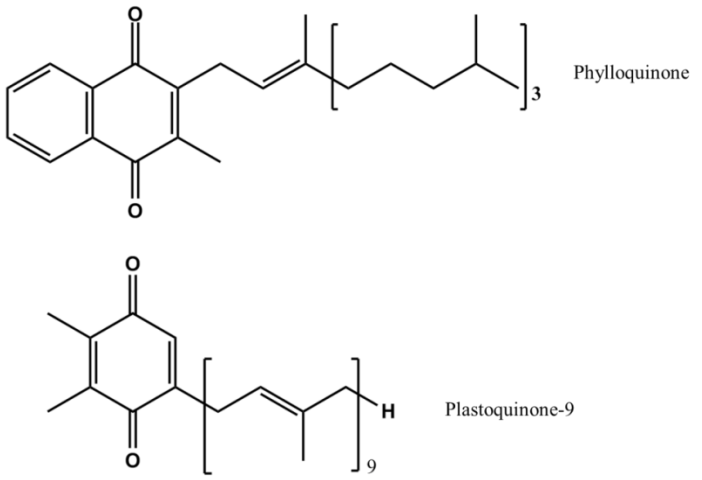

Figure 4-4: The wild-type naphthoquinone Phylloquinone (top) and the menB variant benzoquinone Plastoquinone-9 (bottom) which occupy the A_1 binding site.

When purified *menB* PSI particles are incubated with non-native napthoquinones, the loosely bound plastoquinone-9 is readily displaced. This procedure was carried out for several naphthoquinones and the low-temperature X-band TREPR radical pair spectrum was recorded for each.

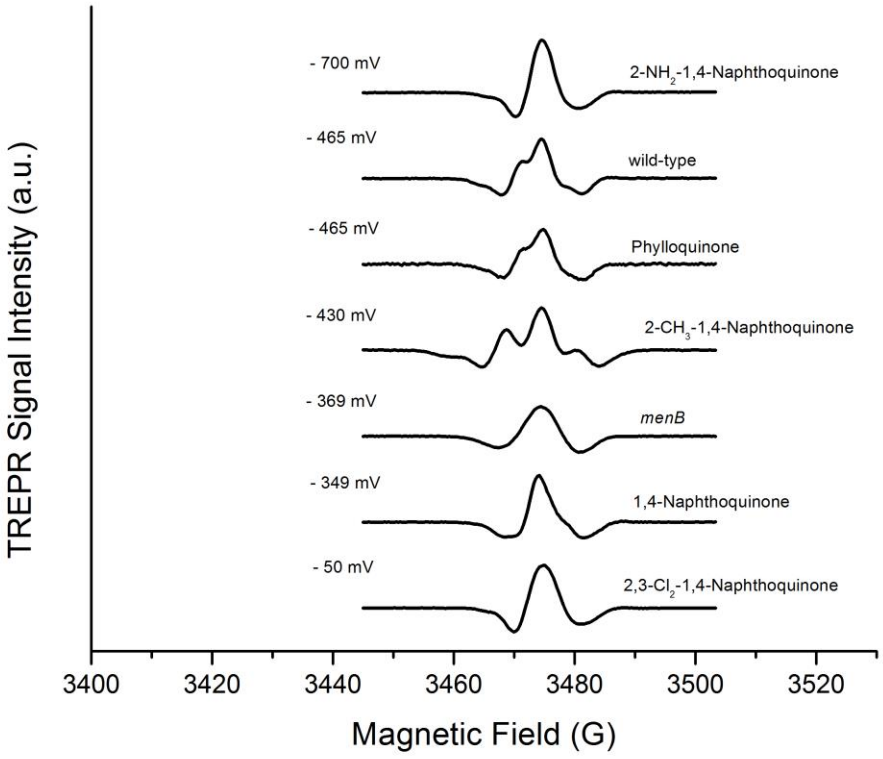

Figure 4-5: X-Band TREPR spectra of the spin polarized $P_{700}^{+}A_1^{-}$ radical pair at 80 K for wild-type, *menB* and *menB* incubated with indicated quinone. Reduction midpoint potentials measured in DMF against a Ag/AgCl reference electrode. Values for the midpoint potential have been corrected against the standard hydrogen electrode (SHE) for clarity.

The TREPR spectra of the $P_{700}^{+}A_1^{-}$ radical pairs for the *menB* incubations are plotted in Figure 4-5. There are significant spectral changes when compared to the *menB* and wild-type samples. The origin of the changes comes is the different hyperfine coupling of the electron to the surrounding nuclei of the incorporated quinones. A full description of the EPR spectral features are discussed in Chapter 3 of this thesis. The substituents and positioning of those substituents controls the midpoint potential of the naphthoquinone. [5-7] These midpoint potentials can vary over a wide range (~1 V). The potential of 2,3-dichloro-1,4-naphthoquinone is very positive measuring -50.0 mV vs SHE. In Chapter 6,

this sample was used to investigate the directionality of ET in PSI as a function of temperature.

4.4 References

1. Sieckman, I., A. van der Est, H. Bottin, P. Sétif, and D. Stehlik, *Nanosecond electron transfer kinetics in photosystem I following substitution of quinones for vitamin K1 as studied by time resolved EPR.* FEBS Lett., 1991. **284**(1): p. 98-102.
2. Biggins, J. and P. Mathis, *Functional Role of Vitamin K_1 in Photosystem I of the Cyanobacterium Synechocystis 6803.* Biochem, 1988. **27**(5): p. 1494-1500.
3. Kumazaki, S., M. Iwaki, I. Ikegami, H. Kandori, K. Yoshihara, and S. Itoh, *Rates of Primary Electron-Transfer Reactions in the Photosystem-I Reaction-Center Reconstituted with Different Quinones as the Secondary Acceptor.* J. Phys. Chem., 1994. **98**(43): p. 11220-11225.
4. Johnson, T.W., G. Shen, B. Zybailov, D. Kolling, R. Reategui, S. Beauparlant, I.R. Vassiliev, D.A. Bryant, A.D. Jones, J.H. Golbeck, and P.R. Chitnis, *Recruitment of a foreign quinone into the A_1 site of photosystem I. I. Genetic and physiological characterization of phylloquinone biosynthetic pathway mutants in Synechocystis sp. pcc 6803.* J Biol Chem, 2000. **275**(12): p. 8523-30.
5. Pletcher, D. and H. Thompson, *A microelectrode study of the influence of electrolyte on the reduction of quinones in aprotic solvents.* J Chem Soc Farad T, 1998. **94**(23): p. 3445-3450.
6. Prince, R.C., P.L. Dutton, and J.M. Bruce, *Electrochemistry of Ubiquinones - Menaquinones and Plastoquinones in Aprotic-Solvents.* FEBS Lett., 1983. **160**(1-2): p. 273-276.
7. Prince, R.C., P. Lloyd-Williams, J. Malcolm Bruce, and P. Leslie Dutton, *[8] Voltammetric measurements of quinones*, in *Methods in Enzymology*, B.F. Sidney Fleischer, Editor 1986, Academic Press. p. 109-119.

 The collective work was done by the authors listed below. The X-Band and Q-Band CW and Transient EPR were done by SM and AVE of Brock University. The molecular dynamics simulations were done by HG and AC of Brock University. The *Chlamydomonas rheinhardtii* wild-type PSI and PsaA-L722T PSI mutant were produced and purified by MM and KR of Arizona State University. The ONIOM calculations were done by NZ and GH of Georgia State University.

Chapter 5 Introduction of a Hydrogen Bond between Phylloquinone A_{1A} and a Threonine Side-chain OH Group in Photosystem I

Sam Mula[1], Michael D. McConnell[2], Amy Ching[1], Nan Zhao[3], Heather L. Gordon[1], Gary Hastings[3], Kevin E. Redding[2] and Art van der Est[1*].*

[1]Department of Chemistry, Brock University, St Catharines, Ontario, Canada
[2]Department of Chemistry and Biochemistry, Arizona State University, Tempe, Arizona, USA
[3]Department of Physics and Astronomy, Georgia State University, Atlanta, Georgia, USA

*Corresponding authors: AvdE: avde@brocku.ca, K.E.R.: Kevin.Redding@asu.edu

5.1 Introduction

In oxygenic photosynthesis, Photosystem I (PS I), uses light to transfer electrons from plastocyanin on the lumenal side of the thylakoid membrane to ferredoxin on the stromal

side.[1] The electron transport chain consists of two branches of cofactors that diverge at the chlorophyll *a*/*a*′ dimer, P_{700} on the donor side and converge again at F_X, the first of three [4Fe-4S] iron-sulfur clusters on the acceptor side. The two branches are labeled A and B according to which protein subunit, PsaA or PsaB, provides the majority of the bonds to the cofactors[2] and each of them contains two chlorophyll-*a* molecules A_{-1} and A_0 and a phylloquinone, A_1. There is some variability in the side chain of the phylloquinones between species but the headgroup is the same. The acceptor side of the complex is strongly reducing and the two phylloquinone acceptor molecules have unusually low midpoint potentials in the vicinity of -800 mV,[3] which is ~350 mV more negative than in aprotic solvent.[4] Although it is clear that the phylloquinone binding pocket plays an important role in shifting the quinone potentials to more negative values, many details of how this occurs are uncertain. More importantly, the relationship between the structure of the binding pocket, the midpoint potential of the quinone and the rate of electron transfer (ET) is not well understood. As can be seen in the X-ray structure[5] of the A_{1A} phylloquinone binding site (Figure 5-1), one of the two carbonyl oxygen atoms of the quinone headgroup is hydrogen bonded to the backbone nitrogen of PsaA-L722.[5, 6]

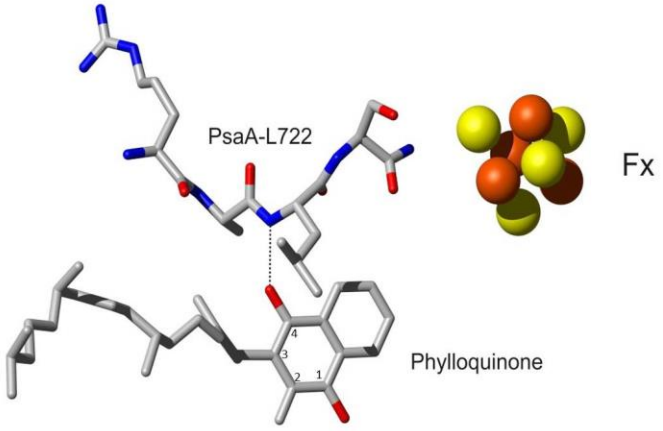

Figure 5-1 The A-branch phylloquinone binding site in PS I from the 2.5 Å x-ray crystal structure (PDB code: 1JB0).[5, 7] The figure was constructed using the program MOLMOL.[8]

The role of this H-bond has been investigated recently [9-11] using point mutations to selectively alter residue PsaA-722 or the corresponding B-branch residue PsaB-706. It was shown that replacement of PsaA-L722 with a bulky tryptophan led to changes in the spin density distribution on the semi-quinone headgroup consistent with weakening or loss of the H-bond.[10] Such a change would be expected to destabilize the semiquinone and consistent with this expectation the rate of ET from A_{1A} to F_X increased in the PsaA-L722W mutant.[9] It was proposed that the larger size of the tryptophan side chain compared to that of leucine likely forces a rearrangement of the protein such that the backbone N of reside PsaA-722 moves away from the phylloquinone and breaks or weakens the H-bond. Tyrosine and threonine mutants of residue PsaA-722 have also been constructed and were used as part of a study to investigate interquinone ET.[12] Both the PsaA-L722Y and PsaA-L722T mutants showed shorter lifetimes for A_{1A} to F_X ET but the effect of the mutations on the phylloquinone H-bonding was not investigated. In the case

of the PsaA-L722Y mutant, the faster ET is expected because the tyrosine side chain is also considerably larger than that of leucine, hence the steric bulk suggested to cause breaking of the H-bond in the PsaA-L722W mutant should cause similar effects. However, the faster ET observed for the PsaA-L722T mutant is not as easy to rationalize because the side chain of threonine is smaller than that of leucine and hence breaking of the H-bond due to steric constraints seems unlikely. Moreover threonine is polar and might be expected to cause some stabilization of the charge on the semi-quinone, which would slow forward ET.

Here, we use transient EPR spectroscopy, quantum chemical calculation and molecular dynamics simulations to investigate what effects the incorporated threonine residue has on hydrogen bonding between A_{1A} and its binding site and on the ET kinetics. The results strongly suggest that in the PsaA-L722T mutant, A_{1A} is H-bonded to the OH group of the threonine side chain. The change in the H-bonding is expected to cause a shift of the quinone midpoint potential to a more positive value and should decrease the rate of forward ET. However, the observed rate of ET is faster than in the wild type. We argue that this is probably the result of a change in the electronic coupling between A_{1A} and F_X.

5.2 Materials and Methods

5.2.1 Construction and Growth of the PsaA-L722T Mutant Strain.

The PsaA-L722T mutation was created as described previously.[12, 13] Briefly, a one-tube PCR method for site-directed mutagenesis was performed[14] using plasmids containing the *psaA-3* exon and the *aadA,* antibiotic resistance gene. Mutant plasmids were delieved via biolistic bombardment into a *psaA-3*Δ strain (KCR1001-11A) of *Chlamydomonas reinhardtii*. Cells were grown under continuous low-light (10 μE $m^{-2}s^{-1}$)

at room temperature on standard TAP media and were selected for resistance to spectinomycin and streptomycin.

5.2.2 Isolation of Photosystem I from the PsaA-L722T Mutant Strain.

Cells were harvested and broken in a chilled French press at 3000 psi. Thylakoid membranes were solubilized on ice in darkness with 0.9 % (wt/vol) n-dodecyl-β-D-maltoside at 0.8 – 1.0 $mg \cdot mL^{-1}$ Chl for 20 minutes and the solubilized fraction was then isolated from the insoluble debris by ultracentrifugation at 65000 g for 25 min. Solubilized membrane proteins were laid on sucrose density gradients, which were formed by the freeze-thaw, method and contained 5 mM Tricine-NaOH (pH 8.0), 0.3 M sucrose, 0.3 M betaine, and 0.05% n-dodecyl-β-D-maltoside. Following a 20-hr centrifugation at 120,000 × *g*, the lowest green band was collected and concentrated in buffer containing 5 mM Tricine-NaOH (pH 8.0), 5 mM $CaCl_2$, 5 mM $MgCl_2$ and 0.05% n-dodecyl-β-D-maltoside.[15]

5.2.3 Transient EPR Spectroscopy.

Time/field transient EPR datasets were measured using a modified Bruker ER 200D-SRC spectrometer with either an ER 041 X-MR X-band or an ER 051 QR Q-band microwave bridge. For the X-band datasets, a Flexline ER 4118 X-MD-5W1 dielectric resonator was used at temperatures below 270 K and an ER 4103 TM rectangular resonator was employed at room temperature. An ER 5106 QT-W cylindrical resonator was used for the Q-band experiments. Light excitation was achieved using a Continuum Surelite Nd-YAG laser operating at 10 Hz and a wavelength of 532 nm and 4.0 mJ/pulse. The temperature was controlled using an Oxford Instruments CF935 gas flow cryostat. The transient EPR signal was collected in direct detection mode with a home-built broadband amplifier (bandwidth > 500 MHz) and was digitized using a LeCroy LT322

500 MHz digital oscilloscope and saved on a PC for analysis. Samples were pretreated with 1 mM sodium ascorbate and 50 μM phenazine methosulfate (PMS). For the low temperature experiments, the samples were dark adapted for 20 minutes on ice and frozen in the dark to ensure complete reduction of P_{700}^{+} before illumination.

5.2.4 Pulsed EPR Experiments.

Out-of-phase echo modulation curves were collected at 80 K using a Bruker Elexsys E580 spectrometer. The echo was generated using a $\pi/2$-τ-π pulse sequence with 8 ns and 16 ns pulses, respectively. The echo intensity was integrated over a 48 ns window centered at the echo maximum. The delay between laser flash and initial microwave pulse was 400 ns. A Continuum Surelite Nd-YAG laser operating at 532 nm, 10 Hz and 3.4 mJ/pulse was used to excite the sample.

5.2.5 Molecular Dynamics Modelling.

Conformations of the protein sidechains and cofactors were explored by restrained high-temperature molecular dynamics simulations for both wild type PS I and the PsaA-L722T mutant. Initial atomic coordinates for the wild type were taken from the 2.5 Å resolution crystal structure of PS I (PDB code: 1JB0).[5] All protein subunits, co-factors, lipids and water molecules in the crystal structure were included in the model. Initial coordinates for the PsaA-L722T mutant were generated by virtual mutation of the residue PsaA-L722 to Thr using the Swiss-Pdb Viewer. [16] For both the wild type and the PsaA-L722T mutant, the AMBER program LEaP [17] was used to generate missing coordinates, including the positions of hydrogen atoms. Twenty sodium ions were added along the periphery of PS I to maintain electroneutrality. The NAMD scalable molecular dynamics package [18] using the all-atom AMBER-1994 force field [17, 19] was used for all modelling of PS I interactions. AMBER parameters for chlorophyll, phylloquinone

and beta-carotene cofactors were as derived from the *ab initio* force field developed by Ceccarelli et al.[20] and modified by Vasil'ev and Bruce[21]. The iron-sulfur clusters were considered to be in the oxidized state and their partial charges were determined from density functional theory calculations on $[Fe_4S_4(SCH_3)_4]^{2-}$.[22] Ideal bond lengths, angles, and dihedral angles for the iron-sulfur clusters were assumed to be those observed in the crystal structure.

A timestep of 1 fs was used during molecular dynamics simulations. Van der Waals interactions were smoothly reduced to zero, using the standard X-PLOR switching function, between 10 Å and the cutoff radius of 13.0 Å. NAMD's multiple timestepping scheme for full-electrostatic integration was employed, whereby the electrostatic interactions beyond the 13.0 Å cutoff were re-evaluated only every 4 timesteps. The radius of the non-bonded neighbor list was set to 13.5 Å and neighbor lists were updated every 20 timesteps. Covalent bonds to hydrogens were constrained using the SHAKE algorithm.[23]

The following protocol was used for molecular dynamics simulations of both wild type and PsaA-L722T PS I. The initial conformation was relieved of possible strain via conjugate gradient (CG) energy minimization for 2000 steps. The system was then heated to 300K by reassigning the velocities of each atom and increasing the temperature by 0.001 K every time step over a total of 300 ps; no atom constraints were applied during this preliminary heating phase. Next, the system was heated from 300K to 500 K over 200 ps, by velocity reassignment, during which only the cofactors, protein side chains and the protein backbone between PsaA-N709 and PsaA-I724 were allowed to move. The positions of all other backbone atoms, solvent atoms, and Na^+ ions were held fixed.

During a subsequent 200 ps equilibration period at 500 K, molecular conformations were saved every 100 timesteps. This high temperature simulation was performed to enable the unrestrained components of the model to overcome energetic barriers and thus sample conformational space more broadly. Finally, every fifth conformation along the 2000 conformer trajectory at 500 K was selected for analysis; each was subjected to CG energy minimization until the root-mean-square gradient of the potential energy was < 0.08 kcal/(mol Å). The positional constraints on backbone and solvent atoms and Na^+ ions were retained during the energy minimization. This procedure resulted in a total of 100 quenched (energy minimized) conformations for each form of PS I.

To assess possible artifacts introduced by the molecular mechanics forcefield and simulation protocol, the structures obtained from the simulation of wild type PSI were compared to the X-ray structure. The initial heating phase of the molecular dynamics simulation to 300K caused a slight expansion of the protein backbone, but the root-mean-squared differences between the backbone (N, Cα, C, O) conformation of the X-ray structure and the models of the wild type and PsaA-L722T are both 0.8 Å over all 12 protein subunits and 0.7 Å over PsaA only. The H-bond between O4 of phylloquinone A and the backbone nitrogen of PsaA-L722 increases slightly in length from 2.69 Å in the X-ray structure to an average of 2.92 Å in the simulation, while the angle between the quinone C=O bond and the H-bond is unchanged at 159º.

5.2.6 Quantum Chemical Calculations

The spin density distribution on the phylloquinone headgroup in the PsaA-L722T mutant was calculated using ONIOM type[24] QM:MM calculations. (ONIOM is an acronym for: our **O**wn **N**-layered **I**ntegrated molecular **O**rbital + **M**olecular mechanics package. QM = quantum mechanical, MM = molecular mechanics) Structural models

used in the ONIOM calculations were constructed starting from the model of Canfield et al.[25], who used density functional theory (DFT) to refine the original PSI X-ray structure. Swiss-Pdb viewer[16] was used to change residue PsaA-722 from leucine to threonine. Two-layer ONIOM calculations ONIOM(B3LYP/6-31G+(d):Amber) were performed using Gaussian03[26]. The QM layer contained the head group and the first 4 carbon atoms of the phytyl tail of phylloquinone in the PsaA binding site. The remaining atoms of the protein residues formed the MM layer. Linking between the QM and MM layers was achieved using hydrogen link atoms. For the MM part of the calculation, the all-atom AMBER-1994 force field was used for the protein. For the cofactors an *ab initio* force field developed for the cofactors of bacterial photosynthetic reaction centers, which was parameterized to reproduce density functional theory vibrational modes, was used. All atoms of the cofactors, solvent and protein side chains, as well as the atoms of the protein backbone between PsaA-I717and PsaA-L736, were unconstrained during optimization.

5.3 Results and Discussion

5.3.1 Transient EPR Spectra.

Figure 5-2 shows room temperature transient EPR (TREPR) spectra and transients for wild type and the PsaA-L722T mutant. The arrows under the spectra indicate the magnetic field positions at which the transients were taken. At room temperature, the transient EPR spectra of both samples evolve from an E/A/E (E=Emission, A= Absoption) pattern due to $P_{700}^{+}A_{1A}^{-}$ at early time to a predominantly emissive spectrum from $P_{700}^{+}F_{X}^{-}$ at later time. The spectra shown in Figure 5-2 have been extracted from the full dataset by the kinetic fitting procedure as described elsewhere.[27] Representative

transients are displayed in the bottom of Figure 5-2 to show the quality of the fit. ET in the B-branch of PS I is too fast to be resolved kinetically by TREPR, however it is observed as a fraction of the emissive signal present at early time. The size of this fraction can be determined approximately by fitting the data.[2] The fits yield lifetimes of 260 ± 30 ns and 200 ± 30 ns for forward ET from A_{1A} to F_X and amplitude ratios of 35:65 and 45:55 for the fast:slow phases of ET in the wild type and PsaA-L722T mutant, respectively. These values are consistent with the corresponding lifetimes of 256 ± 12 ns and 171 ± 10 ns and amplitude ratios of 37:63 and 49:51 obtained previously by optical methods.[12]

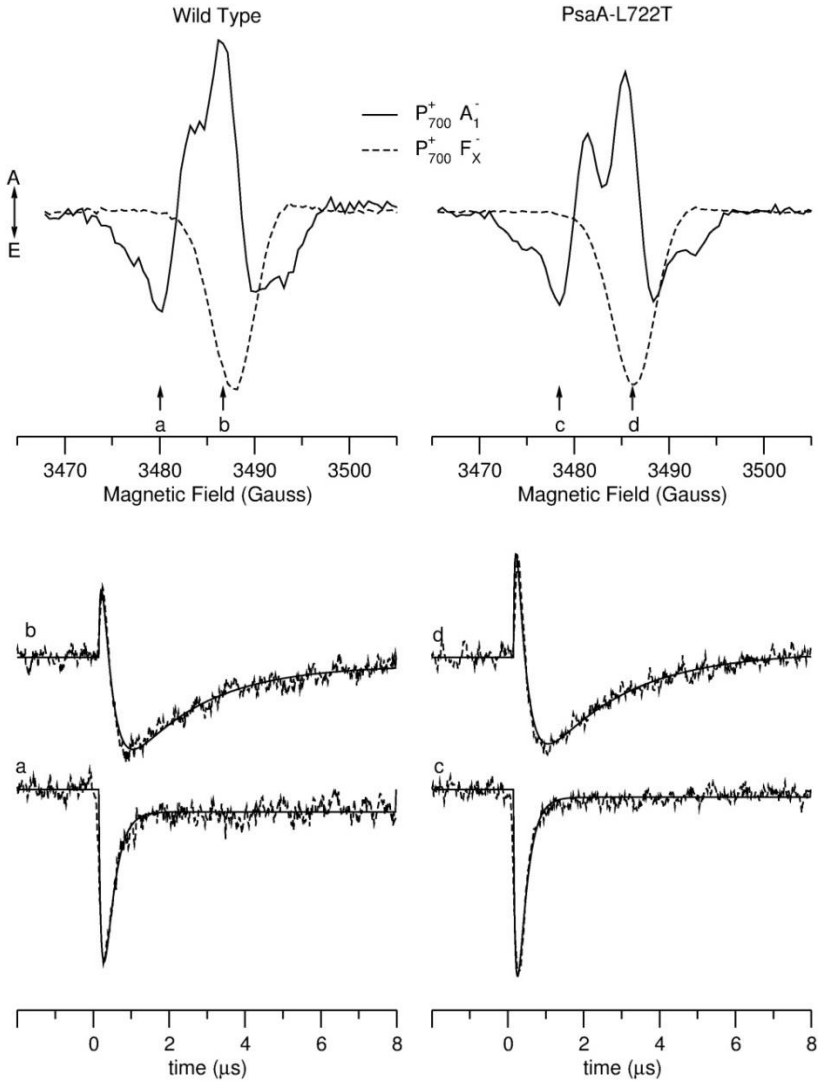

Figure 5-2: Room temperature transient EPR spectra and transients of PS I from the wild type and PsaA-L722T mutant strains of *Chlamydomonas rheinhardtii*. The spectra of $P_{700}^{+}A_{1A}^{-}$ and $P_{700}^{+}F_{X}^{-}$ have been extracted from the full datasets by kinetic fitting. The transients in the lower part of the figure yield lifetimes of 260 ± 30 ns and 200 ± 30 ns for $P_{700}^{+}A_{1A}^{-}$ in the wild type and Psa-L722T mutant, respectively.

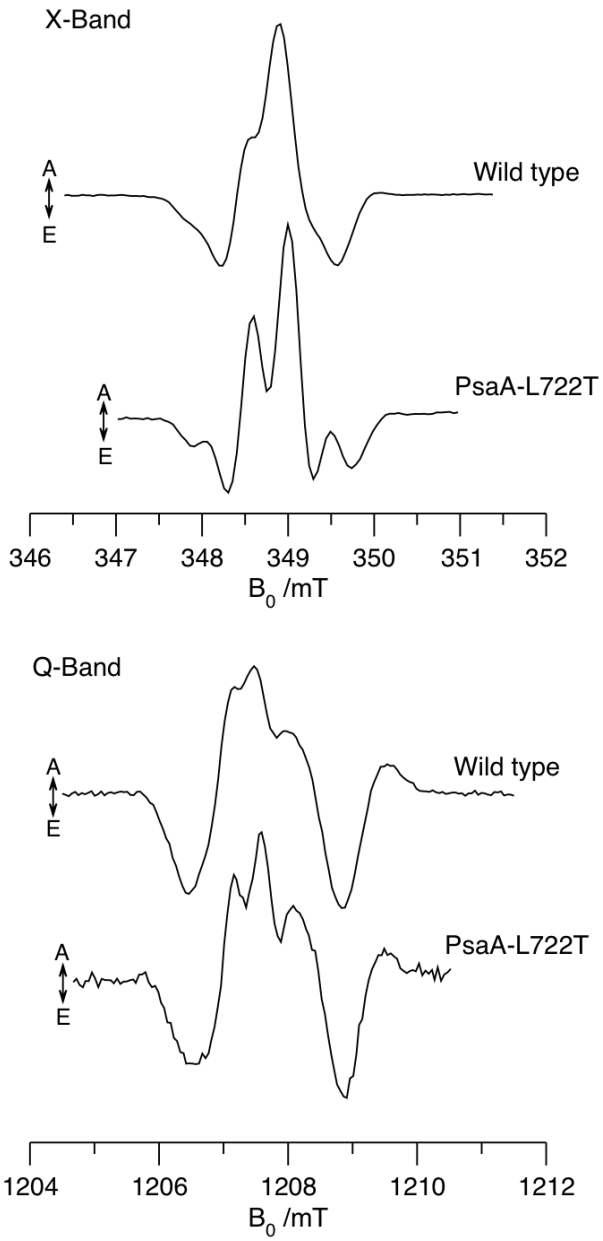

Figure 5-3: X- and Q-band TREPR spectra taken at 80K. The spectra are the average signal intensity in a 400 ns wide time window centered at 850 ns after the laser flash.

In Figure 5-2, the spectra of $P_{700}^{+}A_{1A}^{-}$ in the wild type and the PsaA-L722T mutant are noticeably different with a clear splitting of the central absorptive peak visible in spectrum of the PsaA-L722T mutant while the wild type shows only a shoulder. These differences are seen more clearly in the X- and Q-band spectra measured at 80K, which are shown in Figure 5-3. At X-band (Figure 5-3, top), the spectrum of the PsaA-L722T

mutant shows clear splitting of the downfield emission, the central absorption and the upfield emission. At Q-band (Figure 5-3, bottom), the central absorption of the wild type has two shoulders that are known to arise from strong methyl hyperfine coupling on the *y*-component of the quinone g-tensor. In the corresponding spectrum of the PsaA-L722T mutant, these features are more pronounced. In contrast, the upfield region of the Q-band spectra, which arises primarily from transitions associated with P_{700}^{+}, is virtually identical in the wild type and the mutant. Thus, the change from Leu to Thr at residue PsaA-722 appears to cause an increase in the methyl hyperfine coupling of A_{1A}^{-}. In the wild type, the methyl hyperfine coupling is known to be large because the asymmetry in the H-bonding. The single H-bond to the backbone N of PsaA-L722 distorts the spin density distribution in an alternating pattern around the quinone ring such that it is increased on the ring carbon adjacent to the methyl group. [28-30] The increased hyperfine coupling in the PsaA-L722T mutant implies that the spin density adjacent to the methyl group is further increased as a result of the mutation, which suggests even greater asymmetry in the H-bonding. It also suggests that midpoint potential of A_{1A} is probably more positive in the PsaA-L722T mutant than the wild type since stronger H-bonding should stabilize the semiquinone. Such a change in midpoint potential should slow forward ET, which is opposite to the observed increase in the rate of forward ET in the PsaA-L722T mutant. However, the ET rate is also determined by the electronic coupling and by the reorganization energy.

5.3.2 Out-of-phase Echo Modulation.

It is possible that the electronic coupling between A_{1A} and F_X is altered in the PsaA-L722T mutant as a result of a change in the position of the quinone. This possibility can be explored using out-of-phase electron spin echo modulation measurements. The

modulation curves depend strongly on the spin-spin coupling in the radical pair $P_{700}^{+}A_{1A}^{-}$ and hence on the distance between P_{700} and A_{1A}. If the position of the quinone is altered in the mutant a change in the frequency in the echo modulation curve is expected. Experimental echo modulation curves for the wild type and PsaA-L722T mutant are compared in Figure 5-4. The dashed curves in the figure are calculated as described in references [31-33] using the exchange and dipolar coupling constants determined previously.[34, 35] As can be seen in Figure 5-4, the echo modulation curve from the PsaA-L722T mutant is essentially identical to that from the wild type and is reproduced well using the known coupling constants. Hence, we can conclude that the coupling and the distance between P_{700} and A_{1A} is not altered in the PsaA-L722T mutant, which implies that the position of A_{1A} does not change significantly.

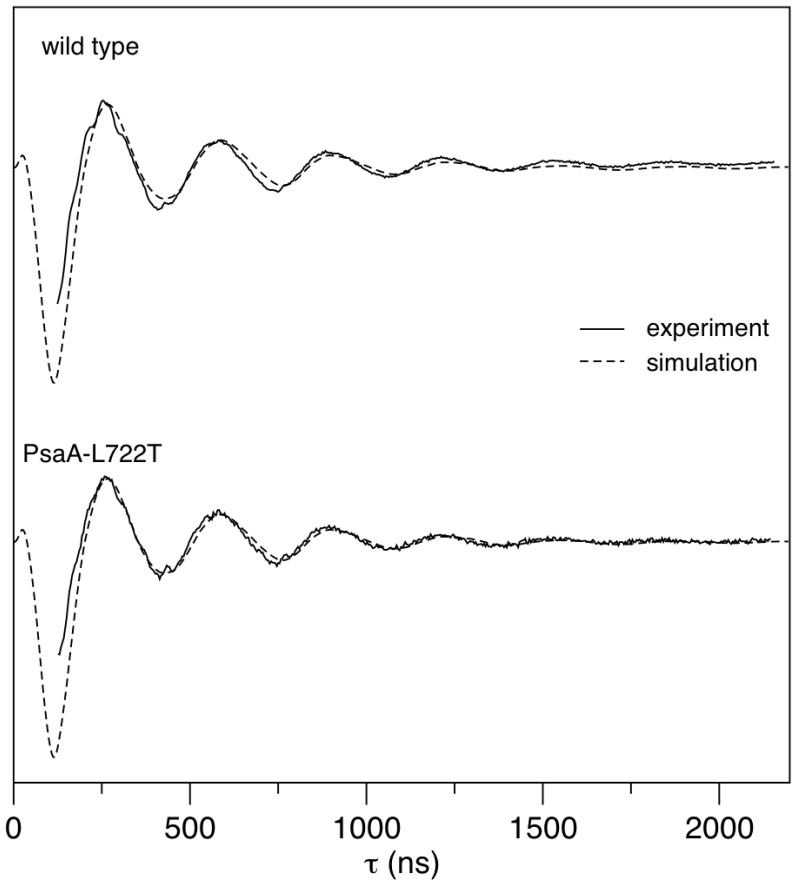

Figure 5-4: X-band out-of-phase electron spin echo envelope modulation curves of PS I from the wild type and PsaA-L722T mutant at 80 K. The dashed curves are calculated by integrating equation (1) of reference[31] over a random distribution of molecular orientations. The dipolar and exchange coupling constants in the simulation were set to *D* = –170 µT and *J* = 1 µT as determined previously.[34, 36]

However, the observed change in the ET lifetime, 260 ns for the wild type versus 200 ns for the PsaA-L722T mutant, is not large and so we need to consider whether the change in the distance between A_{1A} and F_X needed to account for it would lead to a measurable change in the echo modulation curves. Dutton's ruler[37] predicts that a decrease of 0.2 Å in the edge-to-edge distance between A_{1A} to F_X would account for the observed change in rate if all other factors remained the same. If A_{1A} were to move 0.2 Å closer to F_X along the vector joining the center of the A_{1A} headgroup and the center of F_X, the resulting change in the distance between P_{700} and A_{1A} is only 0.03 Å. This is about a

factor of 5-10 smaller than could be detectable in the echo modulation curves. Thus, we cannot discount the possibility that a change in the electronic coupling between F_X and A_{1A} resulting from a small change in the distance between them could contribute to the change in ET rate.

5.3.3 Molecular Dynamics Simulations

To investigate the structural changes in the phylloquinone binding pocket that cause the altered spin density distribution we have performed molecular dynamics simulations of the mutant. The simulations probe the conformation space of each structure and yield families of conformers that represent local minima on the energy surface. Our primary interest is in the nature of the hydrogen bonding of the quinone. Figure 5-5 shows histograms of the distance between oxygen O_4 of A_{1A} and possible H-bond donors. The top histogram is for the wild type and shows the distance to the backbone N of PsaA-L722. The structure expands slightly during the initial heating phase of simulation and as a result, the O-N distance for the wild type is ~0.2 Å longer than observed in the crystal structure. As expected, a very narrow distribution of possible distances is found for the wild type and the average C-O-N angle of 160º in the simulation is identical to the value in the X-ray structure. The middle histogram is the corresponding distance in the PsaA-L722T mutant. In contrast to the wild type, a broad distribution of O-N possible distances is found for the PsaA-L722T mutant (Figure 5-5, middle) and the entire distribution is shifted to considerably longer distances. Thus, the simulations show that when a wide conformation space is sampled by heating the system to 500 K, many conformers are found in which the H-bond between the oxygen O_4 of phylloquinone A and the backbone nitrogen mutation is broken or weakened. This implies that there may be greater flexibility of the backbone.

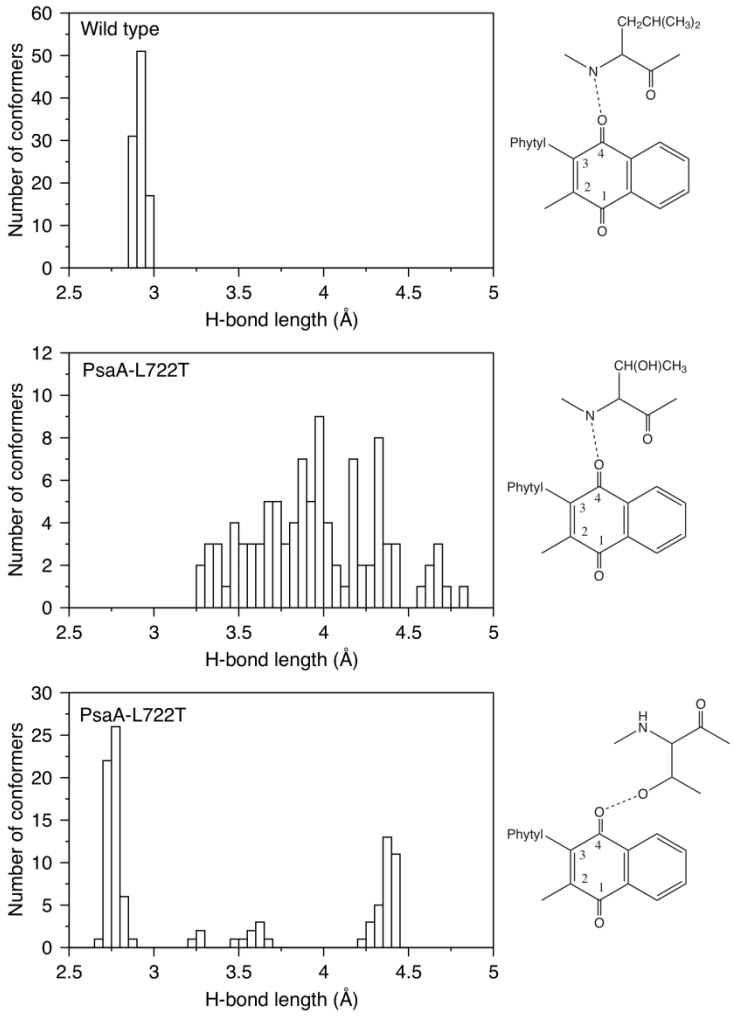

Figure 5-5: Histograms of possible H-bond distances from molecular dynamics simulations of PS I.

The finding that the H-bond to the backbone N may be disrupted in the PsaA-L722T mutant suggests that if the increased hyperfine splitting is due to stronger H-bonding, there should be an additional H-bond donor available to bind to O_4. The obvious candidate is the OH group of the Thr side chain. In the bottom panel of Figure 5-5, the distribution of distances between oxygen O_4 of the phylloquinone and oxygen $O_{\gamma 1}$ of the Thr side chain oxygen is shown. As can be seen, the largest group of conformers is clustered around a distance of 2.8 Å, which is slightly shorter than the O-N distance obtained for the wild type. In addition however, there are two smaller groups of

conformers in which the O-O distances are ~4.4 Å and ~3.5 Å. Examples of the structures of the conformers with O-O distances of 2.8 and 4.4 Å are shown in Figure 5-6 A and B, respectively.

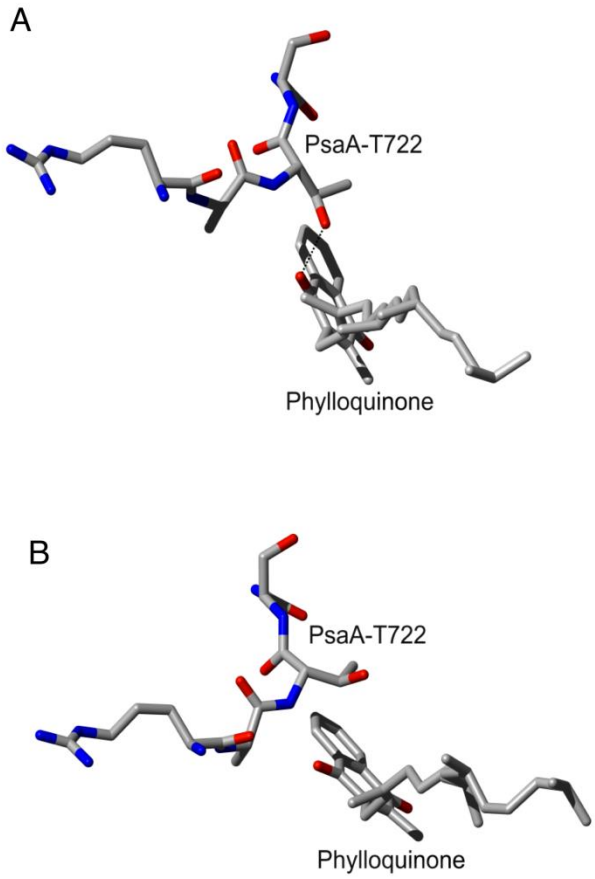

Figure 5-6: Representative conformers from the molecular dynamics simulation of the PsaA-L722T mutant. A: conformer with a phylloquinone O_4 to Thr $O_{\gamma 1}$ O-O distance of 2.8 Å. B: conformer with an O-O distance of 4.4 Å.

Comparison of the two structures in Figure 5-6 shows that they correspond to two different rotomeric conformers of the threonine sidechain about C_α- C_β. In the conformer shown in Figure 5-6A (conformer 1), the side chain of PsaA-T722 is rotated such that C-O bond of the OH group is directed toward the carbonyl group of the quinone. In the conformer in Figure 5-6B (conformer 3), the longer O-O distance of 4.8 Å arises from a rotation of the Thr side chain so that the C-O bond is directed away from the quinone.

The intermediate O-O distances occur in the third rotomeric conformation of the sidechain, which we refer to as conformer 2. From Figure 5-5 and Figure 5-6, it is clear that the simulation predicts that a large number of low energy conformers exist in which the OH group of the Thr side chain is within H-bonding distance of oxygen O_4 of phylloquinone.

An important factor for the effect of the H-bond on the properties of the quinone is its direction with respect to the lone pairs on the carbonyl oxygen. In the X-ray structure of cyanobacterial PS I,[5] the C-O-N angle associated with the H-bond between phylloquinone A_{1A} and the backbone of PsaA-L722 is 169º and the O-N direction is approximately 20º out of the quinone plane. For a linear H-bond along the long pair direction these two angles would be 120º and 0º, respectively. However, a survey of a large number of organic crystals[38] shows that although H-bonding along the lone pair direction is somewhat preferred, a wide range of geometries occur in nature and the H-bond arrangement found for A_{1A} in PS I is near the median of this distribution. A very different arrangement is found for the putative H-bond between the OH group of the Thr sidechain and phylloquinone A in the PsaA-L722T mutant. For those conformers in which the O_4 - $O_{\gamma 1}$ distance is less than 3 Å, the simulation gives an average C_4-O_4- $O_{\gamma 1}$ angle of 134º and an average angle between the O_4- $O_{\gamma 1}$ direction and the plane of the quinone carbonyl group of 65º. Because this geometry is very different from that of the H-bond in the wild type its effect on the spin density distribution is not immediately apparent and quantum mechanical calculations are necessary.

5.3.4 QM/MM Calculations.

The influence of the threonine side chain on the spin density distribution of phyllosemiquinone can be calculated using ONIOM type QM:MM methods. For phyllosemiquinone in the PsaA-L722T mutant three separate calculations were performed, starting with the threonine side-chain in each of the three possible conformations that are outlined in Figure 5-5C, with Oγ - - O bond distances of ~2.75, 3.6 and 4.4 Å for conformers 1, 2 and 3, respectively.

The three models (for phyllosemiquinone in the PsaA-L722T mutant) were geometry optimized using the ONIOM(B3LYP/6-31G+(d):AMBER) approach, and Table 1 lists calculated interatomic distances and angles between the A-branch phyllosemiquinone oxygen atoms and their surroundings. For comparison, Table 5-1 also lists ONIOM calculated geometry optimized data for phyllosemiquinone in WT PS I, as well as the corresponding distances and angles derived from the DFT refined structure model of Canfield et al.[25] for neutral phylloquinone in WT PS I.

Table 5-1: Interatomic distances and angles involving the oxygen atoms of phyllosemiquinone in WT and the PsaA-L722T mutant obtained from ONIOM calculations. Distances in Å and angles in degrees.

	Wild Type		PsaA-L722T		
			Conformer		
	DFT model[25]	ONIOM	1	2	3
	neutral	anion	anion	anion	anion
Thr $O_{\gamma 1}$-O_4			2.76	3.76	4.30
Thr H_{γ}-O_4			1.80	2.90	5.12
C_1=O	1.241	1.261	1.259	1.259	1.261
C_4=O	1.253	1.288	1.295	1.290	1.288
N-O_4	2.98	2.82	2.80	2.84	2.80
NH-O_4	1.95	1.82	1.79	1.84	1.81
∠N-H-O_4	170.7	164.7	171.1	165.8	162.8

The distance between the hydrogen atom of the Thr hydroxyl side chain and the oxygen atom of the C_4=O group of phyllosemiquinone (Thr H_{γ}–O_4 distance) for conformer 1 is

1.80 Å. Such a distance is typical for an H-bond. In conformer 2 and 3 the Thr H_γ–O_4 distance is 2.90 and 5.12 Å, both of these are well outside H-bonding distance.

In the x-ray structure and the ONIOM calculated models, the phylloquinone carbonyl bond-lengths reflect the asymmetric H-bonding environment, and the C_4=O bond (which is H-bonded) is longer than the C_1=O bond (which is not H-bonded). For neutral phylloquinone in WT PS I the C_1=O and C_4=O bond lengths are 1.241 and 1.253 Å, respectively. For phyllosemiquinone in WT PS I ONIOM calculations indicate C_1=O and C_4=O bond lengths of 1.261 and 1.288 Å, respectively. As expected, phylloquinone reduction leads to a lengthening of both carbonyl bonds. The difference in their bond lengths also increases compared to the neutral state (0.027 versus 0.008 Å). For phyllosemiquinone in the PsaA-L722T mutant, the C_4=O bond is lengthened to 1.295 Å in conformer 1 (1.288 Å in WT), possibly indicating stronger/additional H-bonding to the Thr hydroxyl group.

The ONIOM models indicate that the distance between the backbone nitrogen of residue PsaA722 and the C_4=O oxygen atom of phyllosemiquinone is roughly the same in the wild type and the PsaA-L722T mutant. This result differs for that found with the MD simulations (Figure 5-5B) because of the different approaches taken for the two types of calculations. In the MD simulations, the system is heated to 500 K to ensure that as wide a range of conformers as possible are sampled. However, in the ONIOM calculations, PsaA722 the temperature is kept at 300 K and a narrower range of backbone conformations is sampled.

Table 5-2: Principal values and orientation of the 2-methyl hyperfine coupling tensor of phylloquinone *A* in PS I. The coupling constants are given in MHz and the angles are in degrees.

	Wild Type			PsaA-L722T		
	Experiment [39][a]	DFT[39]	ONIOM model	Conformer 1	Conformer 2	Conformer 3
A_{xx}	8.8 (9.1)	9.62	9.0	10.4	10.6	9.0
A_{yy}	12.4 (12.7)	13.05	13.0	15.0	13.3	13.2
A_{zz}	8.3 (8.6)	8.86	9.2	10.6	10.8	8.9
a_{iso}	9.8 (10.1)	10.51	10.4	12.0	11.6	10.4
θ[b]	0	1	13	–2.2	2.2	6
ϕ[b]	30	14	17	15	17	15

[a]The experimental coupling constants are taken from the literature[39] and were measured for the state $P_{700}^{+}A_{1A}^{-}$ in PS I from *T. elongatus*. The values in parentheses are for the photoaccumulated phyllosemiquinone in the same samples. [b]A clockwise rotation about the *y*-axis by θ followed by a clockwise rotation by ϕ about the *z*-axis transforms the principal axes of the hyperfine tensor into those of the g-tensor.

Table 5-2 shows the methyl hyperfine coupling tensors of phyllosemiquinone calculated for the wild type and the three conformers of the PsaA-L722T mutant. Experimental and calculated values for the wild type are from Niklas et al. [39]. The ONIOM model of the wild type reproduces the DFT values very well, apart from a slightly different orientation of the tensor axes. For conformer 1 of the PsaA-L722T mutant both the isotropic hyperfine coupling and the anisotropy of the tensor increase as a result of the additional H-bond. In conformer 2, the coupling and anisotropy are also increased compared to the wild type, but less so than conformer 1. The coupling and anisotropy for conformer 3 is essentially the same as for wild type. To examine the effect of these changes in the methyl hyperfine coupling, the spin polarized EPR spectra of $P_{700}^{+}A_{1A}^{-}$ have been calculated using the known parameters[40] for native PS I in *T.*

elongatus and replacing the wild type hyperfine coupling tensor with those calculated for the PsaA-L722T mutant (Table 5-2). As can be seen, the hyperfine coupling tensor computed for conformer 1 reproduces the experimental spectrum very well. Thus, the observed splitting is consistent with the formation of an H-bond between the Thr side chain and oxygen O_4 of phylloquinone A_{1A} and retention of the H-bond to the backbone nitrogen.

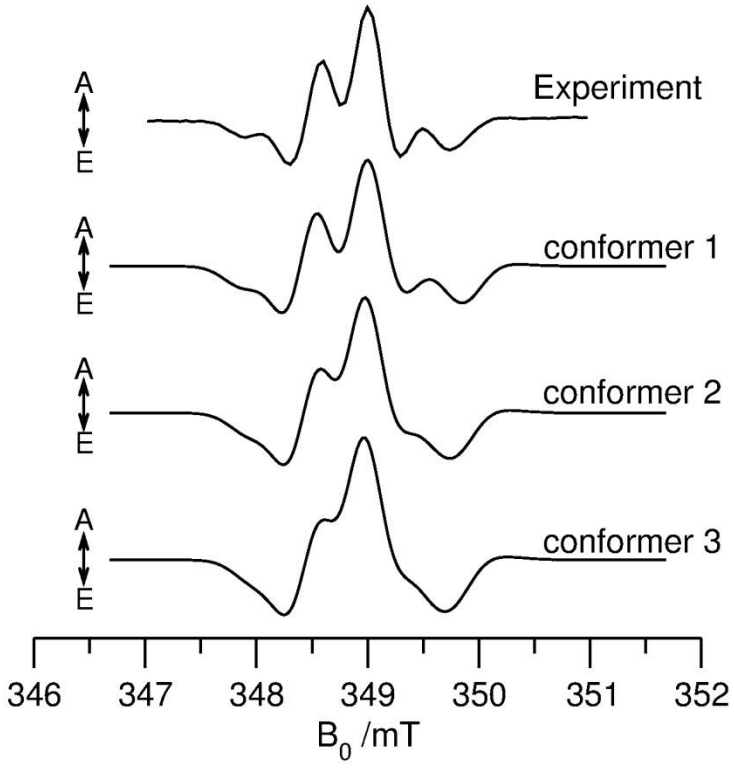

Figure 5-7: X-band TREPR spectra of $P_{700}^{+}A_{1A}^{-}$ in the PsaA-L722T mutant. In the calculated spectra the known parameters[40] for the wild type have been used with the methyl hyperfine coupling tensor given by the ONIOM QM/MM calculations shown in Table 2.

5.3.5 Electron Transfer Energetics.

The faster rate of ET at room temperature for the PsaA-L722T mutant implies that the activation energy for A-branch ET is lowered as a result of the mutation. On the other hand, the H-bonding to the Thr side chain is expected to stabilize the charge on the semiquinone, which would lead to an increase in the activation energy, if the

reorganization energy remains the same. The mutation might also be expected to influence the electronic coupling and the frequency of the modes coupled to the ET. To investigate these effects we have measured the temperature dependence of the rate of A-branch ET in the PsaA-L722T mutant. The rates were obtained from TREPR traces as described for the room temperature data above.

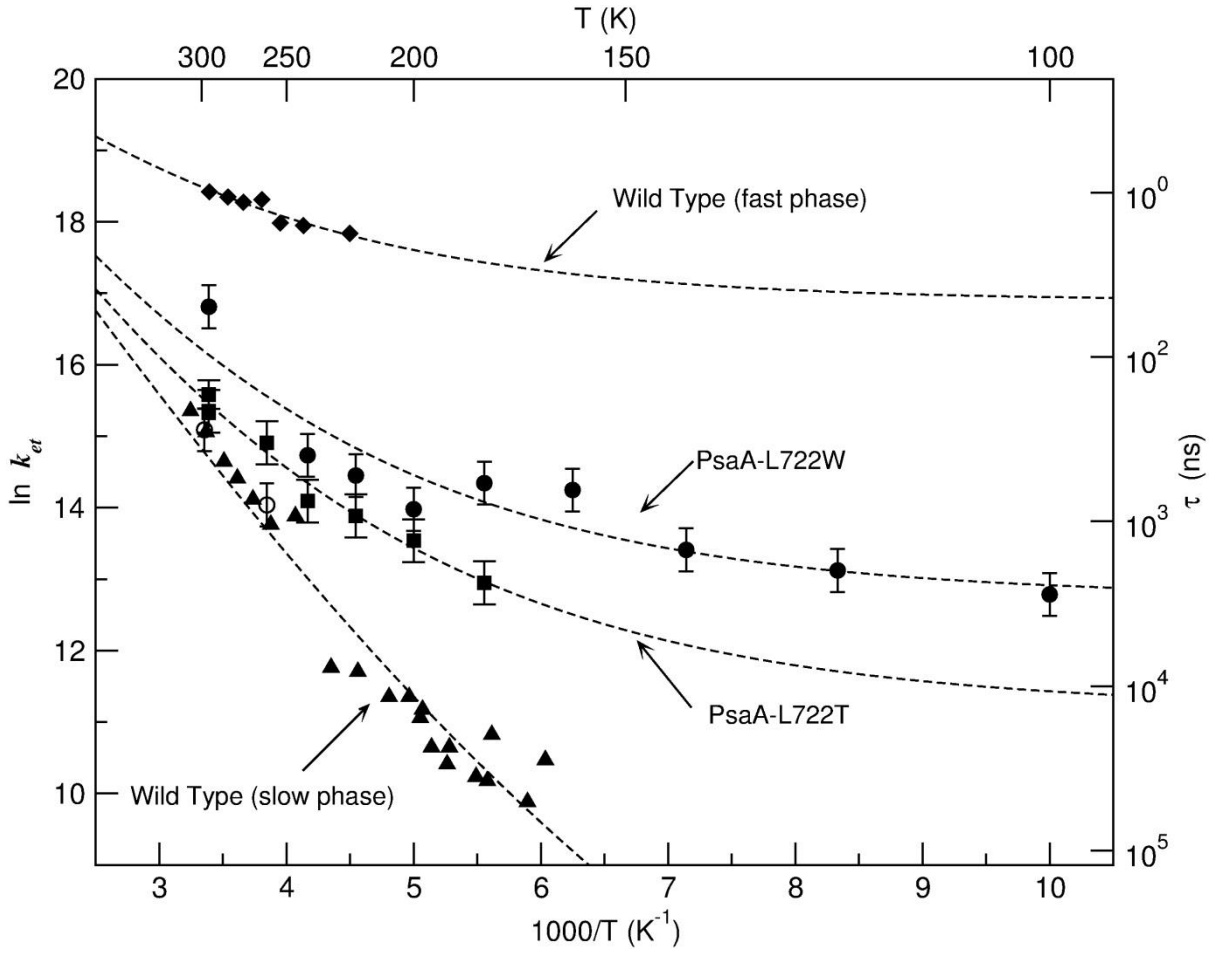

Figure 5-8: Temperature dependence of the rate of ET from phylloquinone to F_X. Squares: PsaA-L722T, EPR data (this work); closed circles: PsaA-L722W, EPR data from reference[9]; open circles: wild type slow phase, EPR data from reference[9]; triangles: wild type slow phase, optical data from reference[41]; diamonds: wild type fast phase, optical data from reference[42]. The dashed curves are fits of the data using the semi-classical approach developed by Hopfield.[43] The parameters used are discussed in the text.

The measured rates are shown as an Arrhenius plot in Figure 5-8 along with data from the literature for the two phases in the wild type[41, 42] and the PsaA-L722W mutant[9].

As can be seen in Figure 5-8, the difference between the ET rate in the PsaA-L722T mutant (squares) and the slow phase in the wild type (diamonds) becomes quite large as the temperature is decreased such that they differ by roughly a factor of 10 at 200 K. In contrast to this difference, the temperature dependences of the rates for the PsaA-L722T mutant and the PsaA-L722W mutant are roughly parallel. The fast phase of the wild type is also included in the plot for comparison. To identify possible origins for the different temperature dependences of the different samples we have fit the data using the semi-classical Marcus equation derived by Hopfield: [43]

$$k_{ET} \propto \frac{1}{\sqrt{2\pi\lambda\hbar\omega Coth\left[\frac{\hbar\omega}{2k_bT}\right]}} \exp-\left(\frac{(\Delta G^o+\lambda)^2}{2\lambda\omega Coth\left[\frac{\hbar\omega}{2k_bT}\right]}\right) \qquad (4.1)$$

where $\hbar\omega\lambda\coth(\hbar\omega/2k_BT)$ is the Gaussian width of the vibrational potential energy surface associated with the ET and ω is the frequency of the vibrational mode. To fit (4.1), to the data in Figure 5-8, the reorganization energy, λ, the electronic coupling $|V|^2$, the activation energy $(\Delta G+\lambda)^2/4\lambda k_B$ and the frequency of the vibrational mode, ω, must be determined. If all four of these parameters are varied simultaneously it is not possible to obtain physically reasonable values for the reorganization energy. Hence, we have chosen to keep it constant at the common value λ = 700 meV found for the ET reactions in purple bacterial reaction centers[37] and only the activation energy, electronic coupling and the frequency of the vibrational mode were varied in the fits. The values obtained for these three quantities are summarized in Table 5-3. For the PsaA-L722T

mutant the activation energy is found to be about 10 meV higher than in the wild type (255 meV versus 243 meV), which is consistent with the expected stabilization of the charge from the additional H-bond between A_{1A} and the threonine side chain. The fits indicate that the higher rate ET rate in the PsaA-L722T mutant compared to the wild type is due to a slight increase in the electronic coupling from 1.04 meV^2 in the wild type to 1.25 meV^2. In contrast to these relatively small changes in the activation energy and electronic coupling, the frequencies of the vibrational modes differ significantly in the wild type versus in the PsaA-L722T mutant (173 cm^{-1} and 320 cm^{-1}, respectively). Whereas, the vibrational frequencies obtained for the two mutants PsaA-L722T and PsaA-L722W are almost the same (320 cm^{-1} and 325 cm^{-1}, respectively) but the activation energy is slightly lower in the PsaA-L722W mutant (233 meV versus 255 meV in the PsaA-L722T mutant). For the fast phase of the wild type, the activation energy is significantly lower (147 meV) and the frequency is much higher (378 cm^{-1}). Thus, there are two main outcomes of these fits. First, they show that both the electronic coupling and the activation energy need to be considered when interpreting small mutation-induced changes in the ET rates. Second, the values for the frequency of the mode that couples to the ET are differ strongly between the kinetic phases of the wild type and between the slow phase in the mutants and in the wild type. In the Hopfield model, the frequency describes the zero point energy and models the transition from classical Arrhenius behavior to quantum mechanical behavior as the temperature is lowered. Importantly, the model does not take coupling of the ET kinetics to the surroundings into account and it is likely that the change in slope in the experimental data reflects the

dynamic arrest of the protein at the glass transition temperature ~200 K rather than quantum mechanical effects.

Table 5-3: Thermodynamic parameters obtained by fitting Equation (4.1) to the electron transfer rates shown in Figure 5-8.

Sample	Activation Energy[a] meV	Electronic Coupling[b] meV^2	Vibrational mode Frequency (cm^{-1})
Wild Type (slow phase)	243	1.04	173
Wild Type (fast phase)	147	0.54	378
PsaA-L722T	255	1.25	320
PsaA-L722W	233	1.04[c]	325

[a]The activation energy is given by $(\Delta G + \lambda)^2 / 4\lambda k_B$. [b]The reorganization energy, λ has been kept fixed at 700 meV. The electronic coupling is $|V|^2$ in equation 1. [c]Held fixed in the fit.

For the A_{1A} to F_X ET step the rate is the range of $10^8 - 10^6$ s^{-1}. Thus, above the protein glass transition temperature at ~200 K[44-46] the dynamic relaxation lifetime, τ_R of the surrounding protein is expected to be shorter than the ET lifetime (τ_{ET}) but below this temperature we have $\tau_{ET} >> \tau_R$. If the ET is coupled to the relaxation of the protein, a change in the slope of the Arrhenius plot is expected at the glass transition temperature. Such behavior is well-known in artificial photosynthetic systems[47] near solvent phase transitions and accounts for their dramatically altered electron transfer kinetics observed in the nematic phase of liquid crystalline solvents. Recently, a description of the temperature dependence near the glass transition temperature that takes the freezing out of the protein relaxation into account has been proposed[48] and from molecular dynamics simulations, it has been suggested that it can lead to a temperature independent

ET rate below the glass transition temperature [49, 50]. The transition from activated to activationless ET occurs when modes of the protein coupled to ET become slower than the ET rate. The data in Figure 5-8 suggest that for the A_{1A} to F_X ET step, freezing out of the protein motion leads to temperature independent ET at the rate reached at the glass transition temperature.

5.4 Conclusions

The EPR data and calculations presented here strongly suggest that in the PsaA-L722T mutant an H-bond is formed between the phylloquinone O_4 and the Thr sidechain OH group. The change in the H-bonding appears to cause a shift of the reduction midpoint potential of the quinone to a more positive value, which results in a slightly higher activation energy. However, the higher activation barrier appears to be offset by slightly stronger electronic coupling between A_{1A} to F_X and as a result a small increase in the rate occurs. The deviations from linearity of the Arrhenius plots of the A_{1A} to F_X electron transfer in the PsaA-L722T and PsaA-L722W mutants near the protein glass transition temperature is a strong indication that protein relaxation plays an important role in determining the rate of this step.

5.5 Acknowledgement

This work was support by Discovery Grants from the Natural Sciences and Engineering Research Council, Canada to AvdE and H.G. and by the United States Department of Energy Energy Biosciences Grant DE-FG02-08ER15989 to K.E.R.

5.6 References

1. Heinnickel, M., R. Agalarov, N. Svensen, C. Krebs, and J.H. Golbeck, *Identification of F_X in the heliobacterial reaction center as a [4Fe-4S] cluster with an S = (3)/(2) ground spin state.* Biochemistry, 2006. **45**(21): p. 6756-6764.
2. Li, Y., A. van der Est, M.G. Lucas, V.M. Ramesh, F. Gu, A. Petrenko, S. Lin, A.N. Webber, F. Rappaport, and K. Redding, *Directing electron transfer within Photosystem I by breaking H-bonds in the cofactor branches.* Proc. Natl. Acad. Sci. U. S. A., 2006. **103**(7): p. 2144-2149.
3. Ishikita, H. and E.W. Knapp, *Redox potential of quinones in both electron transfer branches of photosystem I.* Journal of Biological Chemistry, 2003. **278**(52): p. 52002-52011.
4. Prince, R.C., P.L. Dutton, and J.M. Bruce, *Electrochemistry of Ubiquinones - Menaquinones and Plastoquinones in Aprotic-Solvents.* FEBS Lett., 1983. **160**(1-2): p. 273-276.
5. Jordan, P., P. Fromme, H.T. Witt, O. Klukas, W. Saenger, and N. Kraub, *Three-dimensional structure of cyanobacterial photosystem I at 2.5 A resolution.* Nature, 2001. **411**(6840): p. 909-917.
6. Dashdorj, N., W. Xu, R.O. Cohen, J.H. Golbeck, and S. Savikhin, *Asymmetric electron transfer in cyanobacterial photosystem I: Charge separation and secondary electron transfer dynamics of mutations near the primary electron acceptor A(0).* Biophysical Journal, 2005. **88**(2): p. 1238-1249.
7. Käss, H., P. Fromme, H.T. Witt, and W. Lubitz, *Orientation and Electronic Structure of the Primary Donor Radical Cation in Photosystem I: A Single Crystals EPR and ENDOR Study.* The Journal of Physical Chemistry B, 2001. **105**(6): p. 1225-1239.
8. Koradi, R., M. Billeter, and K. Wuthrich, *MOLMOL: A program for display and analysis of macromolecular structures.* J Mol Graphics, 1996. **14**(1): p. 51-&.
9. Srinivasan, N., S. Santabarbara, F. Rappaport, D. Carbonera, K. Redding, A. van der Est, and J.H. Golbeck, *Alteration of the H-Bond to the A_{1A} Phylloquinone in Photosystem I: Influence on the Kinetics and Energetics of Electron Transfer.* J. Phys. Chem. B, 2011. **115**(8): p. 1751-1759.
10. Srinivasan, N. and J.H. Golbeck, *Protein–cofactor interactions in bioenergetic complexes: The role of the A_{1A} and A_{1B} phylloquinones in Photosystem I.* Biochimica et Biophysica Acta (BBA) - Bioenergetics, 2009. **1787**(9): p. 1057-1088.
11. Santabarbara, S., I. Kuprov, O. Poluektov, A. Casal, C.A. Russell, S. Purton, and M.C.W. Evans, *Directionality of Electron-Transfer Reactions in Photosystem I of Prokaryotes: Universality of the Bidirectional Electron-Transfer Model.* J. Phys. Chem. B, 2010. **114**(46): p. 15158-15171.
12. Santabarbara, S., L. Galuppini, and A.P. Casazza, *Bidirectional Electron Transfer in the Reaction Centre of Photosystem I.* Journal of Integrative Plant Biology, 2010. **52**(8): p. 735-749.
13. Petrenko, A., A.L. Maniero, J. van Tol, F. MacMillan, Y.J. Li, L.C. Brunel, and K. Redding, *A high-field EPR study of P-700(+center dot) in wild-type and*

mutant photosystem I from Chlamydomonas reinhardtii. Biochemistry, 2004. **43**(7): p. 1781-1786.
14. Picard, V., E. Ersdalbadju, A.Q. Lu, and S.C. Bock, *A Rapid and Efficient One-Tube Pcr-Based Mutagenesis Technique Using Pfu DNA-Polymerase.* Nucleic Acids Res, 1994. **22**(13): p. 2587-2591.
15. Subramanyam, R., C. Jolley, D.C. Brune, P. Fromme, and A.N. Webber, *Characterization of a novel photosystem I-LHCI supercomplex isolated from Chlamydomonas reinhardtii under anaerobic (State II) conditions.* FEBS Lett., 2006. **580**(1): p. 233-238.
16. Guex, N. and M.C. Peitsch, *SWISS-MODEL and the Swiss-PdbViewer: An environment for comparative protein modeling.* Electrophoresis, 1997. **18**(15): p. 2714-2723.
17. Case, D.A., T.E. Cheatham, T. Darden, H. Gohlke, R. Luo, K.M. Merz, A. Onufriev, C. Simmerling, B. Wang, and R.J. Woods, *The Amber biomolecular simulation programs.* Journal of Computational Chemistry, 2005. **26**(16): p. 1668-1688.
18. Phillips, J.C., R. Braun, W. Wang, J. Gumbart, E. Tajkhorshid, E. Villa, C. Chipot, R.D. Skeel, L. Kale, and K. Schulten, *Scalable molecular dynamics with NAMD.* Journal of Computational Chemistry, 2005. **26**(16): p. 1781-1802.
19. Cornell, W.D., P. Cieplak, C.I. Bayly, I.R. Gould, K.M. Merz, D.M. Ferguson, D.C. Spellmeyer, T. Fox, J.W. Caldwell, and P.A. Kollman, *A 2nd Generation Force-Field for the Simulation of Proteins, Nucleic-Acids, and Organic-Molecules.* J. Am. Chem. Soc., 1995. **117**(19): p. 5179-5197.
20. Ceccarelli, M., P. Procacci, and M. Marchi, *An ab initio force field for the cofactors of bacterial photosynthesis.* Journal of Computational Chemistry, 2003. **24**(2): p. 129-142.
21. Vasil'ev, S. and D. Bruce, *A protein dynamics study of photosystem II: The effects of protein conformation on reaction center function.* Biophysical Journal, 2006. **90**(9): p. 3062-3073.
22. Mouesca, J.M., J.L. Chen, L. Noodleman, D. Bashford, and D.A. Case, *Density-Functional Poisson-Boltzmann Calculations of Redox Potentials for Iron-Sulfur Clusters.* J. Am. Chem. Soc., 1994. **116**(26): p. 11898-11914.
23. Ryckaert, J.P., G. Ciccotti, and H.J.C. Berendsen, *Numerical-Integration of Cartesian Equations of Motion of a System with Constraints - Molecular-Dynamics of N-Alkanes.* J Comput Phys, 1977. **23**(3): p. 327-341.
24. Dapprich, S., I. Komaromi, K.S. Byun, K. Morokuma, and M.J. Frisch, *A new ONIOM implementation in Gaussian98. Part I. The calculation of energies, gradients, vibrational frequencies and electric field derivatives.* J Mol Struc-Theochem, 1999. **461**: p. 1-21.
25. Canfield, P., M.G. Dahlbom, N.S. Hush, and J.R. Reimers, *Density-functional geometry optimization of the 150 000-atom photosystem-I trimer.* J Chem Phys, 2006. **124**(2).
26. Stephens, P.J., D.M. McCann, E. Butkus, S. Stoncius, J.R. Cheeseman, and M.J. Frisch, *Determination of absolute configuration using concerted ab initio DFT calculations of electronic circular dichroism and optical rotation: Bicyclo[3.3.1]nonane diones.* J Org Chem, 2004. **69**(6): p. 1948-1958.

27. van der Est, A., C. Bock, J. Golbeck, K. Brettel, P. Setif, and D. Stehlik, *Electron-Transfer from the Acceptor A_1 to the Iron-Sulfur Centers in Photosystem I as Studied by Transient Epr Spectroscopy.* Biochemistry, 1994. **33**(39): p. 11789-11797.
28. Pushkar, Y.N., I. Karyagina, D. Stehlik, S. Brown, and A. van der Est, *Recruitment of a foreign quinone into the A_1 site of photosystem I Consecutive forward electron transfer from A_0 TO A_1 to F_X with anthraquinone in the A_1 site as studied by transient EPR.* Journal of Biological Chemistry, 2005. **280**(13): p. 12382-12390.
29. Cohen, R.O., G. Shen, J.H. Golbeck, W. Xu, P.R. Chitnis, A.I. Valieva, A. van der Est, Y. Pushkar, and D. Stehlik, *Evidence for Asymmetric Electron Transfer in Cyanobacterial Photosystem I: Analysis of a Methionine-to-Leucine Mutation of the Ligand to the Primary Electron Acceptor $A_0^{\dagger}$.* Biochemistry, 2004. **43**(16): p. 4741-4754.
30. Pushkar, Y.N., J.H. Golbeck, D. Stehlik, and H. Zimmermann, *Asymmetric hydrogen-bonding of the quinone cofactor in photosystem I probed by C-13-labeled naphthoquinones.* J. Phys. Chem. B, 2004. **108**(27): p. 9439-9448.
31. Bittl, R., E. Schlodder, I. Geisenheimer, W. Lubitz, and R.J. Cogdell, *Transient EPR and Absorption Studies of Carotenoid Triplet Formation in Purple Bacterial Antenna Complexes.* The Journal of Physical Chemistry B, 2001. **105**(23): p. 5525-5535.
32. Tang, J., M.C. Thurnauer, and J.R. Norris, *Electron-Spin Echo Envelope Modulation Due to Exchange and Dipolar Interactions in a Spin-Correlated Radical Pair.* Chem. Phys. Lett., 1994. **219**(3-4): p. 283-290.
33. Salikhov, K.M., Y.E. Kandrashkin, and A.K. Salikhov, *Peculiarities of Free Induction and Primary Spin Echo Signals for Spin-Correlated Radical Pairs.* Appl. Magn. Reson., 1992. **3**(1): p. 199-216.
34. Zech, S.G., W. Lubitz, and R. Bittl, *Pulsed EPR experiments on radical pairs in photosynthesis: Comparison of the donor-acceptor distances in photosystem I and bacterial reaction centers.* Ber Bunsen Phys Chem, 1996. **100**(12): p. 2041-2044.
35. Zech, S.G., A.J. vanderEst, and R. Bittl, *Measurement of cofactor distances between P_{700}^{+} and A_1^{-} in native and quinone-substituted photosystem I using pulsed electron paramagnetic resonance spectroscopy.* Biochemistry, 1997. **36**(32): p. 9774-9779.
36. Bittl, R. and S.G. Zech, *Pulsed EPR Study of Spin-Coupled Radical Pairs in Photosynthetic Reaction Centers: Measurement of the Distance Between and in Photosystem I and between and in Bacterial Reaction Centers.* The Journal of Physical Chemistry B, 1997. **101**(8): p. 1429-1436.
37. Moser, C.C., J.M. Keske, K. Warncke, R.S. Farid, and P.L. Dutton, *Nature of Biological Electron Transfer.* Nature, 1992. **355**(6363): p. 796-802.
38. Taylor, R., O. Kennard, and W. Versichel, *The Geometry of the N-H ... O=C Hydrogen-Bond .3. Hydrogen-Bond Distances and Angles.* Acta Crystallogr B, 1984. **40**(Jun): p. 280-288.
39. van der Est, A., Y. Pushkar, I. Karyagina, B. Fonovic, T. Dudding, J. Niklas, W. Lubitz, and J. Golbeck, *Incorporation of 2,3-Disubstituted-1,4-Naphthoquinones*

into the A_1 Binding Site of Photosystem I Studied by EPR and ENDOR Spectroscopy. Appl. Magn. Reson., 2010. **37**(1-4): p. 65-83.

40. Kandrashkin, Y.E., W. Vollmann, D. Stehlik, K. Salikhov, and A. Van der Est, *The magnetic field dependence of the electron spin polarization in consecutive spin correlated radical pairs in type I photosynthetic reaction centres.* Mol Phys, 2002. **100**(9): p. 1431-1443.
41. Schlodder, E., K. Falkenberg, M. Gergeleit, and K. Brettel, *Temperature Dependence of Forward and Reverse Electron Transfer from A_1^-, the Reduced Secondary Electron Acceptor in Photosystem I^+*. Biochemistry, 1998. **37**(26): p. 9466-9476.
42. Agalarov, R. and K. Brettel, *Temperature dependence of biphasic forward electron transfer from the phylloquinone(s) A_1 in photosystem I: only the slower phase is activated.* Biochim. Biophys. Acta-Bioenerg., 2003. **1604**(1): p. 7-12.
43. Hopfield, J.J., *Electron-Transfer Between Biological Molecules by Thermally Activated Tunneling.* Proc. Natl. Acad. Sci. U. S. A., 1974. **71**(9): p. 3640-3644.
44. Doster, W., S. Cusack, and W. Petry, *Dynamical Transition of Myoglobin Revealed by Inelastic Neutron-Scattering.* Nature, 1989. **337**(6209): p. 754-756.
45. Ferrand, M., A.J. Dianoux, W. Petry, and G. Zaccai, *Thermal Motions and Function of Bacteriorhodopsin in Purple Membranes - Effects of Temperature and Hydration Studied by Neutron-Scattering.* Proc. Natl. Acad. Sci. U. S. A., 1993. **90**(20): p. 9668-9672.
46. Rasmussen, B.F., A.M. Stock, D. Ringe, and G.A. Petsko, *Crystalline Ribonuclease-a Loses Function Below the Dynamic Transition at 220-K.* Nature, 1992. **357**(6377): p. 423-424.
47. Wiederrecht, G.P., W.A. Svec, and M.R. Wasielewski, *Triplet states with unusual spin polarization resulting from radical ion pair recombination at short distances.* J. Am. Chem. Soc., 1999. **121**(33): p. 7726-7727.
48. Matyushov, D., *Thermodynamics of electron transfer.* Abstr Pap Am Chem S, 2005. **230**: p. U2968-U2968.
49. LeBard, D.N. and D.V. Matyushov, *Dynamical transition, hydrophobic interface, and the temperature dependence of electrostatic fluctuations in proteins.* Phys Rev E, 2008. **78**(6).
50. LeBard, D.N. and D.V. Matyushov, *Energetics of Bacterial Photosynthesis.* J. Phys. Chem. B, 2009. **113**(36): p. 12424-12437.

The following published work has been included in this thesis with permission from the Journal of Photochemical and Photobiological Sciences. The entire work was completed by the authors listed below. The *menB* PSI mutant and wild-type were grown and purified by SM of Brock University as well as the incubation experiments for incorporation of foreign quinone 2,3 dichloro-1,4-naphthoquinone. The cyclic voltammetry measurements were carried out by SM of Brock University. The X-Band and Q-Band CW, transient and pulsed EPR experiments were carried out by SM of Brock University under the supervision of AVE of Brock University. The transient absorbance measurements were carried out by SM with the collaborative efforts of JG at Penn State University. The W-Band CW, transient and pulsed EPR and RIDME experiments were carried out by AS, KM and WL of the Max Planck Institute in Mulheim, Germany. The menB/rubA mutant PSI fragments were donated by Mike Gorka of Penn State University under the supervision of JG.

Chapter 6 Incorporation of a High Potential Quinone Reveals that Electron Transfer in Photosystem I Becomes Highly Asymmetric at Low Temperature

Sam Mula,[†] *Anton Savitsky,**[‡] *Klaus Möbius,*[‡,+] *Wolfgang Lubitz*[‡], *John H. Golbeck,*[§, ⊥] *MahirD. Mamedov*[¶], *Alexey Yu. Semenov,**[¶] *Art van der Est**[†]

[†] Department of Chemistry, Brock University, St. Catharines ON, Canada
[‡] Max-Planck-Institut für Bionanorganische Chemie 45470 Mülheim and der Ruhr, Germany
[+] Department of Physics, Free University Berlin, 14195 Berlin, Germany
[§] Department of Biochemistry and Molecular Biology, [⊥]Department of Chemistry, The Pennsylvania State University, University Park, Pennsylvania 16802, United States

¶ Moscow State University, AN Belozersky Institute of Physical-Chemical Biology, Moscow 119992, Leninskie Gory, Russia.
*To whom correspondence should be addressed:
(A.v.d.E) Email: avde@brocku.ca. Tel. +1 905 688 5550. Fax: +1 905 682 9020
(A.S.) Email: savitsky@mpi-muelheim.mpg.de. Tel.: +49 208 3063555. Fax: +49 208 3063955 (A.Yu.S.) Email: semenov@genebee.msu.ru. Tel.: +7 495 939 3188. Fax: +7 495 939 3181
Dedicated to Prof. Kurt Schaffner (Mülheim/Ruhr) on the occation of his 80th birthday.

6.1 Introduction

In Photosystem I (PS I) the PsaA and PsaB protein subunits bind two branches of electron-transfer cofactors extending from P_{700}, a chlorophyll *a* / chlorophyll *a*' dimer, on the lumenal side of the thylakoid membrane to the iron-sulfur cluster F_X on the stromal side (Figure 6-1). Each of the two branches carries two monomeric chlorophyll *a* molecules, $A_{-1A(B)}$ and $A_{0A(B)}$, and a phylloquinone molecule, $A_{1A(B)}$, where A and B indicate the protein subunit PsaA or PsaB to which the cofactor is mainly bound. The terminal iron-sulfur clusters, F_A and F_B are both bound to the protein subunit PsaC. Upon light excitation at room temperature, electrons are transferred from P_{700} to F_B *via* the intervening cofactors. Although there is some debate about whether the initial charge separation occurs independently in each branch between A_0 and A_1 [1] or between P_{700} and A_0 [2], there is general consensus that both branches of cofactors are active in electron transfer. This conclusion has been reached primarily from point-mutation studies, which show that at room temperature the 200 ns phase of A_1 to F_X electron transfer occurs in the A-branch while the 20 ns phase occurs in the B-branch. [3-9]

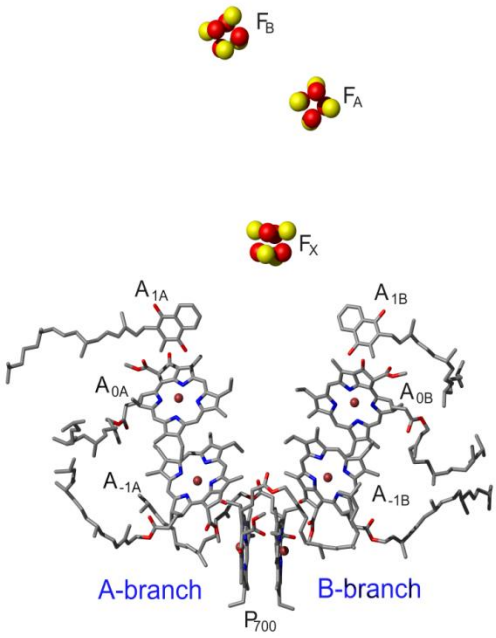

Figure 6-1 Structural arrangement of the electron-transfer cofactors in Photosystem I. The positions of the cofactors are from the 2.5 Å resolution X-ray structure [10] (PDB entry 1JB0).

In contrast to the behavior in PS I, electron transfer in reaction centers from purple bacteria and Photosystem II is unidirectional along the A-branch and extremely difficult to re-direct into the inactive B-branch. This difference appears to be related to the fact that in type II reaction centers electron transfer proceeds from the A-branch quinone to the B-branch quinone, which exchanges with the quinone pool following double reduction and protonation. In Photosystem I, on the other hand, both branches of cofactors converge at F_X and there is no obvious functional advantage to uni-directionality or bi-directionality. At present the factors that determine the relative use of the two branches and lead to such a large difference between type I and type II reaction centers are not well understood and in this context it is of interest to study the temperature dependence of the directionality. In type II reaction centers, the very strong bias towards the A-branch of the electron transfer does not depend on temperature. In PS I, the relative electron-transfer activity of the two branches below the glass-transition

temperature of the protein at about 200 K is less certain because the kinetic behavior becomes heterogeneous. At least two fractions of PS I complexes are observed in which either irreversible electron transfer to F_A and F_B, or reversible electron transfer to A_1 and/or F_X occurs. [11] Electron transfer in the A-branch from A_{1A} to F_X is strongly activated [12], while the corresponding step in the B-branch is nearly activationless. [13] Consistent with this difference in the activation energies, low-temperature EPR studies of branch specific point mutants show that reversible electron transfer to A_1 occurs exclusively in the A-branch. [6, 8, 14-16] However, this observation does not answer the question of the directionality at low temperature because the pathway leading to irreversible charge separation remains unclear.

To address this issue it is necessary to prevent electron transfer past A_1 so that irreversible charge separation does not occur. A number of studies have been carried out in which forward electron transfer past A_1 has been blocked by pre-reduction of the iron-sulfur clusters [4, 14, 17-21] and/or in which A-branch electron transfer is partially hindered by mutation of PsaA-M688, which provides the axial ligand to A_{0A}. [21, 22] Under these conditions, additional components with different kinetic and spectral properties are observed in the time-resolved EPR signals from $P_{700}^{+}A_1^{-}$. Modeling of the spin-polarized EPR spectra and out-of-phase electron-spin echo-envelope modulation (ESEEM) curves suggest that under reducing conditions, or when electron transfer in the A-branch is hindered, components arising from both the A- and B-branch radical pairs $P_{700}^{+}A_{1A}^{-}$ and $P_{700}^{+}A_{1B}^{-}$ are observed. These results have been interpreted as indicating that the electron transfer is also bidirectional at low temperature. [21] However, it has also been suggested that the electron transfer is highly biased towards the A-branch [15,

22] Another method of preventing electron transfer past A_1 is to inhibit the assembly of F_X. It has been shown that deletion of the *rubA* gene of *Synechocystis* sp. PCC 6803, which encodes for a rubredoxin that is involved in the assembly of PS I, results in complexes lacking the iron-sulfur clusters F_A, F_B and F_X in which no irreversible electron transfer is observed at low temperature. [23, 24] In contrast to the pre-reduced samples, the low-temperature time-resolved EPR spectra and echo-modulation curves of PS I complexes from the *rubA* variant are indistinguishable from the wild type and show no evidence for electron transfer in the B-branch. [7, 24]

The difference in behavior between the prereduced samples and the *rubA* variant suggests that the directionality may be altered by either reduction or removal of F_X. Indeed it has been shown that electrons can be re-directed into the B-branch by mutations [8] and/or harsh solubilization methods. [25] Thus, it is conceivable that either reduction at high pH or the absence of the iron-sulfur clusters could alter the directionality. Here we address this issue by incorporating the high potential quinone, 2,3-dichloro-1,4-naphthoquinone (Cl_2NQ) into the A_1 binding sites of PS I to prevent forward electron transfer to the iron-sulfur clusters. To incorporate Cl_2NQ we use PS I from the *menB* variant of *Synechocystis* sp. PCC 6803. Inactivation of the *menB* gene, which codes for a naphthoate synthase, inhibits the biosynthesis of phylloquinone [26] and in its absence, plastoquinone-9 binds to the A_{1A} and A_{1B} sites. [26] Because the binding of plastoquinone-9 is relatively weak it can be displaced by incubation with a wide variety of naphthoquinones. [15, 27-30] The structures of phylloquinone, plastoquinone-9 and Cl_2NQ are shown in Figure 6-2 along with their first reduction midpoint potentials in dimethyl formamide (DMF). The reduction potential of Cl_2NQ in DMF is more than

400 mV more positive than that of phylloquinone, and the premise of the experiments presented here is that a similar difference in the potentials of phylloquinone and Cl_2NQ would be expected in the A_{1A} and A_{1B} binding sites. Estimates of the midpoint potential of the B-branch phylloquinone place it 25 mV, [18] 155 mV [31] or 173 mV [32] more negative than the A-branch phylloquinone. If our premise is correct, electron transfer from Cl_2NQ to F_X in both branches should require a larger activation energy than the phylloquinone to F_X transfer in the A-branch of native PS I.

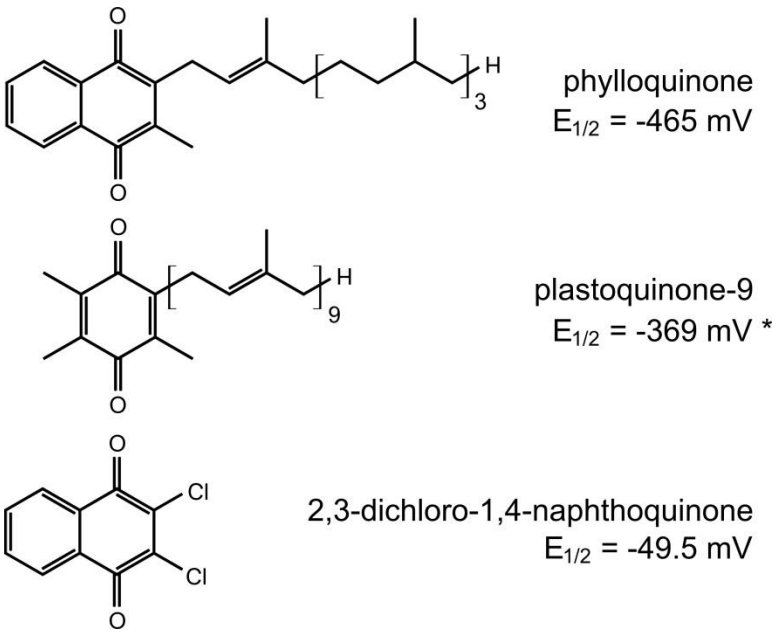

Figure 6-2 Structures of phylloquinone, plastoquinone-9 and Cl_2NQ and their first reduction midpoint potentials in DMF versus the normal hydrogen electrode. (*) The midpoint potential for plastoquinone-9 is taken from the literature. [33]

The main advantage of blocking electron transfer in this way is that neither pre-reduction nor removal of the iron sulfur clusters are required and, hence, possible changes in the structure, electrostatic environment, protonation state of the protein, etc. should be minimized. We will show that the multi-frequency time-resolved EPR data from these

samples are consistent with uni-directional electron transfer in the A-branch and do not show any of the characteristic features that have been associated with the B-branch radical pair $P_{700}^{+}A_{1B}^{-}$.

6.2 Materials and Methods

6.2.1 Growth and Isolation of PS I from the menB and menB/rubA Mutants.

The *menB* deletion mutant strain of *Synechocystis* sp. PCC 6803 was grown under low light, and trimeric PS I complexes were isolated as described previously. [34] The isolated trimers were brought to a chlorophyll *a* concentration of 2 mg/mL by centrifuging to a thick paste using 100K Ultracell purification membranes followed by resuspension in a 50 mM Tris-buffer at pH 8.0 containing 0.05% n-dodecyl-β-D-maltoside and 1% glycerol as a cryo-protectant. The *menB/rubA* mutant strain of *Synechocccocus* sp. PCC 7002 was grown and thylakoid membrane fragments were prepared as described previously [35] and the thylakoid suspension was centrifuged to a chlorophyll-*a* concentration of 16 mg/mL. Photosystem I particles were not isolated from the thylakoids to avoid detergent-induced structural changes.

6.2.2 Incubation of PS I with Cl_2NQ.

1,2-dichloro-1,4-naphthoquinone was obtained from Sigma-Aldrich Chemicals and was dissolved in DMSO. For the *menB* trimers, a 10 µL aliquot of a 20 mM Cl_2NQ solution was added to approximately 100 µL of a PS I trimer solution at a chlorophyll-*a* concentration of 2 mg/mL. The samples were incubated for one hour on ice before being

washed with one 4 mL aliquot of buffer and centrifuged to a thick paste followed by resuspension to a volume of 150 μL.

The *menB/rubA* thylakoid suspension was incubated with 5 μL of a 4 mM solution of Cl_2NQ for 1 hour. This process was carried out in low light to reduce damage to the double mutant.

6.2.3 Cyclic Voltammetry of Quinones in DMF.

Reduction-wave voltammograms of phylloquinone and Cl_2NQ were measured using a BAS Epsilon and C3 Cell Stand (Bioanalytical Systems) with a platinum working electrode, a 3 M NaCl Ag/AgCl reference electrode and a platinum auxiliary electrode. The samples were prepared by dissolving ~ 5 mg of the quinones and 0.15 g of the supporting electrolyte tetrabutylammonium-hexafluorate-phosphate in 10 mL of dry DMF. The solutions were bubbled with nitrogen gas for five minutes to remove oxygen. Voltammograms were cycled between +250 mV and -2000 mV.

6.2.4 Time-Resolved Optical Spectroscopy at 700 nm.

The samples were diluted to a chlorophyll concentration of 10 μg/mL. The samples contained 5 mM sodium ascorbate, 4 μM DCPIP as an exogenous donor and were prepared under aerobic conditions.

6.2.5 Time-Resolved Optical Spectroscopy in the Near-Infrared Region.

The decay of P_{700}^+ due to charge recombination was measured at 820 nm using a laboratory-built time-resolved spectrophotometer. The samples were diluted to a chlorophyll concentration of 50 μg/mL and placed in a quartz cuvette with a path length of 10 mm. The samples contained 10 mM sodium ascorbate, 4 μM DCPIP as an

exogenous donor and were prepared in an anaerobic chamber with an atmosphere of 10% hydrogen and 90% nitrogen. The kinetic traces were analyzed by fitting a multiexponential decay using the Marquardt least-squares algorithm programmed in the Igor Pro language (Wavemetrics).

6.2.6 Time-Resolved and CW EPR Experiments at X-band and Q-band.

Samples for the EPR experiments at X- and Q-band contained 1 mM sodium ascorbate and 50 μM phenazine methosulfate as an external electron donor and were dark adapted for 20 min before being frozen in the dark. The EPR experiments were carried out using a Bruker Elexsys E580 spectrometer or a modified Bruker ER 200D-SRC spectrometer as described previously.[36] For the time-resolved EPR (TREPR, direct detection without field modulation or echo-detected pulse EPR) experiments the samples were illuminated at 532 nm and 10 Hz using a Nd:YAG laser (Continuum Surelite). To determine the throughput of electrons to the terminal iron-sulfur clusters at low temperature the samples were frozen to 15 K in the dark and then illuminated continuously for five minutes with white light from a Schott KL-1500 visible wavelength lamp with an intensity of 1.3 μE s^{-1} to accumulate $[F_A/F_B]^-$ The CW-EPR spectra of $[F_A/F_B]^-$ were collected using 100 KHz field modulation with an amplitude of 1.0 mT and a nominal microwave power of 1.0 mW. The spectrum taken before illumination was subtracted to remove background signals from the resonator.

X-band out-of-phase ESEEM curves were collected at 80 K on the Bruker Elexsys E580 spectrometer. The echo was generated using a hν-T_{DAF}-(t_p)-τ-($3t_p$)-τ-*echo* pulse sequence with t_p= 8 ns (π/3), and τ_0 = 80 ns and $\Delta\tau$ = 4 ns. The echo intensity was integrated over a

100 ns window centered at the echo maximum. The delay between laser flash and initial microwave pulse, T_{DAF} was 300 ns.

6.2.7 W-band EPR Experiments.

High-field EPR measurements were performed on a home-built W-band (95 GHz/3.4 T) multipurpose EPR spectrometer described previously. [37, 38] The sample solutions were placed in a quartz capillary (0.6 mm I.D.), transferred to the EPR probe head and, after dark adaptation at room temperature for 10 min, cooled down to 120 K. Light-induced electron transfer was initiated by light pulses at 532 nm (Nd:YAG laser, 5 ns pulse width, 0.5 mJ on the sample surface) guided to the center of the TE_{011} optical transmission EPR cavity through a quartz fiber of 0.8 mm diameter. The recombination kinetics were obtained by recording the short-lived EPR absorption after laser flash via lock-in detection with magnetic field modulation (30 kHz, 0.1 mT modulation amplitude). The time resolution of this detection technique was thus set to about 100 μs. The pulsed EPR measurements were performed using the Hahn-echo sequence $(t_p) - \tau - (2t_p) - \tau$-*echo* allowing for a time after laser flash, T_{DAF}, in the sequence $h\nu$-T_{DAF}-$(t_p)_{x,-x}$-τ-$(2t_p)$-τ-*echo* under pulsed light illumination with repetition rate of 2 Hz. The t_p pulse length of the $\pi/2$ microwave (mw) pulses was generally set to 30 ns. The quadrature-detected echo traces, (s_{-y}, s_x), were digitized and transferred to the computer for further evaluation. To obtain the in-phase field-swept EPR spectra, the s_{-y} echo response traces at $\tau = 150$ ns, corresponding to the first pulse phase settings +x and –x, were subtracted from each other, and the pure echo response, i.e., free of FID and cavity ringing signals, was integrated over the whole echo duration. The out-of-phase EPR decay profiles were evaluated from s_x echo traces by integrating the echo responses over the time window,

centered at the s_{-y} echo maximum, that covers 60% of the echo intensity to optimize resolution and signal-to-noise ratio.

The single-frequency pulse dipolar EPR experiment of the RIDME type is based on measuring the out-of-phase stimulated echo signal ($h\nu$ - T_{DAF} - $(t_p)_{x,-x}$ - τ - (t_p) - T - (t_p) - τ -*echo*) as a function of the preparation time τ. [39] The fixed mixing time T should be long enough to allow the longitudinal spin relaxation to flip the partner spins in the pair, but short enough to avoid a considerable reduction of the echo signal caused by the longitudinal spin relaxation of the observer spins and by the charge recombination. At 120 K the mean relaxation time for the radical pair was measured, by probing 2-pulse echoes vs. T_{DAF}, to be about 30 µs. Thus, a setting of T = 20 µs satisfies the RIDME requirement. The complete RIDME data set is composed of recordings (T_{DAF}= 400 ns, τ_0 = 50 ns, $\Delta\tau$ = 10ns) detected at field positions stepped through the A_1 spectral region.

6.3 Results

6.3.1 Room-Temperature P_{700}^+ Recombination Kinetics.

The kinetics of charge recombination in PS I following a saturating light flash have been shown to be dependent on the midpoint potential of the quinone in the A_{1A} and A_{1B} sites. [40, 41] Hence, the back-reaction kinetics can be used to monitor the incorporation of Cl_2NQ into the binding site. As displayed in Figure 6-3, and summarized in Table 6-1, the absorbance difference traces taken in the near-IR show that the main kinetic component of the back reaction has lifetimes of 3.5 ms and 140 µs in PS I from the *menB* variant and the *menB* variant incubated with Cl_2NQ, respectively. The trace from the incubated sample (Figure 6-3 bottom) shows no evidence of the 3.5 ms decay associated

with the presence of plastoquinone-9. The main kinetic components of the back reaction observed at 700 nm under aerobic conditions had similar lifetimes (see Table 6-1). Hence, we conclude that essentially complete displacement of plastoquinone-9 by Cl_2NQ has occurred in the back-reaction pathway. Both lifetimes are significantly faster than the 85 ms lifetime observed in the wild type. [40] A positive shift of the quinone potential is expected to lead to faster back-reaction because the equilibrium between forward and back electron transfer between the quinone and F_X will shift towards the quinone, resulting a faster overall rate. [42] Consistent with this expectation, the rate of the back reaction with Cl_2NQ in the binding site is ~30 times faster than with plastoquinone-9, and ~900 times faster than with phylloquinone. The small slow component is due to donation to P_{700}^+ by the external donor DCPIP when the transferred electron is lost to oxygen or other acceptors

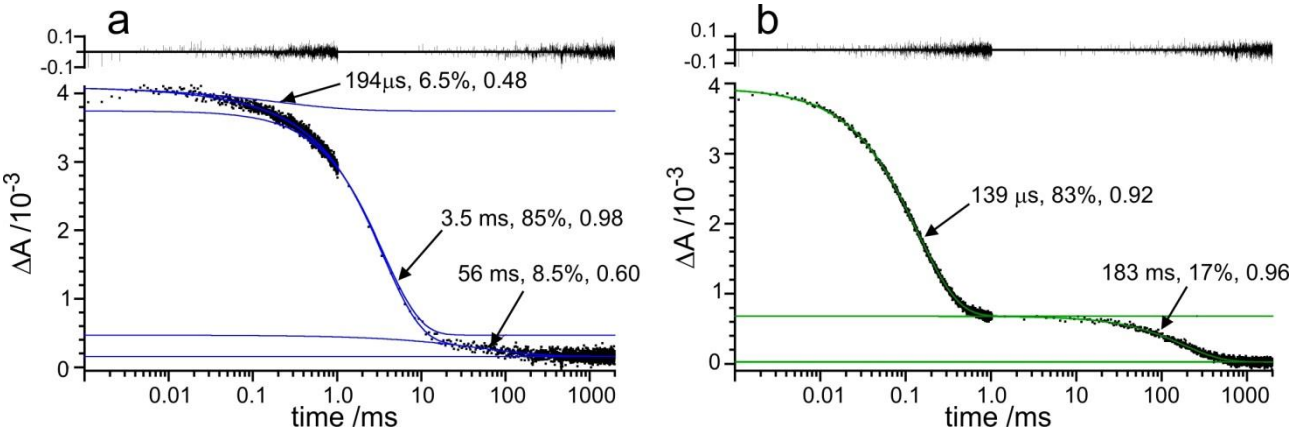

Figure 6-3 Room temperature P_{700}^+ reduction kinetics measured at 820 nm in the *menB* variant (a) and the *menB* variant incubated with Cl_2NQ (b). The experimental absorption difference data are shown in black and the blue and green curves are fits of a weighted sum of stretched exponentials to the data. The lifetimes, relative amplitudes and stretch factors of the individual kinetics components are indicated. The residuals are shown above the fit.

6.3.2 Recombination Kinetics at 120 K.

At low temperature the recombination kinetics can be monitored by W-band EPR spectroscopy. At high external magnetic field, the contributions from P_{700}^{+} and A_1^{-} are spectrally well separated, due to the difference in their g-values, and hence their kinetics can be measured independently of one another. Previous studies [12, 22] suggest that at low temperature at least three fractions exist following illumination. The majority of electrons recombine from A_1^{-}, a second fraction is trapped as $P_{700}^{+}(F_A/F_B)^{-}$ and a small amount of recombination occurs from the iron-sulfur clusters, probably from F_X^{-}. The relative magnitudes of the recombining fractions can be estimated from high-field EPR transient responses taken in the P_{700}^{+} and A_1^{-} regions of the spectrum. Figure 6-4 shows a comparison of such transients for the *menB* variant and the *menB* variant incubated with Cl_2NQ. The recombination lifetimes obtained from the traces are summarized in Table 6-1. In Figure 6-4a, transients of the two samples, taken in the P_{700}^{+} region, are compared. As expected, the lifetime of the decay from the Cl_2NQ sample (0.2 ms, green trace) is considerably shorter than that in the *menB* sample (1.1 ms, blue trace). In addition, the *menB* decay is clearly bi-exponential and offset from zero whereas for the Cl_2NQ sample the slow component is absent and the whole signal decays to zero in less than 5 ms. As shown in the inset of Figure 6-4a, the time between consecutive laser flashes is 900 ms, thus the offset of the curve prior to each flash represents the “stable” fraction that decays with a time longer than the repetition rate. In Figure 6-4b traces from the *menB* variant taken in the P_{700}^{+} (blue trace) and A_1^{-} (red trace) regions are compared. As can be seen, the A_1^{-} curve decays with the same 1.1 ms lifetime as the fast component of the P_{700}^{+} trace and, thus, we can conclude that this lifetime characterizes the recombination of

$P_{700}^{+}A_1^{-}$. The fact that the slow-component and offset signals are not observed in the A_1^{-} region suggests that they are due to recombination from F_X^{-} and trapping of $(F_A/F_B)^{-}$, respectively. Since these two components are missing in the trace from the Cl_2NQ sample (Figure 6-4c), we conclude that electron transfer past the quinone is blocked. Also shown in Table 6-1 are the decay times of the spin polarization of $P_{700}^{+}A_1^{-}$ determined by monitoring the echo amplitude as a function of the delay time after the laser flash, T_{DAF}. The decay of the spin polarization due to spin-lattice relaxation, T_1, is mono-exponential and has the same lifetime in both the P_{700}^{+} and A_1^{-} regions of the spectrum. Following the decay of the initial spin polarization to a Boltzmann population distribution, the spin echo signal decays due to charge recombination with the same lifetimes measured using field modulation. Thus, there are no additional faster charge-recombination processes present.

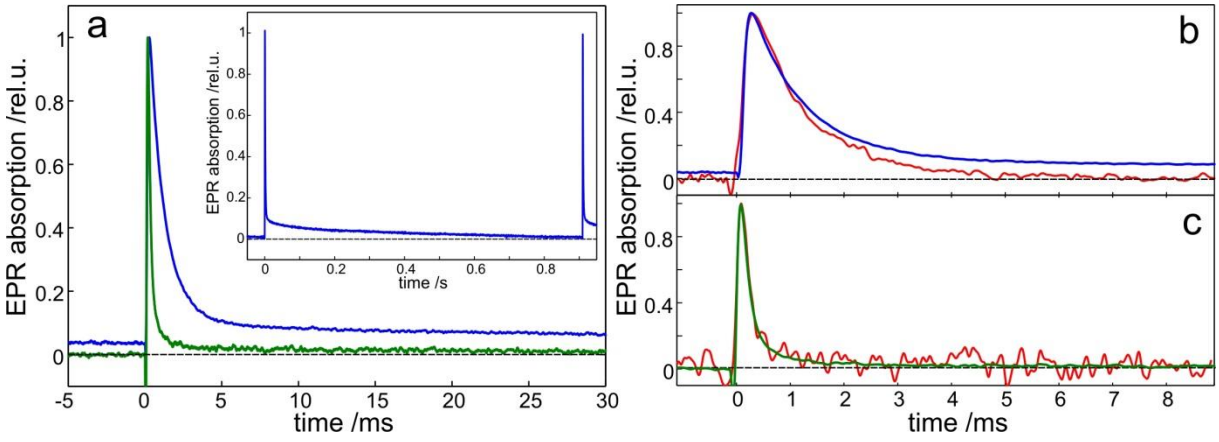

Figure 6-4 Charge-recombination kinetics measured by time-resolved W-band EPR spectroscopy after pulsed laser excitation (532 nm) at 120 K. (a) P_{700}^{+}decay in the *menB* variant (blue line) and the *menB* variant incubated with Cl_2NQ (green line). The inset shows the decay of the *menB* variant on a longer time scale. Decay traces from the *menB* variant (b) and the *menB* variant incubated with Cl_2NQ (c) taken in the P_{700}^{+} and A_1^{-} (red line) spectral regions of the corresponding samples.

Table 6-1 Kinetic parameters of P_{700}^{+} and A_1^{-}.

Sample	T/K	Quantity measured	Lifetime components /ms	Spin polarization lifetime / µs
menB	295	ΔA 820 nm	0.194 (6.5%), 3.54 (85%), 56.3 (8.5%)	
	295	ΔA 700 nm	1.8 (40%), 5.4 (50%), 1780 (10%)	
	120	EPR P_{700}^{+}	1.1 (92%), 270 (8%)	32
	120	EPR A_1^{-}	1.1 (100%)	27
menB + Cl_2NQ	295	ΔA 820 nm	0.139 (83%), 183 (17%)	
	295	ΔA 700 nm	0.20 (67%), 0.74 (7%), 290 (26%)	
	120	EPR P_{700}^{+}	0.2 (100%)	24
	120	EPR A_1^{-}	0.2 (100%)	20

6.3.3 Accumulation of $[F_A/F_B]^{-}$ at 15 K.

The ability of the PS I samples upon illumination to transfer electrons past the quinones can also be monitored by measuring the CW EPR spectrum of photoaccumulated $[F_A/F_B]^{-}$ at 15 K. A comparison of these spectra for the wild type, *menB* variant and *menB* variant with Cl_2NQ is shown in Figure 6-5. In agreement with a previous report [34] the amplitude of the photoaccumulated $[F_A/F_B]^{-}$ spectrum from the wild type and *menB* variant is virtually the same. Note that the peak at about the free-electron g-value near 350 mT is primarily from P_{700}^{+} and is strongly saturated by the high microwave power levels needed to observe $[F_A/F_B]^{-}$. Any other light-induced organic radicals produced in the sample would also contribute in this field region. Because of the saturation and possible presence of other radical species in the sample, the intensity of this EPR peak cannot be reliably interpreted. When the *menB* variant is incubated with a

100-fold excess of Cl_2NQ, only a weak $g \approx 2$ signal is observed and no accumulation of $(F_A/F_B)^-$ occurs (Figure 6-5, bottom). With smaller amounts of Cl_2NQ (5- to 10-fold excess) a weak $[F_A/F_B]^-$ spectrum becomes visible (data not shown) suggesting that a 100-fold excess is needed to fully displace plastoquinone-9 from the A_1 binding sites. Thus, consistent with the kinetic data, the lack of accumulation of $[F_A/F_B]^-$ indicates that Cl_2NQ has been incorporated and that it prevents electron transfer past the quinones.

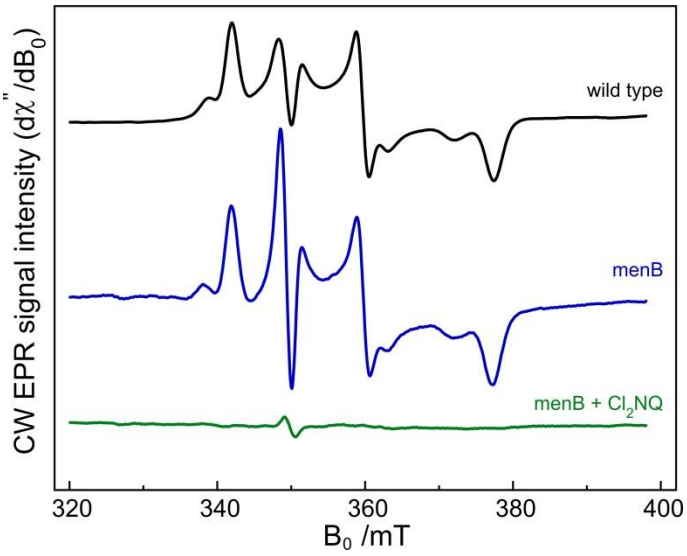

Figure 6-5 Light-induced X-band CW EPR spectra at 15 K of $[F_A/F_B]^-$ in PS I samples frozen in the dark from the wild type (black), *menB* variant (blue) and *menB* variant incubated with Cl_2NQ (green). In each case, a dark background spectrum, collected prior to illumination, was subtracted from the spectrum after illumination. For all three samples, the chlorophyll concentration was 2 mg/mL, the modulation amplitude was 1.0 mT and the microwave power was 1.0 mW. No additional normalization of the spectra was performed.

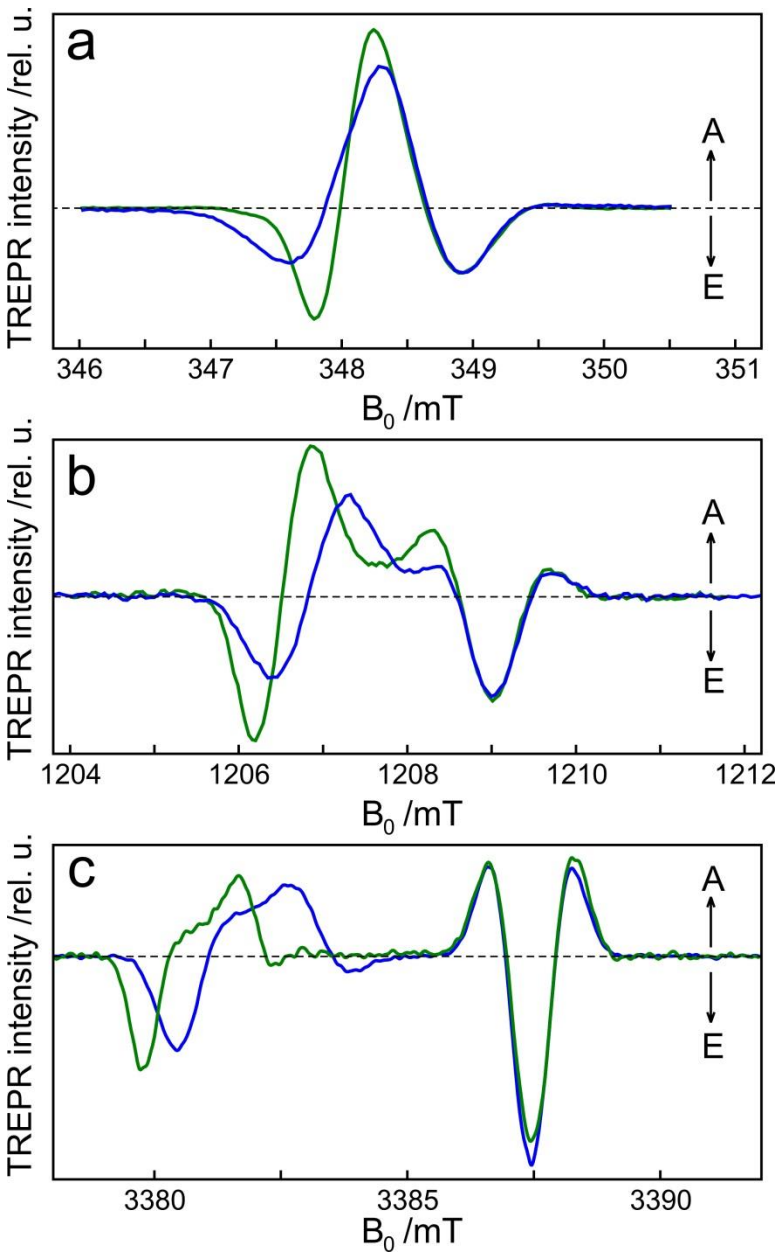

Figure 6-6 Spin-polarized transient EPR spectra of the *menB* variant (blue) and the *menB* variant incubated with Cl_2NQ (green). a: X-band, 80 K; b: Q-band, 80 K; c: W-band, 120 K. The X- and Q-band spectra are the direct detection transient EPR signal, while the W-band spectrum is the echo-detected spectrum. In all cases the spectrum is the difference between the signal intensity 400 ns after the laser flash and the intensity before the flash. The spectra are normalized in such a way that the upfield features, which are primarily due to P_{700}^+, have the same amplitude for both samples.

6.3.4 Low-Temperature TREPR Spectra of $P_{700}^+A_1^-$.

Figure 6-6 shows a comparison of the low-temperature spin-polarized TREPR absorption-emission spectra of the radical pair $P_{700}^+A_1^-$ in PS I particles from the *menB*

variant containing plastoquinone-9 (green spectra) and Cl_2NQ (blue spectra) taken at three different microwave frequencies, X-band (9GHz, Figure 6-6a), Q-band (35 GHz, Figure 6b) and W-band (95 GHz, Figure 6-6c). At all three frequencies the upfield regions, which are dominated by contributions from P_{700}^+, are virtually identical while the downfield regions, which arise from the quinones, differ markedly. At X-band, (Figure 6-6a) the spectral width is determined to a large extent by the proton hyperfine couplings. Plastoquinone-9 has three methyl groups and one methylene group with β-protons with large hyperfine couplings [43], while Cl_2NQ has only ring α-protons with small hyperfine couplings. Therefore, the X-band spectrum from the *menB* sample (green) has a significantly larger width than that of the Cl_2NQ sample (blue). As the microwave frequency and corresponding resonance field are increased, the Zeeman energy becomes increasingly important and the quinone g-tensor components become better resolved at Q-band (Figure 6-6b) and completely resolved at W-band (Figure 6-6c). The two chlorine atoms in Cl_2NQ provide a significant source of spin-orbit coupling and, thus, Cl_2NQ has a larger g-anisotropy than plastoquinone-9. As a result, the spectral features associated with the x- and y-components of the quinone g-tensor are shifted downfield in the Q-band and W-band spectra of the Cl_2NQ sample relative to those of the *menB* sample. Again, this confirms that Cl_2NQ has been incorporated into the A_1 binding site.

The polarization pattern in the P_{700}^+ region of the W-band spectrum is sensitive to the orientation of the dipolar coupling vector relative to the principal axes of the P_{700}^+ g-tensor. [44] Because this orientation is different in the radical pairs $P_{700}^+A_{1A}^-$ and $P_{700}^+A_{1B}^-$ of PS I, their high-field EPR spectra differ in the P_{700}^+ region, as has been demonstrated using pre-reduced PS I samples. [19] The fact that this region is virtually

identical in the *menB*, *menB* plus Cl_2NQ and wild-type (not shown) samples indicates that there is no additional contribution from the B-branch radical pair when electron transfer past the quinone is blocked in the Cl_2NQ sample. Simulation of the quinone region of the W-band spectra reveals that the spectrum of the Cl_2NQ sample contains a minor contribution (12 ± 3 %) from plastoquinone-9 in the A_1 site. With this contribution taken into account, the simulations yield the parameters given in Table 6-2. Although the spectra do not yield the absolute orientation of the quinone, they depend on the geometric parameter, $Tr_{Ay/x}$ determined by the ratio of the projections of the dipolar-coupling vector onto the principal y- and x-axes of the A_1^- g-tensor [39]:

$$Tr_{Ay/x} = \frac{1-3\cdot(\sin\eta_A \cdot \sin\phi_A)^2}{1-3\cdot(\sin\eta_A \cdot \cos\phi_A)^2} \tag{5.1}$$

The polar angles η_A and ϕ_A are the inclination and azimuth angles determining the direction of the electron-electron interspin vector r_{AP} in the g-tensor frame of A_1^-. As can be seen from Table 2, the value of this geometric parameter is the same, within experimental error, for phylloquinone, plastoquinone-9 and Cl_2NQ, which suggests that all three quinones are bound in their PS I binding sites in the same orientation.

Table 6-2 Magnetic and geometric parameters evaluated from the W-band time-resolved EPR spectra and W-band out-of-phase ESEEM of the spin-correlated radical pair $P_{700}^+A_1^-$.

Quinone (PS I sample)	A_1^- g-tensor (g_x, g_y)[a]	Linewidths $\Delta B_{1/2}$ /mT (x,y)[a]	$Tr_{Ay/x}$	Dipolar frequency $\nu_\perp$ / MHz	Distance r_{AP} / nm
Phylloquinone (perdeuterated WT)	2.00623, 2.00507	0.34, 0.40	-0.56 ± 0.05	2.94 ± 0.05	2.61 ± 0.02
Plastoquinone-9 (menB variant)	2.00680, 2.00519	0.86, 1.09	-0.61 ± 0.05	3.00 ± 0.05	2.59 ± 0.02

Cl_2NQ (menB variant)	2.00722, 2.00590	0.54, 0.65	-0.58 ± 0.05	2.92 ± 0.05	2.61 ± 0.02

g_z value and the corresponding linewidth could not be determined due to overlap of the A_1^- and P_{700}^+ spectral contributions.

6.3.5 Distance between P_{700}^+ andA_1^-.

The spin density distribution in P_{700}^+ (a Chl*a*/Chl*a*' dimer) is highly asymmetric and resides primarily on the eC-B1 chlorophyll. [45-47] Because of this asymmetry, the distances between radical centers in $P_{700}^+A_{1A}^-$ and $P_{700}^+A_{1B}^-$ are different. The dipolar coupling between P_{700}^+ and A_1^- depends on this distance and, therefore, can be used to deduce the contributions of the two possible radical pairs to the EPR signals. The electron-electron spin-spin coupling in the spin-polarized transient radical pair $P_{700}^+A_1^-$is measured most conveniently using the out-of-phase ESEEM technique. [48, 49] In PS I particles from the wild type [50, 51] and *menB* variant [34] such measurements yield distances consistent with the A-branch charge-separated radical pair. Figure 6-7 shows a comparison of W-band out-of-phase ESEEM data from the perdeuterated wild-type, *menB* variant and *menB* incubated with Cl_2NQ taken at the P_{700}^+ spectral region. In this region the modulation frequency observed in the out-of-phase detected echo decay corresponds to the perpendicular dipolar coupling frequency, $\nu_\perp$. This is because the dipolar vectors directed from P_{700}^+ to the semiquinones A_{1A}^- and A_{1B}^- are oriented almost perpendicularly to the z-axes of both quinones [19]. As can be seen, the echo-modulation curves (Figure 6-7a) from the *menB* variant and *menB* incubated with Cl_2NQ samples are almost identical. The sine Fourier transforms of the modulation curves (Figure 6-7b) show single peaks at $\nu_\perp$. From the calibration relation in the point-dipole approximation $\nu_\perp = 52.04(r_0/r_{AP})^3$ /MHz (r_0=1 nm) [39] the distance between the radicals can be

determined from the peak positions. The exchange coupling $J \leq 0.03$ MHz can be safely ignored. [51] The distances obtained for the three samples are given in Table 6-2, and within experimental error they are all identical. Any possible contribution from the B-branch radical pair or distribution of distances would be easily recognized as differences in the lineshapes of the peaks in the Fourier transforms of the modulation curves. [22] However, within experimental error, all three samples have the same peak shapes as can be seen in Figure 6-7b.

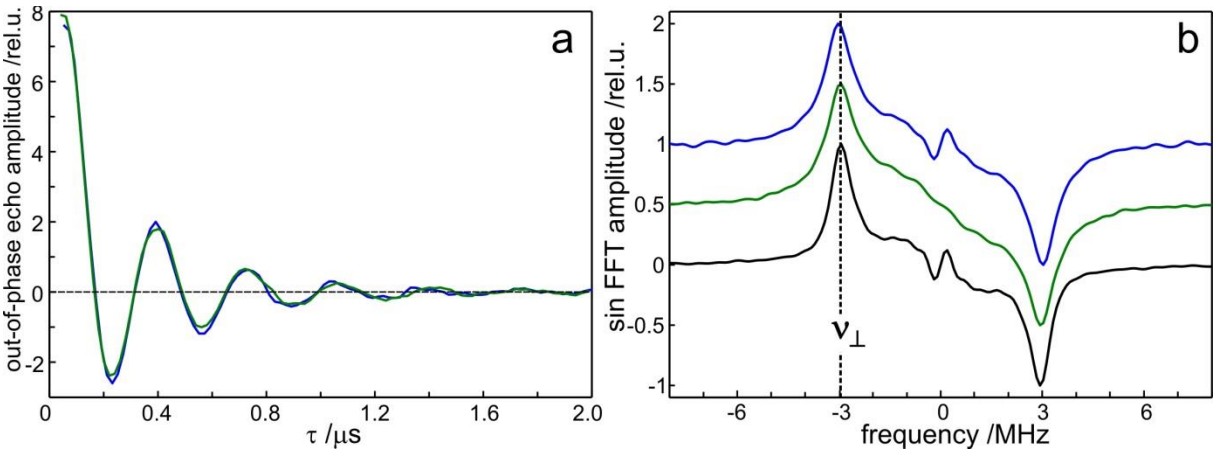

Figure 6-7 W-band out-of-phase ESEEM measurements of the *menB* variant and *menB* incubated with Cl_2NQ at 120 K. (a) Out-of-phase ESEEM traces taken at the P_{700}^+ signal maximum for the *menB* variant (blue) and Cl_2NQ sample (green). The delay-after-flash time, TDAF, was set to 400 ns and a laser repetition rate of 10 Hz was used. The signals are scaled to the maximum amplitude. (b)Sine Fourier transform amplitudes of the ESEEM decays for the *menB* variant (blue) and Cl_2NQ sample (green). For comparison, the corresponding Fourier transform for perdeuterated wild type PS I is also shown (black line).

6.3.6 Relaxation-Induced Dipolar Modulation Enhancement (RIDME) Experiments.

The orientation and distance of the radical-pair partners can be determined together by combining the spectral resolution of high-field EPR with spin-echo modulation. [39, 52] In the RIDME experiment the echo amplitude from one of the radical-pair partners is modulated by the electron spin-spin coupling due to relaxation induced-spin flips of the

partner radical. By plotting the Fourier-transform amplitudes of the modulations of the spin-echo decay trace against field position, the dipolar coupling is correlated with the g-tensor components of the radicals, thus allowing the distance between them and the relative orientation of the dipolar coupling vector and the g-tensor axes to be deduced. Figure 6-8 shows a comparison of such two-dimensional plots for the *menB* variant and the Cl_2NQ sample taken over the g_x-g_y quinone region of the spectrum. The spectral positions corresponding to quinone g_x and g_y resonance fields, B_x and B_y, are indicated by dashed lines. The solid horizontal lines indicate the frequencies associated with the parallel, $\nu_{\|}$, and perpendicular, $\nu_{\perp}$, components of the dipolar coupling, and the vertical dotted lines indicate the corresponding spectral positions at which the maximum modulation amplitude occurs. From the plot it is immediately apparent that the principal components of the dipolar coupling are identical in the two samples, and that they map onto the g-tensor axes in the same way, with the parallel component close to g_x and the visible perpendicular component close to g_y. Again this demonstrates that the position and orientation of the quinone is the same in both samples. [53] The values of the dipolar coupling are identical to those observed in the wild type so that we conclude that only the A-branch radical pair is observed.

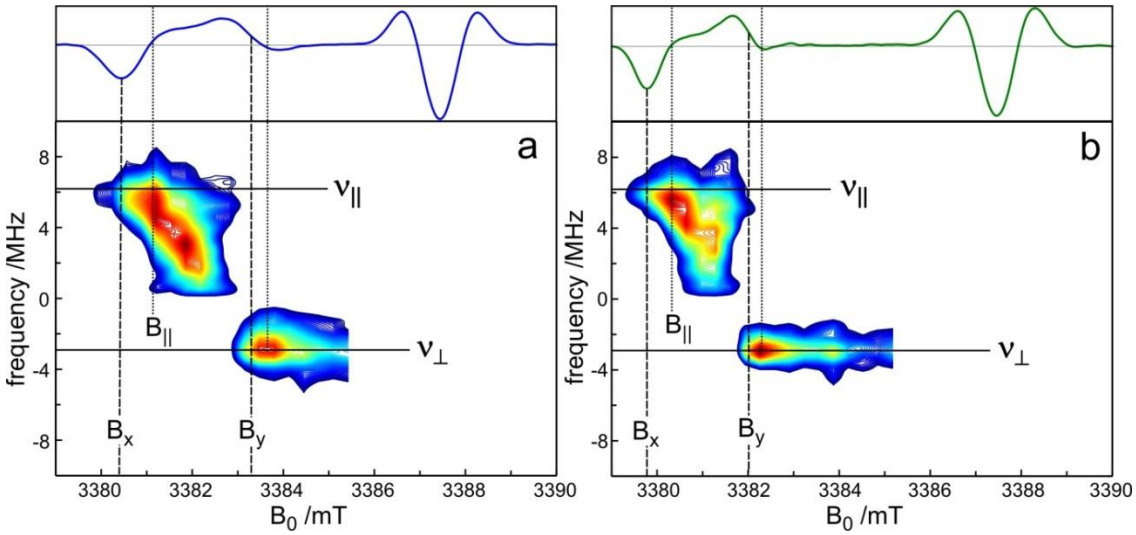

Figure 6-8 W-band dipolar out-of-phase RIDME spectra of the radical pair $P_{700}^{+}A_1^{-}$ at 120 K in *menB* variant (a) and *menB* incubated with Cl_2NQ (b). The data were collected with a long mixing period of the stimulated spin-echo pulse sequence of T = 20 µs, and the delay after the laser flash TDAF = 200 ns. The contour plot shows the positive sine Fourier amplitudes of the RIDME traces taken over the spectral region dominated by the g_x and g_y tensor components of the A_1^{-} radical. The spin-polarized TREPR spectrum of $P_{700}^{+}A_1^{-}$ is displayed above the contour plot to show the corresponding spectral positions. For additional information, see text.

6.3.7 TREPR Spectra of the *rubA*/menB Double Mutant.

All of the above data indicate that when Cl_2NQ is incorporated into PS I from the *menB* variant, electron transfer past the quinone is blocked at low temperature and that only signal contributions associated with the A-branch radical pair are observed. This suggests that the electron transfer is unidirectional in the A-branch. However, a scenario in which a fraction of the electron transfer would occur in the B-branch and proceed rapidly from A_{1B} to A_{1A} via F_x would give similar results. Such a scenario is quite unlikely for several reasons. First, it would require that only the A-branch quinone is exchanged since fast electron transfer from Cl_2NQ to F_X is energetically not feasible. Second, it is well known [54] that electron transfer beyond A_1 results in net polarization of P_{700}^{+} and that this polarization has a characteristic dependence on the magnetic field/ microwave frequency. [55] Net polarization of P_{700}^{+} is not observed in any of the TREPR data. Nonetheless, we

can test for the possibility of B-branch electron transfer using the *rubA*/*menB* double mutant. [35] This mutant is unable to synthesize phylloquinone (plastoquinone-9 is incorporated instead) and to assemble the iron-sulfur clusters. Thus, electron transfer past the quinones cannot occur. In principle, direct electron transfer between the quinones could occur, however using Dutton's ruler [56] as an estimate of the distance dependence of the electron transfer rate due to the electronic coupling, we obtain a minimum lifetime for inter-quinone electron transfer on the order of 1 µs from the edge-to-edge distance between the two quinones (~15 Å). Thus, this electron-transfer step should be slow enough to be detectable by EPR. Figure 6-9 shows a comparison of the X-band TREPR data of the *menB* and *menB/rubA* variants before and after incubation with Cl_2NQ. The spin-polarized spectra of the two variants are identical with both plastoquinone-9 (Figure 6-9a, top) and Cl_2NQ (Figure 6-9a, bottom) in the binding site. The corresponding sine Fourier transforms of the out-of-phase ESEEM curves are shown in Figure 6-9b. In all four samples the dipolar frequency is $\nu_\perp$= 2.95 MHz as indicated by the dashed line in Figure 6-9b. Thus, we conclude that in all of these samples the electron transfer is strongly biased towards the A-branch at low temperature.

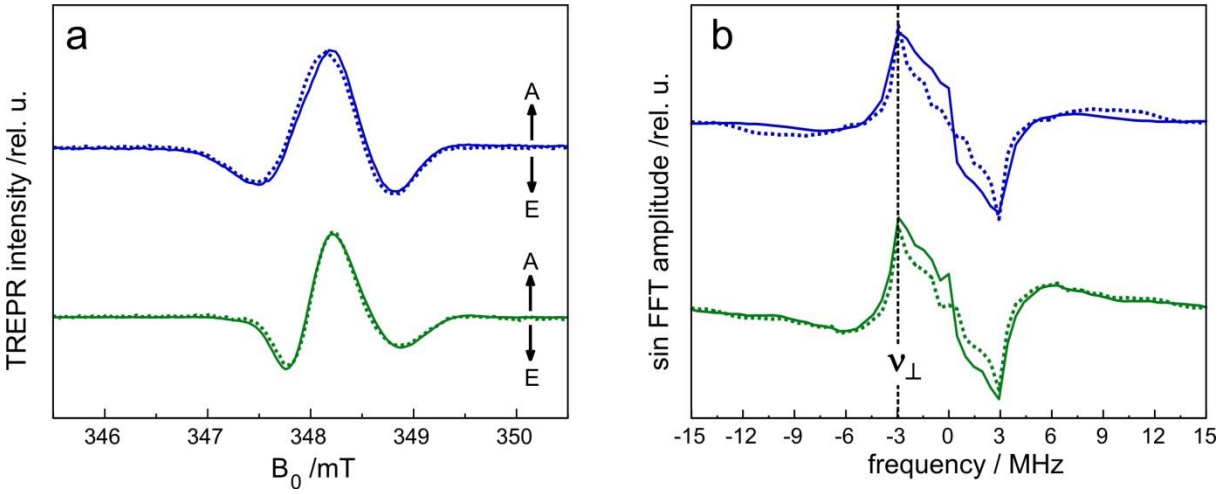

Figure 6-9 Comparison of X-band TREPR data from the *menB* variant and *menB/rubA* variant of PS I. a) Transient EPR spectra 600 ns after the laser flash. b) Sine Fourier transforms of the out-of-phase ESEEM curves. The *menB* variant data are plotted as solid lines and the data from the *menB/rubA* variant are shown as dashed lines. The blue traces are PS I containing plastoquinone-9 and the green traces are samples incubated with Cl_2NQ.

6.4 Discussion

All of the above data indicate that when Cl_2NQ is incorporated into PS I, electron transfer past the quinones does not occur. Thus, incorporation of a high-potential quinone provides an alternative to removal or reduction of F_X for blocking forward transfer. Under these conditions we find that within the detection limits of TREPR there is no evidence for involvement of the B-branch at low temperature. This is in agreement with high-field W-band EPR spectroscopy studies of the *rubA* variant [24, 57] and the point mutants PsaA-M688N and PsaB-M668N [22] which show that in dark-adapted samples without pre-reduction of the iron-sulfur clusters, electron transport in cyanobacterial PS I is strongly biased towards the A-branch of cofactors below the glass-transition temperature.

In contrast, many studies in which the iron-sulfur clusters are reduced do show evidence for low-temperature B-branch electron transfer. [4, 14, 17, 19-21, 58, 59] The origin of the different results for the two types of samples is not immediately apparent but it suggests that the directionality of electron transfer in PS I is easily influenced. Since the spin-polarized EPR spectra show that Cl_2NQ binds to the A_{1A} site in the same position and orientation as phylloquinone, it is unlikely that exchanging the quinone has any significant effect on the directionality, which is determined by the midpoint potentials and binding of the co-factors involved in the initial charge separation. On the other hand, according to electrostatic calculations, the free energy difference between midpoint potentials of A_{1A} and F_X was estimated to be +10 mV. [31] More recent semi-continuum

electrostatic approach using two dielectric constants and substantial heterogeneity of the static dielectric constant gave the value of ~ -80 mV. [30] Modeling of the forward and backward electron transfer reactions in PS I yielded the energy gap between A_{1A} and F_X of -50 – -80 mV [60]. Therefore it is possible that under experimental conditions used in some previous publications [19, 20], the pre-reduction of F_X in the presence of dithionite under illumination at low temperature is accompanied by at least partial reduction of A_{1A}. Indeed, it is known that because the midpoint potentials of A_{1A} and A_{1B} are different, addition of dithionite and illumination leads initially to accumulation of A_{1A}^- and that A_{1B} is reduced only after prolonged illumination and double reduction of A_{1A} [17]. Therefore the accumulation of charges on the acceptor side of the complex under reducing conditions changes the electrostatic environment and should affect $A_{0A}$and A_{0B} differently. We note also that the iron-sulfur clusters F_A and F_B are arranged asymmetrically with respect to the two branches and could also lead to a difference in the electrostatic effects in the two branches. The size of the overall influence of charges on the acceptor side of PS I is difficult to determine accurately, but using the calculated contributions from local charges to the midpoint potentials of the cofactors in native PS I [31, 32] as a guide, a shift of 10-100 mV in the midpoint potential of A_0 can be expected, particularly if A_{1A} becomes reduced. It has been shown that disruption of the H-bond between tyrosine PsaA-Y696 and the chlorophyll A_{0A} (or between PsaB-Y676 and chlorophyll A_{0B}) leads to redirection of electrons into the B-branch (or A-branch). [8] Thus, it is plausible that the shift in the midpoint potential due to the additional charges introduced when the acceptor side of PS I is reduced, could redirect electrons into the B-branch.

The data presented here also allow conclusions to be drawn about the origin of the different fractions observed at low temperature and the relative midpoint potentials of A_{1A} and A_{1B}. Because electron transfer from A_{1B} to F_X is known to be nearly activationless, while the A_{1A} to F_X step is strongly activated [13], it has been postulated that the irreversible fractions results from electron transfer in the B-branch. The strong bias towards the A-branch suggests that if trapping does occur via B-branch electron transfer, the single-flash quantum yield of stable $[F_A/F_B]^-$ would be very low. Moreover, the observation of back reaction from the iron-sulfur clusters at low temperature shows that electron transfer beyond the quinones does not necessarily lead to trapping and suggests that the two fractions may be the result of heterogeneity in either forward or reverse electron transfer between F_X and F_A. Incorporation of quinones with potentials higher than that of phylloquinone can also be used to make a rough estimate of the difference in midpoint point potential between A_{1A} and A_{1B}. In DMF, the difference in redox potential between phylloquinone and plastoquinone-9 and between phylloquinone and Cl_2NQ are 96 mV and 416 mV, respectively (Figure 6-2). If these differences also apply to the protein-bound quinones and we assume that reduction of $[F_A/F_B]$ is the result of a small amount of B-branch electron transfer, then the midpoint potential of A_{1B} would be at least 96 mV but less than 416 mV more negative that of A_{1A} since an $[F_A/F_B]^-$ spectrum is observed in the *menB* variant but not for the Cl_2NQ containing sample (Figure 6-5). This estimate is in line with the calculated differences of 155 mV and 173 mV calculated by Ishikita et al. [31] and Ptshenko et al. [32], repectively but does not agree with the value of 25 mV estimated by Santabarbara et al. [18]

Together, the observation of highly asymmetric electron transfer at low temperature, and the optical and EPR data indicating bidirectional electron transfer at room temperature, suggest that the relative use of the two branches in PS I is temperature dependent. This is consistent with the observation by Agalarov and Brettel [13] that the relative amplitude of the kinetic phase associated with electron transfer from A_{1B}^- to F_X becomes smaller with decreasing temperature and could not be observed reliably below 223 K. The fact that we see no evidence for B-branch electron transfer at low temperature in the Cl_2NQ sample suggests that the difficulty observing the fast phase below 223 K is due to the loss of electron-transfer activity in the B-branch. If this is the case, then changes in the shape of the spin-polarized EPR spectra of $P_{700}^+A_1^-$ can be expected at room temperature in the Cl_2NQ sample as the contribution from the B-branch radical pair $P_{700}^+A_{1B}^-$ becomes appreciable. Indeed, such differences are observed in the spectra from the *rubA* mutant. [23] However, because the iron-clusters are absent it is difficult to exclude the possibility of structural changes at high temperature. This problem should not occur in the Cl_2NQ sample, and investigations of the spin-polarized EPR spectra and kinetics at room temperature are in progress.

6.5 Acknowledgements

This work was support by grants from the Natural Sciences and Engineering Research Council, Canada to A.v.d.E., from the National Science Foundation (MCB-1021725) to J.H.G., from the Russian Foundation for Basic Research (RFBR, 09-04-01657), and from the Russian Ministry for Education and Science (16.512.12.2010) to A.Yu.S., from DFG-RFBR Cooperation Project 11-04-91330_NNIO) to A.Yu.S and K.M, from the Max-

Planck Society to A.S. and K.M. We thank Mike Gorka for providing membrane fragments of the *rubA/menB* variant.

6.6 References

1. Muller, M.G., C. Slavov, R. Luthra, K.E. Redding, and A.R. Holzwarth, *Independent initiation of primary electron transfer in the two branches of the photosystem I reaction center.* Proc. Natl. Acad. Sci. U. S. A., 2010. **107**(9): p. 4123-4128.
2. Shelaev, I.V., F.E. Gostev, M.D. Mamedov, O.M. Sarkisov, V.A. Nadtochenko, V.A. Shuvalov, and A.Y. Semenov, *Femtosecond primary charge separation in Synechocystis sp PCC 6803 photosystem I.* Biochim. Biophys. Acta-Bioenerg., 2010. **1797**(8): p. 1410-1420.
3. Boudreaux, B., F. MacMillan, C. Teutloff, R. Agalarov, F. Gu, S. Grimaldi, R. Bittl, K. Brettel, and K. Redding, *Mutations in Both Sides of the Photosystem I Reaction Center Identify the Phylloquinone Observed by Electron Paramagnetic Resonance Spectroscopy*. Journal of Biological Chemistry, 2001. **276**(40): p. 37299-37306.
4. Fairclough, W.V., A. Forsyth, M.C.W. Evans, S.E.J. Rigby, S. Purton, and P. Heathcote, *Bidirectional electron transfer in photosystem I: electron transfer on the PsaA side is not essential for phototrophic growth in Chlamydomonas.* Biochim. Biophys. Acta-Bioenerg., 2003. **1606**(1-3): p. 43-55.
5. Guergova-Kuras, M., B. Boudreaux, A. Joliot, P. Joliot, and K. Redding, *Evidence for two active branches for electron transfer in photosystem I.* Proceedings of the National Academy of Sciences, 2001. **98**(8): p. 4437-4442.
6. Xu, W., P. Chitnis, A. Valieva, A. van der Est, Y.N. Pushkar, M. Krzystyniak, C. Teutloff, S.G. Zech, R. Bittl, D. Stehlik, B. Zybailov, G. Shen, and J.H. Golbeck, *Electron Transfer in Cyanobacterial Photosystem I: I. PHYSIOLOGICAL AND SPECTROSCOPIC CHARACTERIZATION OF SITE-DIRECTED MUTANTS IN A PUTATIVE ELECTRON TRANSFER PATHWAY FROM A_0 THROUGH A_1 TO F_X.* Journal of Biological Chemistry, 2003. **278**(30): p. 27864-27875.
7. Xu, W., P.R. Chitnis, A. Valieva, A. van der Est, K. Brettel, M. Guergova-Kuras, Y.N. Pushkar, S.G. Zech, D. Stehlik, G. Shen, B. Zybailov, and J.H. Golbeck, *Electron Transfer in Cyanobacterial Photosystem I: II. DETERMINATION OF FORWARD ELECTRON TRANSFER RATES OF SITE-DIRECTED MUTANTS IN A PUTATIVE ELECTRON TRANSFER PATHWAY FROM A_0 THROUGH A_1 TO F_X.* Journal of Biological Chemistry, 2003. **278**(30): p. 27876-27887.
8. Li, Y., A. van der Est, M.G. Lucas, V.M. Ramesh, F. Gu, A. Petrenko, S. Lin, A.N. Webber, F. Rappaport, and K. Redding, *Directing electron transfer within Photosystem I by breaking H-bonds in the cofactor branches.* Proc. Natl. Acad. Sci. U. S. A., 2006. **103**(7): p. 2144-2149.
9. Santabarbara, S., A. Jasaitis, M. Byrdin, F.F. Gu, F. Rappaport, and K. Redding, *Additive Effect of Mutations Affecting the Rate of Phylloquinone Reoxidation and Directionality of Electron Transfer within Photosystem I.* Photochemistry and Photobiology, 2008. **84**(6): p. 1381-1387.

10. Jordan, P., P. Fromme, H.T. Witt, O. Klukas, W. Saenger, and N. Kraub, *Three-dimensional structure of cyanobacterial photosystem I at 2.5 A resolution.* Nature, 2001. **411**(6840): p. 909-917.
11. Brettel, K., *Electron transfer and arrangement of the redox cofactors in photosystem I.* Biochimica et Biophysica Acta (BBA) - Bioenergetics, 1997. **1318**(3): p. 322-373.
12. Schlodder, E., K. Falkenberg, M. Gergeleit, and K. Brettel, *Temperature Dependence of Forward and Reverse Electron Transfer from A_1^-, the Reduced Secondary Electron Acceptor in Photosystem I†*. Biochemistry, 1998. **37**(26): p. 9466-9476.
13. Agalarov, R. and K. Brettel, *Temperature dependence of biphasic forward electron transfer from the phylloquinone(s) A_1 in photosystem I: only the slower phase is activated.* Biochim. Biophys. Acta-Bioenerg., 2003. **1604**(1): p. 7-12.
14. Srinivasan, N. and J.H. Golbeck, *Protein–cofactor interactions in bioenergetic complexes: The role of the A_{1A} and A_{1B} phylloquinones in Photosystem I.* Biochimica et Biophysica Acta (BBA) - Bioenergetics, 2009. **1787**(9): p. 1057-1088.
15. Cohen, R.O., G. Shen, J.H. Golbeck, W. Xu, P.R. Chitnis, A.I. Valieva, A. van der Est, Y. Pushkar, and D. Stehlik, *Evidence for Asymmetric Electron Transfer in Cyanobacterial Photosystem I: Analysis of a Methionine-to-Leucine Mutation of the Ligand to the Primary Electron Acceptor A_0†*. Biochemistry, 2004. **43**(16): p. 4741-4754.
16. Karyagina, I., Y. Pushkar, D. Stehlik, A. van der Est, H. Ishikita, E.W. Knapp, B. Jagannathan, R. Agalarov, and J.H. Golbeck, *Contributions of the protein environment to the midpoint Potentials of the A_1 phylloquinones and the F_X iron-sulfur cluster in photosystem I.* Biochemistry, 2007. **46**(38): p. 10804-10816.
17. Heathcote, P., P.K. Fyfe, and M.R. Jones, *Reaction centres: the structure and evolution of biological solar power.* Trends Biochem Sci, 2002. **27**(2): p. 79-87.
18. Santabarbara, S., P. Heathcote, and M.C.W. Evans, *Modelling of the electron transfer reactions in Photosystem I by electron tunnelling theory: The phylloquinones bound to the PsaA and the PsaB reaction centre subunits of PS I are almost isoenergetic to the iron–sulfur cluster F_X.* Biochimica et Biophysica Acta (BBA) - Bioenergetics, 2005. **1708**(3): p. 283-310.
19. Poluektov, O.G., S.V. Paschenko, L.M. Utschig, K.V. Lakshmi, and M.C. Thurnauer, *Bidirectional electron transfer in photosystem I: Direct evidence from high-frequency time-resolved EPR spectroscopy.* J. Am. Chem. Soc., 2005. **127**(34): p. 11910-11911.
20. Santabarbara, S., I. Kuprov, P.J. Hore, A. Casal, P. Heathcote, and M.C.W. Evans, *Analysis of the Spin-Polarized Electron Spin Echo of the $[P_{700}^+A_1^-]$ Radical Pair of Photosystem I Indicates That Both Reaction Center Subunits Are Competent in Electron Transfer in Cyanobacteria, Green Algae, and Higher Plants†.* Biochemistry, 2006. **45**(23): p. 7389-7403.
21. Santabarbara, S., I. Kuprov, O. Poluektov, A. Casal, C.A. Russell, S. Purton, and M.C.W. Evans, *Directionality of Electron-Transfer Reactions in Photosystem I of Prokaryotes: Universality of the Bidirectional Electron-Transfer Model.* J. Phys. Chem. B, 2010. **114**(46): p. 15158-15171.

22. Savitsky, A., O. Gopta, M. Mamedov, J. Golbeck, A. Tikhonov, K. Möbius, and A. Semenov, *Alteration of the Axial Met Ligand to Electron Acceptor A_0 in Photosystem I: Effect on the Generation of $P_{700}^{\cdot+}A_1^{\cdot-}$ Radical Pairs as Studied by W-band Transient EPR.* Appl. Magn. Reson., 2010. **37**(1-4): p. 85-102.
23. Shen, G.Z., M.L. Antonkine, A. van der Est, I.R. Vassiliev, K. Brettel, R. Bittl, S.G. Zech, J.D. Zhao, D. Stehlik, D.A. Bryant, and J.H. Golbeck, *Assembly of photosystem III. Rubredoxin is required for the in vivo assembly of F_X in Synechococcus sp PCC 7002 as shown by optical and EPR spectroscopy.* Journal of Biological Chemistry, 2002. **277**(23): p. 20355-20366.
24. Shen, G.Z., J.D. Zhao, S.K. Reimer, M.L. Antonkine, Q. Cai, S.M. Weiland, J.H. Golbeck, and D.A. Bryant, *Assembly of photosystem II. Inactivation of the rubA gene encoding a membrane-associated rubredoxin in the cyanobacterium Synechococcus sp PCC 7002 causes a loss of photosystem I activity.* Journal of Biological Chemistry, 2002. **277**(23): p. 20343-20354.
25. Agalarov, R., M. Byrdin, F. Rappaport, G.Z. Shen, D.A. Bryant, A. van der Est, and J.H. Golbeck, *Removal of the PsaF Polypeptide Biases Electron Transfer in Favor of the PsaB Branch of Cofactors in Triton X-100 Photosystem I Complexes from Synechococcus sp PCC 7002.* Photochemistry and Photobiology, 2008. **84**(6): p. 1371-1380.
26. Johnson, T.W., B. Zybailov, A.D. Jones, R. Bittl, S. Zech, D. Stehlik, J.H. Golbeck, and P.R. Chitnis, *Recruitment of a foreign quinone into the A_1 site of photosystem I. In vivo replacement of plastoquinone-9 by media-supplemented naphthoquinones in phylloquinone biosynthetic pathway mutants of Synechocystis sp. PCC 6803.* The Journal of biological chemistry, 2001. **276**(43): p. 39512-21.
27. van der Est, A., Y. Pushkar, I. Karyagina, B. Fonovic, T. Dudding, J. Niklas, W. Lubitz, and J. Golbeck, *Incorporation of 2,3-Disubstituted-1,4-Naphthoquinones into the A_1 Binding Site of Photosystem I Studied by EPR and ENDOR Spectroscopy.* Appl. Magn. Reson., 2010. **37**(1-4): p. 65-83.
28. Pushkar, Y.N., S.G. Zech, D. Stehlik, S. Brown, A. van der Est, and H. Zimmermann, *Orientation and protein-cofactor interactions of monosubstituted n-alkyl naphthoquinones in the A_1 binding site of photosystem I.* J. Phys. Chem. B, 2002. **106**(46): p. 12052-12058.
29. Pushkar, Y.N., J.H. Golbeck, D. Stehlik, and H. Zimmermann, *Asymmetric hydrogen-bonding of the quinone cofactor in photosystem I probed by C-13-labeled naphthoquinones.* J. Phys. Chem. B, 2004. **108**(27): p. 9439-9448.
30. Pushkar, Y.N., I. Karyagina, D. Stehlik, S. Brown, and A. van der Est, *Recruitment of a Foreign Quinone into the A_1 Site of Photosystem I: CONSECUTIVE FORWARD ELECTRON TRANSFER FROM A_0 TO A_1 TO F_X WITH ANTHRAQUINONE IN THE A_1 SITE AS STUDIED BY TRANSIENT EPR.* Journal of Biological Chemistry, 2005. **280**(13): p. 12382-12390.
31. Ishikita, H. and E.W. Knapp, *Redox potential of quinones in both electron transfer branches of photosystem I.* Journal of Biological Chemistry, 2003. **278**(52): p. 52002-52011.
32. Ptushenko, V.V., D.A. Cherepanov, L.I. Krishtalik, and A.Y. Semenov, *Semi-continuum electrostatic calculations of redox potentials in photosystem I.* Photosynth Res, 2008. **97**(1): p. 55-74.

33. Prince, R.C., P. Lloyd-Williams, J. Malcolm Bruce, and P. Leslie Dutton, *[8] Voltammetric measurements of quinones*, in *Methods in Enzymology*, B.F. Sidney Fleischer, Editor 1986, Academic Press. p. 109-119.
34. Johnson, T.W., G. Shen, B. Zybailov, D. Kolling, R. Reategui, S. Beauparlant, I.R. Vassiliev, D.A. Bryant, A.D. Jones, J.H. Golbeck, and P.R. Chitnis, *Recruitment of a foreign quinone into the A_1 site of photosystem I. I. Genetic and physiological characterization of phylloquinone biosynthetic pathway mutants in Synechocystis sp. pcc 6803.* The Journal of biological chemistry, 2000. **275**(12): p. 8523-30.
35. Sakuragi, Y., B. Zybailov, G.Z. Shen, D.A. Bryant, J.H. Golbeck, B.A. Diner, I. Karygina, Y. Pushkar, and D. Stehlik, *Recruitment of a foreign quinone into the A_1 site of photosystem I - Characterization of a menB rubA double deletion mutant in Synechococcus sp PCC 7002 devoid of F_X, F_A, and F_B and containing plastquinone or exchanged 9,10-anthraquinone.* Journal of Biological Chemistry, 2005. **280**(13): p. 12371-12381.
36. Srinivasan, N., S. Santabarbara, F. Rappaport, D. Carbonera, K. Redding, A. van der Est, and J.H. Golbeck, *Alteration of the H-Bond to the A_{1A} Phylloquinone in Photosystem I: Influence on the Kinetics and Energetics of Electron Transfer.* J. Phys. Chem. B, 2011. **115**(8): p. 1751-1759.
37. Bagryanskaya, E.G., D. Bardelang, S. Chenesseau, J.P. Finet, L. Jicsinszky, H. Karoui, S.R.A. Marque, K. Mobius, D. Polovyanenko, A. Savitsky, and P. Tordo, *EPR, NMR, and Thermodynamic Evidences for Forced Nuclear Spin-Electron Spin Interactions in the Case of 1-Phenyl-2-Methylpropyl-1,1-Dimethyl-2-Nitroxide (TIPNO) Attached to Permethylated beta-Cyclodextrin.* Appl. Magn. Reson., 2009. **36**(2-4): p. 181-194.
38. Mobius, K., A. Schnegg, M. Plato, M.R. Fuchs, and A. Savitsky, *High-field EPR spectroscopy on transfer proteins in biological action.* Acta Phys Pol A, 2005. **108**(2): p. 215-234.
39. Savitsky, A., B.V. Trubitsin, K. Mobius, A.Y. Semenov, and A.N. Tikhonov, *Photosynthetic electron transport in the cyanobacterium Synechocystis sp PCC 6803: High-field W-band and X-band EPR study of electron flow through photosystem I.* Appl. Magn. Reson., 2007. **31**(1-2): p. 221-236.
40. Semenov, A.Y., I.R. Vassiliev, A. van der Est, M.D. Mamedov, B. Zybailov, G. Shen, D. Stehlik, B.A. Diner, P.R. Chitnis, and J.H. Golbeck, *Recruitment of a Foreign Quinone into the A1 Site of Photosystem I: ALTERED KINETICS OF ELECTRON TRANSFER IN PHYLLOQUINONE BIOSYNTHETIC PATHWAY MUTANTS STUDIED BY TIME-RESOLVED OPTICAL, EPR, AND ELECTROMETRIC TECHNIQUES.* Journal of Biological Chemistry, 2000. **275**(31): p. 23429-23438.
41. Gopta, O.A., Y.L. Kalaidzidis, A.Y. Semenov, and J.H. Golbeck, *Analysis of charge recombination kinetics in cyanobacterial photosystem I with site-specific substitutions in the vicinity of the phylloquinone molecules.* Biochim. Biophys. Acta-Bioenerg., 2006: p. 273-273.
42. Sarkisov, O.M., F.E. Gostev, I.V. Shelaev, V.I. Novoderezhkin, O.A. Gopta, M.D. Mamedov, A.Y. Semenov, and V.A. Nadtochenko, *Long-lived coherent*

oscillations of the femtosecond transients in cyanobacterial photosystem I. Physical Chemistry Chemical Physics, 2006. **8**(48): p. 5671-5678.

43. Atherton, N.M., *Bruker Lecture - the Nuclear Zeeman Interaction in Electron Resonance.* Chem Soc Rev, 1993. **22**(5): p. 293-298.
44. Kandrashkin, Y. and A. van der Est, *A new approach to determining the geometry of weakly coupled radical pairs from their electron spin polarization patterns.* Spectrochim Acta A, 2001. **57**(8): p. 1697-1709.
45. Käss, H., P. Fromme, H.T. Witt, and W. Lubitz, *Orientation and Electronic Structure of the Primary Donor Radical Cation in Photosystem I: A Single Crystals EPR and ENDOR Study.* The Journal of Physical Chemistry B, 2001. **105**(6): p. 1225-1239.
46. Plato, M., N. Krauss, P. Fromme, and W. Lubitz, *Molecular orbital study of the primary electron donor P700 of photosystem I based on a recent X-ray single crystal structure analysis.* Chem Phys, 2003. **294**(3): p. 483-499.
47. Holzwarth, A.R., M.G. Muller, J. Niklas, and W. Lubitz, *Ultrafast transient absorption studies on Photosystem I reaction centers from Chlamydomonas reinhardtii. 2: Mutations near the P_{700} reaction center chlorophylls provide new insight into the nature of the primary electron donor.* Biophysical Journal, 2006. **90**(2): p. 552-565.
48. Dzuba, S.A., P. Gast, and A.J. Hoff, *Eseem Study of Spin-Spin Interactions in Spin-Polarized $P^+Q_a^-$ Pairs in the Photosynthetic Purple Bacterium Rhodobacter-Sphaeroides R26.* Chem. Phys. Lett., 1995. **236**(6): p. 595-602.
49. Bittl, R., S.G. Zech, P. Fromme, H.T. Witt, and W. Lubitz, *Pulsed EPR structure analysis of photosystem I single crystals: Localization of the phylloquinone acceptor.* Biochemistry, 1997. **36**(40): p. 12001-12004.
50. Bittl, R. and S.G. Zech, *Pulsed EPR Study of Spin-Coupled Radical Pairs in Photosynthetic Reaction Centers: Measurement of the Distance Between and in Photosystem I and between and in Bacterial Reaction Centers.* The Journal of Physical Chemistry B, 1997. **101**(8): p. 1429-1436.
51. Zech, S.G., W. Lubitz, and R. Bittl, *Pulsed EPR experiments on radical pairs in photosynthesis: Comparison of the donor-acceptor distances in photosystem I and bacterial reaction centers.* Ber Bunsen Phys Chem, 1996. **100**(12): p. 2041-2044.
52. Mobius, K., W. Lubitz, and A. Savitsky, *Photo-Induced Electron Spin Polarization in Chemical and Biological Reactions: Probing Structure and Dynamics of Transient Intermediates by Multifrequency EPR Spectroscopy.* Appl. Magn. Reson., 2011. **41**(2-4): p. 113-143.
53. Rusanov, A.L. and A.P. Savitsky, *Fluorescence resonance energy transfer between fluorescent proteins as powerful toolkits for in vivo studies.* Laser Phys Lett, 2011. **8**(2): p. 91-102.
54. Kandrashkin, Y.E. and A. van der Est, *Time-resolved EPR spectroscopy of photosynthetic reaction centers: From theory to experiment.* Appl. Magn. Reson., 2007. **31**(1-2): p. 105-122.
55. Kandrashkin, Y.E., W. Vollmann, D. Stehlik, K. Salikhov, and A. Van der Est, *The magnetic field dependence of the electron spin polarization in consecutive spin correlated radical pairs in type I photosynthetic reaction centres.* Mol Phys, 2002. **100**(9): p. 1431-1443.

56. Moser, C.C., J.M. Keske, K. Warncke, R.S. Farid, and P.L. Dutton, *Nature of Biological Electron Transfer.* Nature, 1992. **355**(6363): p. 796-802.
57. van der Est, A. and D. Bruce, *Photosynthesis: Fundamental Aspects to Global Perspectives : Proceedings of the 13th International Congress on Photosynthesis*2005: Alliance Communications Group.
58. Santabarbara, S., I. Kuprov, W.V. Fairclough, S. Purton, P.J. Hore, P. Heathcote, and M.C.W. Evans, *Bidirectional Electron Transfer in Photosystem I: Determination of Two Distances between P_{700}^{+} and A_1^{-} in Spin-Correlated Radical Pairs†.* Biochemistry, 2005. **44**(6): p. 2119-2128.
59. Byrdin, M., S. Santabarbara, F.F. Gu, W.V. Fairclough, P. Heathcote, K. Redding, and F. Rappaport, *Assignment of a kinetic component to electron transfer between iron-sulfur clusters F_X and $F_{A/B}$ of Photosystem I.* Biochim. Biophys. Acta-Bioenerg., 2006. **1757**(11): p. 1529-1538.
60. Kumazaki, S., M. Iwaki, I. Ikegami, H. Kandori, K. Yoshihara, and S. Itoh, *Rates of Primary Electron-Transfer Reactions in the Photosystem-I Reaction-Center Reconstituted with Different Quinones as the Secondary Acceptor.* J. Phys. Chem., 1994. **98**(43): p. 11220-11225.

The following unpublished chapter contains the work of Sam Mula, whom was under the supervision of Dr. Art van der Est; both of Brock University.

Chapter 7 Heterogeneous ET in PS I at low temperature: Dependence on the midpoint potential of A_1

7.1 Introduction

The activity of the PsaA and PsaB-branches of electron transfer (ET) cofactors in Photosystem I can be measured by transient optical and electron paramagnetic resonance (EPR) spectroscopies. Room temperature studies of the $P_{700}^{+}A_1^{-}$ to $P_{700}^{+}F_X^{-}$ ET step, indicate a ratio of 70:30 for the use of the A- and B branches, respectively in complexes from Synechocystis sp PCC 6803. [1-3] The PsaA-branch A_{1A}^{-} to F_X^{-} ET step has a significant activation energy and is strongly temperature dependent, while the PsaB-branch A_{lB}^{-} to F_X^{-} ET step is temperature independent. [4] Below the protein glass transition temperature (~180 K) several types of ET can be identified by EPR spectroscopy. One type is the reversible ET between the primary donor P_{700} and the acceptor A_1 which has a lifetime of several microseconds. According to Chapter 5 [5] and early studies of point mutations [6] this reversible ET is strongly biased to the PsaA-branch. In addition, irreversible ET to the terminal [4Fe4S] clusters F_A and F_B occurs and leads to photo-accumulation of $P_{700}^{+}[F_A/F_B]^{-}$ which can be observed by continuous wave

(CW) EPR spectroscopy. At low temperature the A_{1A}^- to F_X step is essentially blocked, because it is highly activated. Thus, the irreversible ET to F_A and F_B is postulated to occur via the A_{1B}^- to F_X^- pathway. After prolonged illumination, the $P_{700}^+[F_A/F_B]^-$ signal accounts for about half the PSI reaction centers. This accumulated fraction is trapped indefinitely and will not recombine. Finally, a small amount of reversible ET to the iron-sulfur clusters occurs with a lifetime of several milliseconds, which can be observed by transient EPR using field modulation detection. [7] The reversible fractions intensity do not diminish even after hours of illumination. The origin of this heterogeneous behavior is not known. However, the difference in kinetics and activation energies of the A_1^- to F_X^- ET step in the two branches suggests that the difference in thermodynamic properties of the two quinones, A_{1A} and A_{1B}, may play a role. Currently, it is not known how important this difference is in determining the appearance of these different fractions at low temperature.

The accumulation of P_{700}^+ and $[F_A/F_B]^-$ can be measured as a function of quinone redox potential by comparing the behavior of wild-type and the *menB* variant of *Synechocystis* sp. PCC 6803. The reduction midpoint potentials of the two quinones, phylloquinone and plastoquinone, which occupy the A_1 site in these two species are -465 mV and -369 mV vs the standard hydrogen electrode (SHE), respectively when measured in aprotic solvents (i.e. dimethyl formamide). It is reasonable to assume the difference of 100 mV between the two midpoint potentials of the mutual naphthoquinones is preserved when in the binding site, therefore in the *menB* variant the quinones in the A_{1A} and A_{1B} binding sites are expected to be 100 mV more positive than in the wild-type. If the very low midpoint potential of the PsaB-branch phylloquinone and the resulting temperature

independent electron transfer is an important factor in allowing irreversible charge separation to occur, then the accumulation behavior in the WT and *menB* mutant should differ strongly.

7.2 Materials and Methods

7.2.1 Growth and Isolation of PSI Trimer Reaction Centers from the *menB* Mutant and wild-type *Synechocystis* sp. PCC 6803.

The *menB* mutant strain of *Synechocystis* sp PCC 6803 [8, 9] was grown under low light (See Appendix III for complete description) and the corresponding wild type strain was grown under normal light. [10] Trimeric PS I complexes were isolated from both strains as described in Appendix I. The isolated trimers were brought to a chlorophyll *a* concentration of 2 mg/mL by centrifuging to a thick paste using 100K Ultracell purification membranes followed by resuspension in a 50 mM Tris-buffer at pH 8.0 containing 0.05% n-dodecyl-β-D-maltoside and 1% glycerol as a cryo-protectant.

7.2.2 X-band CW EPR measurements of P_{700}^{+} Accumulation

X-Band spectra of the P_{700}^{+} were collected with a Bruker E580 pulsed and CW X-band spectrometer equipped with Super X-FT Microwave Bridge and Flexline dielectric resonator. The signal was detected by using 100 kHz field modulation and digitized by the E580 signal channel. Samples containing 1.7 µM PSI (0.17 mg/mL Chl-*a*),1 mM sodium ascorbate and 50µM DCPIP were prepared with the buffer described above to a volume of 100 µL. Each sample was dark adapted for 15 minutes before being frozen to the desired temperature in the resonator of the EPR spectrometer in the dark. A reference spectrum was taken in the dark to ensure that complete reduction of the P_{700}^{+} by DCPIP

had occurred prior to illumination. Laser flashes at 4.0mJ/pulse were then applied to the sample. This energy is high enough to provide one photon per chlorophyll per flash or 100 photons per PSI complex.

7.2.3 X-band CW EPR measurements of $[F_A/F_B]^-$ Accumulation

X-Band EPR spectra of $[F_A/F_B]^-$ were collected as described in section (7.2.2) but were only taken at 15 K because the spin relaxation of the $[F_A/F_B]^-$ is too fast to allow the CW EPR signal to be detected at higher temperatures.

7.3 Results and Discussion

7.3.1 X-Band CW-EPR of PSI samples under continuous illumination.

7.3.1.1 The photo-accumulated P_{700}^+

The 80 K CW EPR of the photo-accumulated P_{700}^+ signals for the *menB* and wild-type samples can be seen in Figure 7-1. The P_{700}^+ EPR signals have been integrated using Bruker XEPR software to allow easier comparison of their intensities. Under continuous illumination, (Figure 7-1 black curve) the spectrum represents the P_{700}^+ equilibrium population of both reversible and irreversible ET. As can be seen its intensity is equal for the *menB* variant and wild-type samples. The accumulated irreversible signal P_{700}^+ (Figure 7-1 red curve), which persists after several cycles of continuous illumination and "dark relaxation", represents a fraction of reaction centers in which irreversible ET has occurred and the transferred electron is trapped, presumably on the terminal acceptors F_A and F_B. Again, the intensity of the spectrum is virtually the same for *menB* and wild-type samples. The "dark relaxation" refers to a five minute period during which the sample is not illuminated.

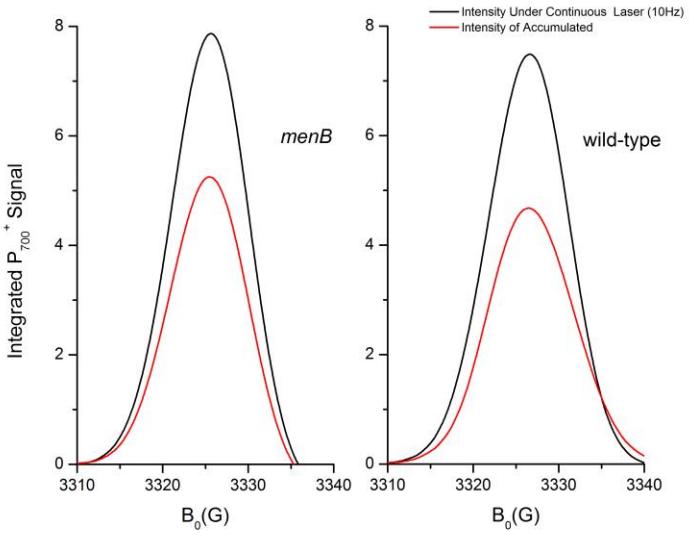

Figure 7-1: Low Temperature (80 K) X-Band CW EPR spectra at 80K of the light induced species P_{700}^{+} for *menB* (left) and wild-type (right) under continuous illumination (black line) and 5 minutes after illumination (red line).

7.3.1.2 The Photo-accumulated $[F_A/F_B]^-$

The X-Band CW EPR spectra taken of the photo-accumulated $[F_A/F_B]^-$ signal at 15 K can be seen in Figure 7-2. The intensity of the *menB* signal is weaker than the wild type. The experiment was repeated several times. Each iteration of the accumulation involved a fresh sample preparation from stock purified PSI. The difference in intensity persisted for each iteration. For comparison, the accumulated P_{700}^{+} signal for *menB* and wild-type at 15 K can be seen in Figure 7-3. The menB P_{700}^{+} signal intensity is weaker than the wild-type. Collectively these signals represents a fraction of ET that results in the static state P_{700}^{+} $[F_A/F_B]^-$ at low temperature (15 K). The difference in intensity from 80 K to 15 K for the P_{700}^{+} signal is hypothesized to result from a temperature dependent step, which includes the step between the A_{1A} and F_X cofactors as shown by Schlodder et. al. [4] At very low temperatures (15 K) the Gibbs free energy and reorganization energy may account for the change in signal intensity.

The trapping of these populations requires many saturating laser pulses (5,000 + flashes). Therefore, the single turnover accumulation of P_{700}^{+} and $[F_A/F_B]^{-}$ signals for the *menB* and wild-type samples were examined.

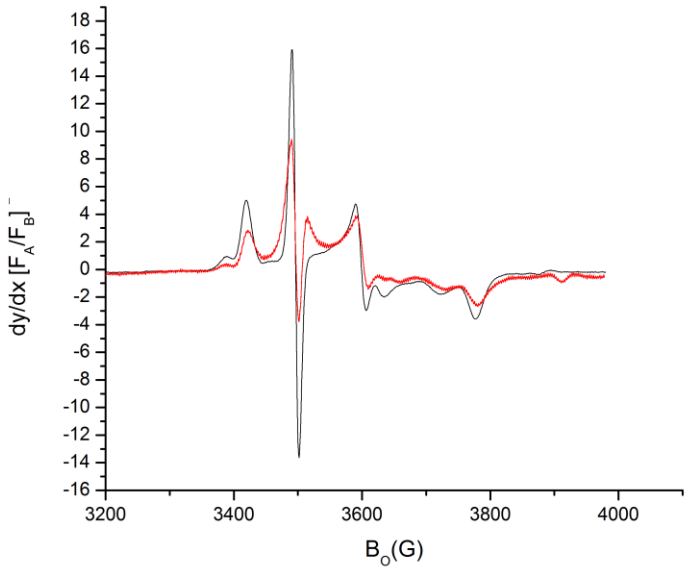

Figure 7-2: X-Band CW EPR spectra of accumulated light induced $[F_A/F_B]^{-}$ for *menB* (red) and wild-type (black) taken at 15 K.

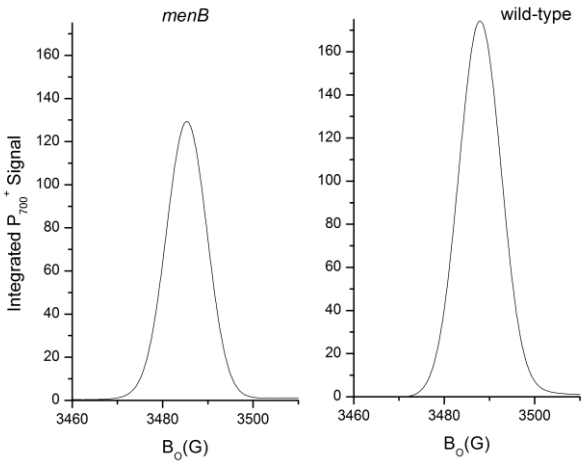

Figure 7-3: X-Band CW EPR spectra of accumulated P_{700}^{+} for *menB* (left) and wild-type (right) during continuous illumination by laser flashes at 10 Hz and 4.0mJ/pulse taken at 15 K.

7.3.2 X-Band CW-EPR of PSI samples with single flash illumination

7.3.2.1 The accumulation of P_{700}^{+} by single flash illumination.

The single flash accumulation of P_{700}^{+} signal for *menB* and wild-type samples can be seen in Figure 7-4. The *menB* sample accumulates P_{700}^{+} faster in ~500 flashes than the wild-type. The integrated P_{700}^{+} spectra Figure 7-4 (a) and (b) peak heights were plotted verse laser flash count as shown in Figure 7-4 (c) and (d).

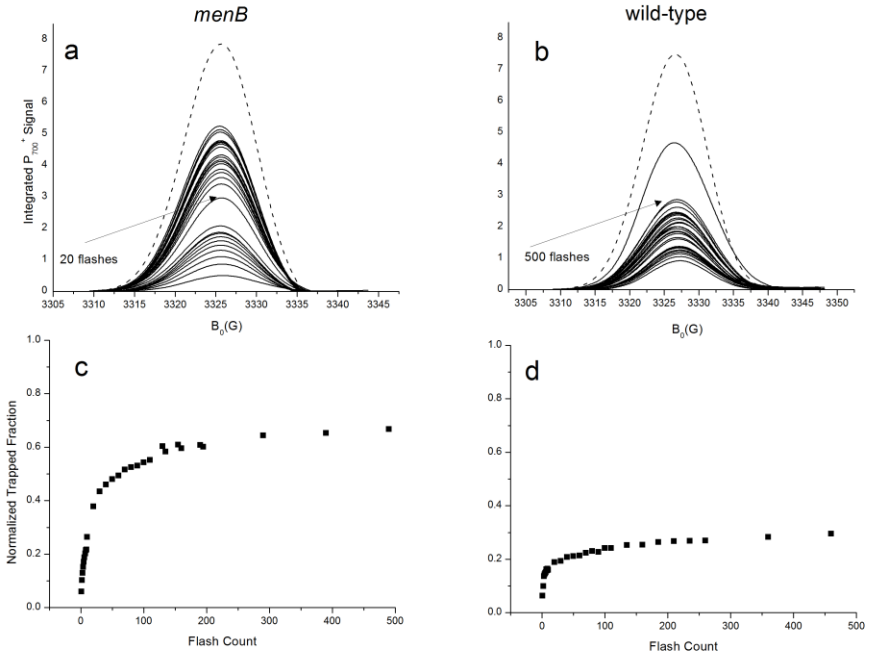

Figure 7-4: Low Temperature (80 K) X-Band CW EPR spectra of the P_{700}^{+} single flash accumulation for menB (a) and wild-type (b). The continuous illumination intensity (Dotted Line) is the signal equilibrium of reversible and irreversible species whose lifetimes are longer than the flash rate (10 Hz). The accumulated signal (solid line) represents the long lived fraction. The trapped fraction has been normalized to the continuous illumination signal and plotted as a function of laser flash count for menB (c) and wild-type (d).

In the *menB* sample, the irreversible P_{700}^{+} signal accumulates faster during the first 100 flashes than it does in the wild-type. The figure shows that for wild-type 500 flashes were required to reach an intensity of ~3 while for the menB only 20 flashes were needed to

reach the same intensity. Quantum calculations of the A_1 cofactor in the binding site propose a difference of 173 mV between the A_{1A} and A_{1B} reduction midpoint potentials. [11] In addition, the reduction midpoint potential of plastoquinone-9 and phylloquinone measured in dimethyl formamide (DMF) vs the standard hydrogen electrode (SHE) differs by 100 mV. If the difference in solution midpoint potentials between plastoquinone-9 and phylloquinone were maintained when incorporated into the binding pocket, then the *menB*, being 100 mV more positive, should produce wild-type A_{1A} behavior for the *menB* A_{1B} and promote slower accumulation, but it does not. In fact, the rapid accumulation of the *menB* P_{700}^{+} signal would suggest the change in redox potential of the *menB* A_{1B} quinone has increased the rate of the A_{1B}^{-} to F_X ET step when compared to the native wild-type, which is unlikely.

At room temperature the reversible P_{700}^{+} components have lifetimes of 3.5 ms and 90 ms for samples *menB* and wild-type, respectively. Longer lifetimes are present at low temperature which correspond to those reaction centers with reversible ET to the iron sulfur clusters; a result which has been confirmed by PsaC protein subunit deletion mutants [12]. In the absence of the PsaC-subunit, electron transfer from the [4Fe4S] clusters F_A and F_B do not contribute. Therefore decay kinetics of P_{700}^{+} can be examined for the absence of lifetimes which are associated with F_A and F_B with and without the PsaC deletion mutant. This result confirms the long lived species are for those electrons returning from the [4Fe4S] clusters F_A and F_B.

7.3.2.2 The $[F_A/F_B]^-$ accumulation by single flash illumination.

The result for the accumulation of $[F_A/F_B]^-$ signal after single laser flashes measured by X-Band CW EPR for *menB* and wild-type are shown in Figure 7-5. The

menB sample accumulates $[F_A/F_B]^-$ signal faster when compared to wild-type, which agrees with the result for the P_{700}^+ accumulation.

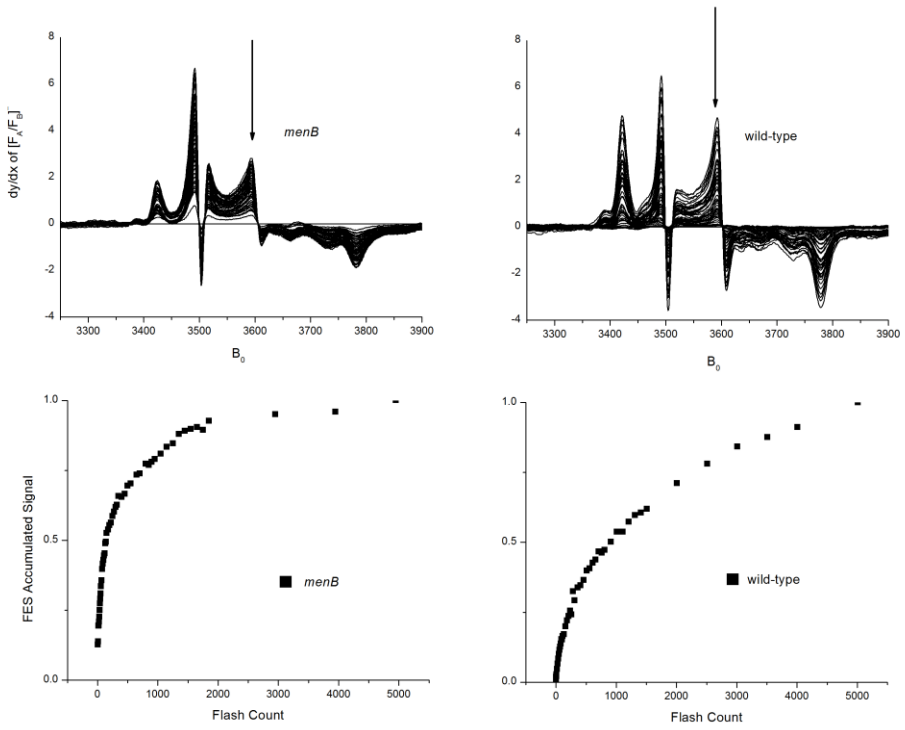

Figure 7-5: X-Band CW EPR spectra at 15 K of the $[F_A/F_B]^-$ single flash accumulation for *menB* (a) and wild-type (b).

We postulate that the approach to the saturation point for the *menB* and wild type differ due to the differences in back reaction lifetimes. Upon each single laser flash induced ET turnover, the number of available reaction centers capable of performing light induced charge separation is less in the wild-type due to the longer back reaction lifetime compared to *menB*. If both samples, *menB* and wild-type, show a final accumulation of similar intensity with such a significant difference in redox potential then the heterogeneity of the accumulation must be due to an equilibrium step that is common to both *menB* and wild-type and not one that involves the A_1 cofactor.

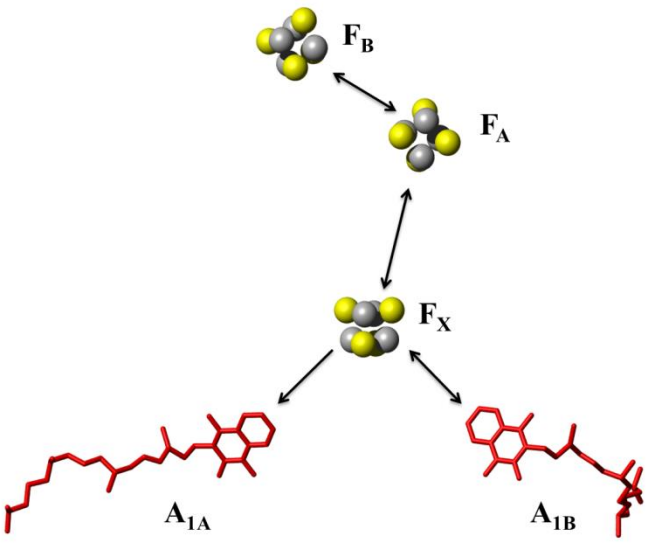

Figure 7-6: Selected cofactors of the PSI reaction core provided from the PDB file 1JB0. ET steps involving the cofactors A_{1A}, A_{1B}, F_X, F_A and F_B. The arrows indicate the forward and reverse steps possible between the cofactors at low temperature (80 K).

7.3.3 Alternatives to Quinone Dependence

Alternative steps that may be responsible for heterogeneity involve the cofactors F_X, F_A and F_B. (Figure 7-6) The forward step to F_X from either the A_{1A} or A_{1B} cofactor does not have an effect on the final amount of trapping as seen in Figure 7-1. The A_{1A} to F_X step is blocked at low temperature but the reverse reaction is still possible. If the forward reaction does not influence the total amount as seen in Figure 7-1, then it would follow that the back reaction from F_X to the A_{1A} or A_{1B} should not limit the amount of trapping.

The ET between F_A and F_B is known to have a small activation barrier. This is evident by the change in relative intensity of the F_A^- or F_B^- signal measured by CW-EPR over the small thermal range of 15-18 K (data not shown). Thus, this step does not appear to influence the amount of trapping or reversible ET.

The step between F_X and F_A is predicted to have an effect on the back reaction heterogeneity. There are two possible ways that you could get a distribution of rates for the ET between F_A and F_X. There could be a distribution of activation energies or there could be a distribution of electronic couplings. It is not possible to say which of these two is more important. However, it is plausible that different protonation states and conformations of the protein side chains could lead to different activation barriers.

7.4 References

1. Setif, P. and K. Brettel, *Forward electron transfer from phylloquinone A_1 to iron-sulfur centers in spinach photosystem I.* Biochem, 1993. **32**(31): p. 7846-7854.
2. Boudreaux, B., F. MacMillan, C. Teutloff, R. Agalarov, F. Gu, S. Grimaldi, R. Bittl, K. Brettel, and K. Redding, *Mutations in Both Sides of the Photosystem I Reaction Center Identify the Phylloquinone Observed by Electron Paramagnetic Resonance Spectroscopy.* J Bio Chem, 2001. **276**(40): p. 37299-37306.
3. Guergova-Kuras, M., B. Boudreaux, A. Joliot, P. Joliot, and K. Redding, *Evidence for two active branches for electron transfer in photosystem I.* P Nat Ac Sci, 2001. **98**(8): p. 4437-4442.
4. Schlodder, E., K. Falkenberg, M. Gergeleit, and K. Brettel, *Temperature Dependence of Forward and Reverse Electron Transfer from A_1^-, the Reduced Secondary Electron Acceptor in Photosystem $I^\dagger$.* Biochem, 1998. **37**(26): p. 9466-9476.
5. Mula, S., A. Savitsky, K. Mobius, W. Lubitz, J.H. Golbeck, M.D. Mamedov, A.Y. Semenov, and A. van der Est, *Incorporation of a high potential quinone reveals that electron transfer in Photosystem I becomes highly asymmetric at low temperature.* Photoch Photobio Sci, 2012. **11**(6): p. 946-956.
6. van der Est, A., C. Bock, J. Golbeck, K. Brettel, P. Setif, and D. Stehlik, *Electron-Transfer from the Acceptor A_1 to the Iron-Sulfur Centers in Photosystem I as Studied by Transient Epr Spectroscopy.* Biochem, 1994. **33**(39): p. 11789-11797.
7. Savitsky, A., B.V. Trubitsin, K. Mobius, A.Y. Semenov, and A.N. Tikhonov, *Photosynthetic electron transport in the cyanobacterium Synechocystis sp PCC 6803: High-field W-band and X-band EPR study of electron flow through photosystem I.* Appl. Magn. Reson., 2007. **31**(1-2): p. 221-236.
8. Johnson, T.W., G. Shen, B. Zybailov, D. Kolling, R. Reategui, S. Beauparlant, I.R. Vassiliev, D.A. Bryant, A.D. Jones, J.H. Golbeck, and P.R. Chitnis, *Recruitment of a foreign quinone into the A_1 site of photosystem I. I. Genetic and physiological characterization of phylloquinone biosynthetic pathway mutants in Synechocystis sp. pcc 6803.* J Biol Chem, 2000. **275**(12): p. 8523-30.
9. Johnson, T.W., B. Zybailov, A.D. Jones, R. Bittl, S. Zech, D. Stehlik, J.H. Golbeck, and P.R. Chitnis, *Recruitment of a foreign quinone into the A_1 site of photosystem I. In vivo replacement of plastoquinone-9 by media-supplemented*

naphthoquinones in phylloquinone biosynthetic pathway mutants of Synechocystis sp. PCC 6803. J Biol Chem, 2001. **276**(43): p. 39512-21.

10. Anderson, S.L. and L. Mcintosh, *Light-Activated Heterotrophic Growth of the Cyanobacterium Synechocystis Sp Strain Pcc-6803 - a Blue-Light-Requiring Process.* J Bacteriol, 1991. **173**(9): p. 2761-2767.
11. Ptushenko, V.V., D.A. Cherepanov, L.I. Krishtalik, and A.Y. Semenov, *Semi-continuum electrostatic calculations of redox potentials in photosystem I.* Photosynth Res, 2008. **97**(1): p. 55-74.
12. Shinkarev, V.P., B. Zybailov, I.R. Vassiliev, and J.H. Golbeck, *Modeling of the P_{700}^{+} Charge Recombination Kinetics with Phylloquinone and Plastoquinone-9 in the A_1 Site of Photosystem I*, in *Biophys J*2002. p. 2885-2897.

Chapter 8 General Discussions and Future Work

The three research projects presented in this thesis were done through collaborations with many faculties in many research facilities across several different countries in an effort to examine the influence of the protein environment on the A_1 cofactor and the effective thermodynamic factors governing the A_1 to F_X ET step in PSI. This was done in order to elucidate its contribution to the overall transfer of an electron from the donor P_{700} to the terminal acceptors F_A and F_B.

The influence of the protein medium on the A_1 cofactor is still not well understood. However, the work discussed in Chapter 5 reveals the backbone nitrogen of the PsaA-L722 residue in *Chlamydomonas reinhartii* PSI which binds the A_1 cofactor to the protein matrix with a single hydrogen bond could be changed and an additional hydrogen bond does occur through the side chain of the threonine residue. The most interesting result is the non-Arrhenius behavior of the A_1 to F_X rate in both the PsaA-L722T and PsaA-L722W [1] PSI mutants. The rate becomes virtually temperature independent for the two samples below 200 K. The non-linear behavior requires a different mathematical fitting model and as such the Hopfield model [2] was employed. The Hopfield model suggests small changes in activation energy (~10 meV) and a single frequency mode of the vibrational energy in the range of 400 cm^{-1} to account for the change in slope for the two mutants. The Hopfield fitting results are reasonable and fit the data well. However, the physical requirement the fit suggests is not scientifically sound. The thermal energy *kT* at 200 K is sufficient to overcome the potential energy requirement imposed by a 400 cm^{-1} vibrational mode for the zero-point energy. This being the case the rate is not

affected by a quantum mechanical cause. A temperature independent rate suggest the barrier is activationless and that $\Delta G^{*} = 0$. The physical requirement that is imposed by Marcus Theory is that λ must be equal to the driving force $-\Delta G^{o}$. Values for the driving force were obtained from the literature with midpoint potentials of A_{1A}, A_{1B} and F_X being -671, -804 and -654 mV [3], respectively. The calculated influence of a hydrogen bond is estimated to be ~100 mV. To achieve activationless ET the value of λ would need to increase substantially to more than 1.0 eV. The requirement of a large λ so close to the protein glass transition does not seem feasible as it would imply a broad potential well. Broad potential wells are suggested to occur from secondary interactions of the protein which should be frozen out at the protein glass transition. It is difficult to define the atomic motion responsible for a changing λ. Changes of the reorganization energy for the glass phase transition are currently being explored [4] and the work shows an inability of Marcus Theory to define such non-Arrhenius behavior in terms of ergodicity.

The room temperature ET reaction rates for the A_{1A} to F_X step and the A_{1B} to F_X step are certainly different with signal decay lifetimes of 200 and 20 ns for the respective reactions. [5, 6] In addition to the difference in rates at room temperature, the PsaA-branch has a temperature dependent reaction rate which leads to reversible ET at temperatures below ~280 K. [7] The two active branches of ET are unique to PSI. Other photoactive reaction centers (PSII and Purple Bacterial Reaction Centers) only exhibit unidirectional ET. In Chapter 6 it was shown the driving force ΔG^{o} for the A_1 to F_X ET step could be altered by incorporation of a high midpoint potential quinone 2,3-dichloro-1,4-naphthoquinone (Cl_2NQ) into the A_1 binding site of *menB* PSI which amounted to a blocked electron transfer passed the A_1 cofactor. After blocking the A_1 to F_X reaction it

was concluded the only identifiable ET was that of the reversible ET PsaA-branch. Reaction centers which incorporated the Cl_2NQ showed no accumulation of the iron sulfur cluster signal therefore no irreversible electron transfer could be identified. High frequency pulsed W-band EPR experiments, which resolves the spins of the $P_{700}^{+}A_1^{-}$ radical pair, showed no evidence of B-branch electron transfer at low temperature and it was concluded that at low temperature the ET becomes strongly biased to A-branch transfer. This is different than what was seen in work done by Poluektov et. al. [8], where chemical reduction of the iron-sulfur cluster F_X and A_{1A} with dithionite in the presence of light for photosynthetic algae PSI showed clear evidence of a B-branch radical pair at low temperature. The difference in low temperature observations could be the result of different experimental conditions or the use of different photosynthetic organisms.

The work discussed in Chapter 7 was done to explore the low temperature ET of PSI. Irreversible electron transfer results in accumulated $P_{700}^{+}[F_A/F_B]^{-}$ signal after each successive laser flash. Interestingly, the population of reaction centers that undergo this irreversible electron transfer only occurs in roughly half of the sample. The other half undergo reversible electron transfer to both A_{1A} and F_A/F_B as demonstrated time resolved absorbance and CW and transient EPR spectroscopy. It is postulated the A_1 cofactor is the determining step in the heterogeneity. Upon exploration of the low temperature accumlated signals from ET as a function of the A_1 cofactor in the *menB* and wild type PSI a similar behavior was seen. The difference in solution midpoint potential of the platiquinone-9 and phylloquinone is believed to remain once incorporated into the A_1 binding site and therefore places the menB A_{1B} 100 mV higher than the wild-type A_{1B}. This increase should produce wild-type A_{1A} behavior in the menB A_{1B} binding site and

have a significant effect on the irreversible accumulated state $P_{700}^{+}[F_A/F_B]^{-}$. The data show a marginal difference between the accumulated P_{700}^{+} signal at 80 K. This implies that the A_1 to F_X step does not determine the final amount of trapping or irreversible electron transfer to F_A and F_B. It also implies that the F_X to A_1 step does not determine the final amount of trapping. Therefore, we suggest the F_A to F_X step can be influenced by an activation barrier or a change in electronic coupling as a result of freezing the protein. The F_A and F_B cofactors are bound by the PsaC-subunit separating them from the PsaA and PsaB subunits and could be susceptible to factors not identifiable by A_{1A} and A_{1B} transfer.

8.1 References

1. Srinivasan, N., S. Santabarbara, F. Rappaport, D. Carbonera, K. Redding, A. van der Est, and J.H. Golbeck, *Alteration of the H-Bond to the A_{1A} Phylloquinone in Photosystem I: Influence on the Kinetics and Energetics of Electron Transfer.* J. Phys. Chem. B, 2011. **115**(8): p. 1751-1759.
2. Hopfield, J.J., *Electron-Transfer Between Biological Molecules by Thermally Activated Tunneling.* Proc. Natl. Acad. Sci. U. S. A., 1974. **71**(9): p. 3640-3644.
3. Srinivasan, N. and J.H. Golbeck, *Protein–cofactor interactions in bioenergetic complexes: The role of the A_{1A} and A_{1B} phylloquinones in Photosystem I.* BBA-Bio, 2009. **1787**(9): p. 1057-1088.
4. LeBard, D.N. and D.V. Matyushov, *Dynamical transition, hydrophobic interface, and the temperature dependence of electrostatic fluctuations in proteins.* Phys Rev E, 2008. **78**(6).
5. Guergova-Kuras, M., B. Boudreaux, A. Joliot, P. Joliot, and K. Redding, *Evidence for two active branches for electron transfer in photosystem I.* P Nat Ac Sci, 2001. **98**(8): p. 4437-4442.
6. Xu, W., P.R. Chitnis, A. Valieva, A. van der Est, K. Brettel, M. Guergova-Kuras, Y.N. Pushkar, S.G. Zech, D. Stehlik, G. Shen, B. Zybailov, and J.H. Golbeck, *Electron Transfer in Cyanobacterial Photosystem I: II. DETERMINATION OF FORWARD ELECTRON TRANSFER RATES OF SITE-DIRECTED MUTANTS IN A PUTATIVE ELECTRON TRANSFER PATHWAY FROM A_0 THROUGH A_1 TO F_X.* J Bio Chem, 2003. **278**(30): p. 27876-27887.
7. Schlodder, E., K. Falkenberg, M. Gergeleit, and K. Brettel, *Temperature Dependence of Forward and Reverse Electron Transfer from A_1^-, the Reduced Secondary Electron Acceptor in Photosystem $I^{\dagger}$.* Biochem, 1998. **37**(26): p. 9466-9476.

8. Poluektov, O.G., S.V. Paschenko, L.M. Utschig, K.V. Lakshmi, and M.C. Thurnauer, *Bidirectional electron transfer in photosystem I: Direct evidence from high-frequency time-resolved EPR spectroscopy*. J. Am. Chem. Soc., 2005. **127**(34): p. 11910-11911.

Appendix I PSI Isolation from Cyanobacteria Cells

The following procedure is based on that developed at Penn State University and adapted at Brock University.

1) Record weight of an empty centrifuge bottle. This will be used to calculate cell pellet weight in Step 6.

2) Begin chilling French Press Piston and **1 L** of 50mM Tris pH 8.0 for later steps (Steps 7 & 8)

3) Spin down **2-4 Liters** (large prep) of cells culture at 8000 rpm for 5 minutes (will take multiple spins)

Figure I-1: Liquid cyanobacteria cell culture being bubbled with compressed air. Media contains no carbon source and cells are grown photoautotrophically.

4) Wash final cell pellets in 100mL 50mM Tris pH 8.0

5) Spin down washed cells at 8000 rpm for 5 minutes.

6) Weigh cell pellet. (KEEP CELLS COLD they will break more readily.)

7) Resuspend cell pellet in ice cold 50 mM Tris, pH 8.0 buffer. (Ratio: 1 gram cells/ 10 mL Tris buffer) If you have a homogenizer, use it here to insure cells are homogeneous.)

8) Break cells with 3 passes through the French Press. (Piston should be cold.) Cells should experience 20,000 psi at the exit. Solution should drip out at a rate of 2 drops/second if done properly.

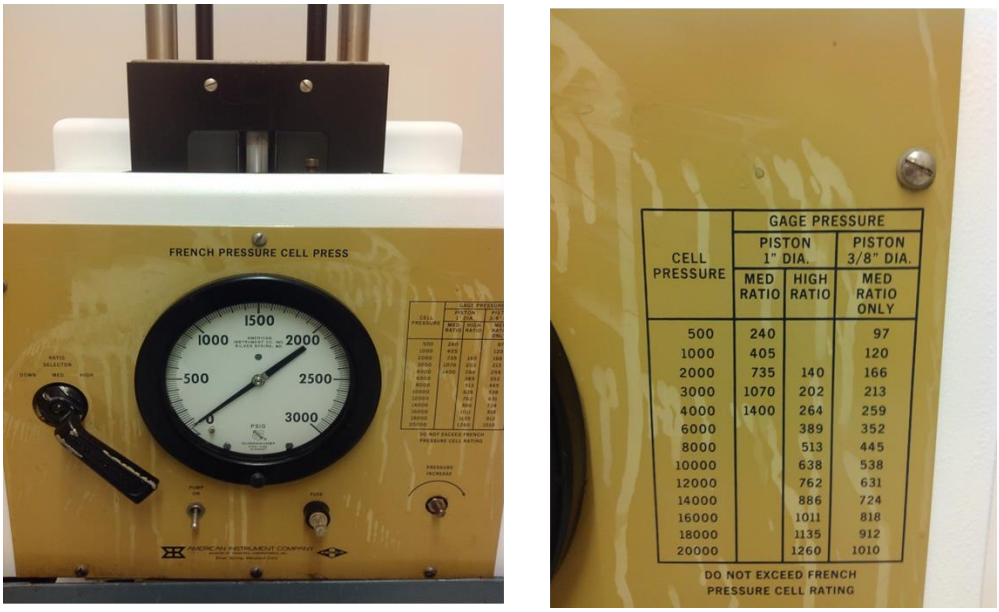

CELL PRESSURE	GAGE PRESSURE		
	PISTON 1" DIA.		PISTON 3/8" DIA.
	MED RATIO	HIGH RATIO	MED RATIO ONLY
500	240		97
1000	405		120
2000	735	140	166
3000	1070	202	213
4000	1400	264	259
6000		389	352
8000		513	445
10000		638	538
12000		762	631
14000		886	724
16000		1011	818
18000		1135	912
20000		1260	1010

DO NOT EXCEED FRENCH PRESSURE CELL RATING

Figure I-2: French Pressure Cell Press which is operated at a High Ratio of 1260 with the 1 " piston diameter. Cell experience 20,000 psi at the exit port of the piston.

9) Centrifuge broken cell slurry for 5 minutes at 8000 rpm. (the supernatant should be green with a red hue and there should be a large pellet in the bottom of the tube.)

10) Transfer **SUPERNATANT** to swinging bucket ultracentrifuge tubes (40 mL tubes) and spin down for 1 hr at 28,000. This speed is for the Beckman SW28. And corresponds to about 140,000 x g. For other rotors the speed should be adjusted to achieve this g value.

11) Dispose of bilinprotien-containing supernatant (The supernatant has a red hue due to the billin fluorescence and will appear blue when poored out). The pellet is thylakoid membrane fragments containing PSI.

12) Re-suspend the thylakoid pellet in a small volume of 50mM Tris buffer pH 8.0 to obtain a chlorophyll-*a* concentration of 1mg/mL.

13) Thylakoids can be frozen and stored for future solubilization. (-70C)

14) Solubilize thylakoids at a chlorophyll concentration of 0.5 mg/mL and 1% w/v β-dodecyl-maltoside (beta-dM) for 30 to 45 minutes and prepare your continuous sucrose gradients

15) Spin down the solubilized membrane fragments at 12,000 rpm for 5 minutes.

16) Using gradient maker and pre-prepared 20% and 5% w/v sucrose solutions containing 0.05% beta-dM pour a continuous sucrose gradient at ~4mL/minute. If no gradient maker is available do a layer by layer gradient with sucrose/beta-dM solutions (20%, 17%, 15%, 12%, 10%, 7% and 5%). Gradient volume is adjusted based on tube size. (Appendix IV)

17) Load solubilized thylakoid mix onto gradient and spin for 16 hrs to separate bands. A load:gradient ratio of 1:10 should be used. 10mL (.5mg/mL chlorophyll concentration) on the 30mL gradient works well. Three isolated bands should form (orange and two green). If the gradient is overloaded good separation of bands will not be obtained.

18) Collect bottom band for trimeric PSI

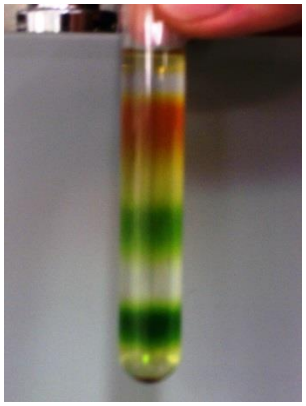

Figure I-3: Initial sucrose gradient of solubilized thylakoid membranes separated by size with carotenoids band (top), PSII band (middle) and PSI trimer band (bottom).

19) Purifying PSI: The crude your PSI trimers collected from the bottom band will still contain unwanted protein and contaminants.

20) Remove detergent from collected PSI by dialysis or extensive washing in Millipore centrifuge concentrators with.

    a) For Dialysis use 50kDa membrane with 2 volumes of 50 mM Tris Buffer pH 8 with **NO DETERGENT**. 200 fold dilution for each treatment.

    b) For washing use 8mL of crude PSI to obtain 500uL of collected sample in the Millipore centrifuge concentrators. (50 -100kDa pore size)

Figure I-4: Ultra-centrifuge tubes containing 100 K Dalton retention cellulose millipore ultra-centrifuge spin columns for retaining PSI trimer complexes.

21) Second gradient will be same as first (15) but with NO DETERGENT. Spin for 16 hrs

22) Pelleted PSI can be resuspended and concentrated **BEFORE** being brought up in final buffer 50mM Tris pH 8.0, 15% glycerol and 0.05%beta-dM. Some PSI may remain in gradient. Collect the bottom most band and add to re-suspended pellet. Wash with large aliquots (4 mL) of 50mM Tris pH 8.0 buffer.

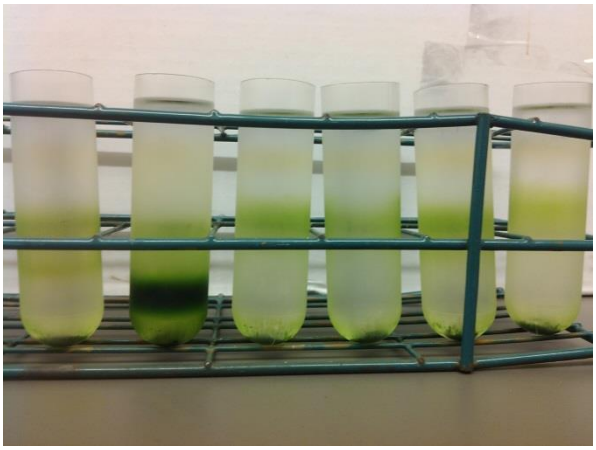

Figure I-5: Second sucrose gradient containing no detergent. PSI trimer complexes are pelleted during the 16 hour spin at 28,000 rpm.

23) Preparation of sample for concentration measurement: Pipet 10 uL of (22) PSI trimers into 990 uL of methanol in a 1 mL centrifuge tube.

24) Spin down solution in a bench top centrifuge at 10,000 rpm for 1 minute.

25) Pipet the supernatant into a 1x1cm quartz cell and measure the Chl-*a* UV-Vis absorbance signal at 667 nm .

26) Concentration of Chl-*a* sample will be $C=A_{667}*200/82$.

Appendix II BG-11 Media for Cyanobacteria Cultures

BG-11 Media Recipe (make 1 L flasks)

Per 100 mL

1) 1 mL	**100x BG-11 w/out Fe, PO_4 or CO_3**
2) 0.1 mL	**1000x Ferric Ammonium Citrate**
3) 0.1 mL	**1000x Sodium Carbonate**
4) 0.1 mL	**1000x Dipotassium Hydrogen Phosphate**
5) 0.05 mL	**50 mg/mL Spectinomycin (menB only)**

Recipes for Stock Solutions

100x BG-11 w/out Fe, PO_4 or CO_3

Per Liter

149.6 g	**$NaNO_3$**
7.49 g	**$MgSO_4 \cdot 7H_2O$**
3.60 g	**$CaCl_2 \cdot 2 H_2O$**
0.60 g	**Citric Acid**
1.12 mL	**Na EDTA, pH 8, 0.25M**
100 mL	**Trace Minerals**

Trace Minerals

Per Liter

2.86 g	**H_3BO_3**
1.81 g	**$MnCl_2 \cdot 4 H_2O$**
0.222 g	**$ZnSO_4 \cdot 7 H_2O$**
0.39 g	**$Na_2MoO_4 \cdot 2 H_2O$**
0.079 g	**$CuSO_4 \cdot 5 H_2O$**

0.0494 g **$Co(NO_3)_2$• 6 H_2O**

1000x Ferric Ammonium Citrate

Per Liter

6.00 g **$Fe(NH_4)_3(C_6H_5O_7)_2$**

1000x Sodium Carbonate

Per Liter

20 g **Na_2CO_3**

1000x Dipotassium Hydrogen Phosphate

Per Liter

30.5 g **K_2HPO_4**

0.25 M NaEDTA pH 8.0

Per Liter

78.785 g **NaEDTA**

pH with Acetic Acid EDTA will not dissolve readily until you pH the solution.

Antibiotic for *menB* Media

Per 50 mL

Stock Solution 50 mg/mL

2.5 g **Spectinomycin**

Appendix III Cell Maintenance Protocol

Cell Maintenance

No Glucose in Media

Growth Temperature
32-34 Celsius

menB
Low Light 2500 uE

Agar Medium Plates for Photosynthetic Cells
Thick Plates
Per Liter
1% Agar plates.

100 g	Agar
1000 mL	BG-11 media

*Cook Media and Allow to cool before adding (filter sterilized glucose (1% final volume) and antibiotic when necessary)

Glycerol Cell Culture Stocks
Per 1 mL

200 uL	Glycerol (should be autoclaved then filter sterilized)
800 uL	Cell Culture

Appendix IV Cell Solution Preparation Protocols

Cell Preparation Solutions

50 mM Tris Buffer pH 8.0
Per Liter
6.055 g **Tris Base**
pH to 8.0 with Acetic Acid

Beta d-Maltoside (detergent) 5% stock solution
Per 40 mL
2.00 g **beta d-Maltoside**

Sucrose Gradient Solutions
20% Sucrose Solution
Per 500 mL
100 g **Sucrose**
495 mL **50 mM Tris pH 8.0**
5 mL **5 % beta dM stock**

Tris Gradient Solution
Per 500 mL
495 mL **50 mM Tris pH 8.0**
5 mL **5 % beta dM stock**

Gradient Tubes
40 mL tubes (30 mL for density gradient 10 mL for sample load)

20 %	17%	15%	12%	10%	7%	5%
5	5	5	5	5	2.5	2.5

Stock for Density Gradient Tube
Per 50 mL

	20% Sucrose	Tris Gradient Solution
20%	50 mL	0 mL
17%	42.5 mL	7.5 mL
15%	37.5 mL	12.5 mL
12%	30 mL	20 mL
10%	25 mL	25 mL
7%	17.5 mL	32 mL
5%	12.5 mL	37.5 mL